DESIGN AND FABRICATION OF MULTILAYER STRUCTURES IN DYNAMIC SENSING AND TRANSPARENT NANOCOMPOSITE SCINTILLATORS FOR HIGH ENERGY LIGHT DETECTION

A Dissertation
Presented to
The Academic Faculty

by

Gyu Hyon Lee

In Partial Fulfillment
Of the Requirements for the Degree
Doctor of Philosophy in the
School of Materials Science and Engineering

Georgia Institute of Technology

May 2017

DESIGN AND FABRICATION OF MULTILAYER STRUCTURES IN DYNAMIC SENSING AND TRANSPARENT NANOCOMPOSITE SCINTILLATORS FOR HIGH ENERGY LIGHT DETECTION

Approved by:

Dr. Zhitao Kang, Advisor
Georgia Tech Research Institute
Georgia Institute of Technology

Dr. Christopher J. Summers, Advisor
School of Materials Science and Engineering
Georgia Institute of Technology

Dr. Brent K. Wagner
Georgia Tech Research Institute
Georgia Institute of Technology

Dr. Naresh N. Thadhani
School of Materials Science and Engineering
Georgia Institute of Technology

Dr. Meilin Liu
School of Materials Science and Engineering
Georgia Institute of Technology

Date Approved: March 23rd, 2017

To my Family.

ACKNOWLEDGEMENTS

During PhD studies, fortunately my journey was not alone and filled with many people who kindly support me and willingly help me both physically and mentally.

First, I would thank my Advisors Dr. Zhitao Kang and Dr. Christopher Summers for all their kind supports, insightful guidance, and encouragements during my Ph.D. life. I would like to pay great appreciation to Dr. Kang for pushing me and guiding me to try my best through my entire doctoral studies while being very understanding. I would like to thank both of them for showing great patients in reviewing my papers and this thesis. I thank Dr. Brent Wagner for his guidance, and technical advice in different projects, particularly in the deposition processes and tools. I would like to also thank Dr. Naresh Thadhani for the valuable advice especially in dynamic behaviors of materials and in reviewing papers. I would like to thank Dr. Meilin Liu for being my thesis committee member, and for providing me with valuable feedback to carry my dissertation to completion.

I would like to greatly thank David Scripka for co-working on the dynamic sensor work, various dynamic compression measurements and his insightful advice and discussions on designing the optical structures. I would like to also thank Christian Struebing for helping with some of the XRD measurements, gamma-ray excitation measurements and numerous discussions on the scintillators work. I would like to also thank Junghyun Noh, my great friend and colleague for numerous insightful advice, and help in both personal and academic life. They contributed significantly to the works in this thesis. I would like to also thank all other GTRI members: Dr. Jason Nadler for training and letting me use the polishers and the SEM, Hunter Chan for his countless help

in various measurements, Steven Turano for teaching me the metal deposition tools, Virginia Liao for numerous advice, discussions and being a great friend, Kavin Manickaraj for helpful discussions, Brooke Barta for XRD, and hot temperature box furnace help, Yaru Ni, Changyan Sun, Dr. Wusheng Tong, Dr. Jud Ready, Mike Harris, Ben Jacobs, and Carter Johns.

I would like to thank my friends and collaborators: Jenny Jeong for being the best friend and my companion, putting up with me even through the tough times and endlessly supporting and loving me, Timothy Huang for being a great friend, helpful academic discussions, and mental support, Sang-Eon Park for being an awesome friend and helping me through a memorable graduate life, Alex Bryant for DSC measurements, Vincent Wu, Kathy Tuan, Dr. Ikjun Choi, Dr. Yoon Sang Kim, Dr. Doh-Yeon Park, Dr. Jung Pil Lee, Dr. Jung Tae Lee, Dr. Jaehan Jung, Dr. Youngho Jin, Dr. Soo Kyung Kim, Dong Chan Lee, Yohan Park, Young Jun Yoon, Yoon Joo Na, Ah-Young Song, Dr. Chin Park, Dr. Hyoung Joon An, Sungkun Hwang, Young Kyu Jeon, Dongjune Kim and all other GTKSA basketball team members. I would like to thank them once again who have shared great adventure with me throughout my years here at Georgia Tech.

My parents have been truly supportive and encouraging during my Ph.D. studies, and even before that. I thank my parents for their endless love, sacrifices, and trust. Without their endless support, I would not have been able to achieve my degree.

TABLE OF CONTENTS

ACKNOWLEDGEMENTS iv
LIST OF TABLES viii
LIST OF FIGURES ix
SUMMARY xiii
1. Introduction 1
1.1 Motivation 1
1.2 Operating Principles 2
1.2.1 Scintillators 2
1.2.2 Photonic Crystals 3
1.2.3 Optical Microcavities 4
1.3 Background and Challenges and Research Objectives 6
1.3.1 Transparent nanocomposite scintillators 6
1.3.2 Optical structures for dynamic loading sensors 7
1.4 Research Objectives 10
1.5 Map of Dissertation 12
2. Transparent Nanocomposite Scintillators 13
2.1 Introduction 13
2.2 Experimental 16
2.3 Results and discussion 19
2.3.1 Optical Characterization 20
2.3.2 Glass Matrix Comparisons 22
2.3.3 GdF_3 and $BaGdF_5$ nanocrystal comparisons 23
2.3.3. $BaGdF_5$ nanocrystal based scintillator with GdF_3 nucleation agent 25
2.4 Conclusion 34
3. 2D Photonic Crystal for light extraction enhancement 36
3.1 Introduction 36
3.2 Simulation Approach 38
3.2.1 Array Arrangement 39
3.2.2 Air Filling Fraction (Radius to Spacing ratio) 40
3.2.3 Dielectric Constant (Refractive Index) 41

3.2.4 Optimized Design 43
3.3 Fabrication Approach 44
3.4 Results and Discussions 46
3.5 2D Photonic Crystal for dynamic loading sensors 52
3.6 Conclusions 56
4. 1D Photonic Crystal for dynamic loading sensor 58
4.1 Introduction 58
4.2 Design criteria and material selection 61
4.3 Simulation 65
4.3.1 Effect of the order of the reflectance peak and number of bilayers 65
4.3.1 Effect of the refractive indices difference 68
4.4 Device Fabrication and Dynamic Loading Experiments 70
4.5 Conclusion 76
5. Asymmetrical Optical Microcavity for dynamic loading sensor 77
5.1 Introduction 77
5.2 Design Methodology 79
5.3 AOMC Fabrication Procedure 88
5.4 Results and Discussion 89
5.5 Conclusion 94
6. Conclusions and Future Work 96
6.1 Conclusions 96
6.2 Future Works 99
REFERENCES 102
VITA 106

LIST OF TABLES

Table 2.1 X-ray radiation results on BGFT scintillators..... 21

Table 2.2 Gamma-ray excitation results on other scintillator systems with GdF_3 or $BaGdF_5$ nanocrystals in different glass matrices 22

Table 2.3 Gamma ray radiation results on GdF_3 and $BaGdF_5$ nanocrystal based scintillators. 24

Table 2.4 XRD analysis on BGFTGF:y=3 and BGFT:y=1 samples. 28

Table 2.5 Gamma ray radiation results on GdF_3 and $BaGdF_5$ based scintillators 33

Table 4.1 List of fabricated structures and their optical properties 73

Table 5.5.1. Comparison between simulated and experimental spectral characteristics .. 89

Table 5.5.2. Comparison of parameter values between simulated and measured spectra for both the original and modified SiO_2 AOMC structures 91

LIST OF FIGURES

Figure 1.1 Basic working principle of scintillator 2

Figure 1.2 Simple Schematic of 1D, 2D, and 3D photonic crystal structures 3

Figure 1.3 Schematics of various OMC structures 5

Figure 2.1 Images of successfully fabricated transparent nanocomposite scintillators under UV lamp with inset image under 6 MeV X-ray. 19

Figure 2.2 (a) PL spectra of $BaGdF_5$ nanocrystal based scintillator samples with different Tb doping concentration; y denotes to molar amount of Tb in raw composition and (b) PLE spectra of the 2% Tb doped $BaGdF_5$ based sample 20

Figure 2.3 PL and PLE spectra of undoped GdF_3 glass-ceramic sample 21

Figure 2.4 XRD spectra of both GdF3 (left) and BaGdF5 (right) nanocrystal based scintillators collected at respectively different annealing temperatures. 23

Figure 2.5 Absorption spectra of y=4 Tb doped BGFT and BGFTGF samples. 26

Figure 2.6: Decay results of y=4 Tb doped BGFT and BGFTGF samples. 27

Figure 2.7 XRD spectra of BGFTGF:y=3 (left) and BGFT:y=1 (right) samples at different annealing conditions; top marker represents $BaGdF_5$ peak positions and bottom marker represents small peaks that are suspected to be responsible by (110) and (300) of GdF_3 28

Figure 2.8 DSC thermograms of y=3 Tb doped BGFT and BGFTGF samples at 20 ℃/min heating rate. 30

Figure 2.9 TEM images of the BGFTGF:y=3 sample, top inset image shows SAED pattern and bottom inset image shows low magnification TEM image revealing uniform distribution of nanoparticles. 31

Figure 2.10 EDS scanning profile in STEM mode for various elements in the typical BGFTGF scintillator sample 31

Figure 3.1 Schematics of the transparent nanocomposite scintillator without and with a 2D PhC surface layer: (a) the emission is expected to be more vertical with the 2D PhC which helps the out-coupling into the PMTs (b) close up view of the scintillator structure with the 2D PhC layer. 37

Figure 3.2 a) Simulated frequency of the photonic band level 1 and 2 for infinite height 2D PhC slab with dielectric constant of 2.402, hexagonal array of cylindrical air holes b) simulated photonic bandgap width between photonic bands 1 and 2 with different dielectric constant for infinite height 2DPhC slab with hexagonal array of cylindrical air holes 40

Figure 3.3 Photonic bandgap area in %, for a hexagonal lattice of cylindrical holes with a r/a ratio of 0.4..... 41

Figure 3.4 Photonic band structure of a 2D PhC infinitely thick slab with a hexagonal array of holes with a relative dielectric constant of 2.4 (n = 1.55) and r/a ratio 0.365..... 43

Figure 3.5 Schematic flow diagram of the 2D PhC slab fabrication process 45

Figure 3.6 Optical Microscope Image of dosage array after (a) e-beam exposure and (b) pattern transfer to the Cr hard mask layer..... 46

Figure 3.7 SEM micrographs after the pattern was transferred from the ZEP resist to the Cr hard mask layer 47

Figure 3.8 SEM micrographs after the pattern was transferred from the Cr hard mask layer to SiO_xN_y PhC layer..... 48

Figure 3.9 (a, b) SEM micrographs after remaining Cr and ZEP layers have been removed (c) AFM micrograph of the array with an inset figure showing the depth profile 49

Figure 3.10 Reflectance spectra taken varying sample angles. Inset image shows the PC sample under white light illumination 50

Figure 3.11 SEM micrographs of 2D PhC structures: (a) a square array of square holes and (b) a square array of square pillars..... 52

Figure 3.12 Diffracted light angle measurement using coherent laser sources and the rainbow spectra collection setup using an incoherent white light source for 2D PhC structures 53

Figure 3.13 Diffraction angle of green (532 nm) and blue (460 nm) coherent radiation source by 2D square lattice PhC structures..... 54

Figure 3.14 Diffraction of incoherent white light source by 2D square lattice PhC structure displaying rainbow spectra for PhCs with different lattice constants and geometries 54

Figure 4.1 Schematic of a SiO_A/SiO_B DBR structure designed for dynamic loading experiments showing the geometrical arrangements for shock wave generation and optical characterization in reflection 63

Figure 4.2 (a) Reflectance spectra of DBRs simulated for different optical modes tuned to position the reflectance peak at 500 nm for 5 and 10 bilayers, respectively; (b) Dependence of FWHM (blue) and device thickness (red) required to achieve a reflectance peak at 500 nm for different numbers of bilayers and mode number. For each mode, the thickness of each layer in the bilayer was obtained using Eq. (4.1) assuming the same optical path length for each layer. The total thickness of the device for each mode, m, for a different number of BLs was calculated using Eq. (4.3). 65

Figure 4.3 (a) Reflectance spectra simulated for a 10 bilayer DBR tuned to position the 3rd order mode reflectance peak at 500 nm for different bilayer refractive indices; (b) Dependence of FWHM (blue) and peak reflectance (red) on the refractive index difference of the bilayers 68

Figure 4.4 Reflectance spectra of the fabricated DBR structure, the original design, and 2% thickness variations from the fabrication errors incorporated in the simulation with (a) 5 BLs and (b) 11BLs. 71

Figure 4.5 Reflectance spectra of the fabricated DBR structures with (a) a single step IAD run and (b) multiple steps IAD run. 72

Figure 4.6 Reflectance spectrum of a fabricated DBR structure taken by the streak camera for different times successfully capturing the shift in reflectance peak caused by applied shock pressure of ~4.0 GPa 74

Figure 5.1 Schematic of a SiO_2 (or Al_2O_3) AOMC structure under dynamic loading experiment and the reflectance spectrum simulated for a $Ag/SiO_2/Ag$ AOMC with a 500 nm thick SiO_2 cavity layer (continuous blue line), and after being compressed to the fracture limit (dotted red line). The inset depicts the calculated shift in the reflectance minimum due to the maximum static compression at the strain to failure point. 82

Figure 5.2 (a) Shape of reflectance spectra simulated for different modes of AOMCs tuned for reflectance minimum at 535 nm (b) dependence of FWHM and cavity thickness (as required to achieve a reflectance minimum at 535 nm) on cavity mode number 84

Figure 5.3 (a) Dependence of reflectivity of Ag mirror at 535 nm on Ag thickness (b) dependence of characteristic minimum (m=3) FWHM and depth on Ag mirror layer 1 thickness for a fixed SiO_2 cavity thickness of 500 nm and Ag mirror layer 2 thickness of 125 nm; inset image shows zoomed in graph of a region of interest 86

Figure 5.4 Reflectance spectra of the simulated design, fabricated structures and the fitted simulation based on experimental results of (a) SiO_2 and (b) Al_2O_3 AOMC structures .. 89

Figure 5.5 (a) Schematic of SiO_2 AOMC structure fabricated using Al_2O_3 adhesion layers and (b) comparison of simulated and measured reflectance spectra of modified and the original SiO_2 AOMC structure..... 91

Figure 5.6 (a) Spectral and temporal response of a modified SiO_2 AOMC device to a 4 GPa shock front. The spectra were recorded using a streak camera at different times to capture the shift in the reflectance minimum (mode 3) caused by the applied shock pressure. (b) The reflectance minimum over time and (c) change in the reflectance minimum position over time after shock propagation. 92

SUMMARY

The development and exploitation of materials science, such as chemical synthesis, physical processes such as diffusion and transport, and the understanding of the thermodynamics that drives these processes are the foundation of new materials and material structures. For example, novel approaches in growth and processing techniques combined with an understanding of quantum effects have led to the development of quantum dots and nanoparticles with unique electronic and optoelectronic properties. Subsequently, new applications have emerged in the field of quantum dot electronics, energy storage systems, and optical communication devices.

In the present study, we have extended the principles of chemical synthesis to the solid phase regime to achieve the formation of nanoparticles of scintillating materials ($BaGdF_5$ and GdF_3) in different solid glass matrices to form novel transparent nanocomposite scintillators. Judicious manipulation of materials choice and thermal processing to drive diffusion and control solubility in the liquid-solid space has resulted in the selection of the robust host glass matrix and the high energy radiation absorbing material (aluminosilicate glass as the host for $BaGdF_5$:Tb nanoparticles). These nanocomposite and similar material systems offer a new approach to achieve large area, low-cost and efficient scintillators. As a result, we have achieved 2.4 times improvement in light output under gamma-ray excitation. To further enhance efficiency, we have investigated technologies for patterning 2D photonic crystal structures into the surface of the scintillators to improve light out-coupling into a photomultiplier tube (PMT). The potential of this embodiment has been demonstrated and resulted in a completely different and new opportunity for dynamic load sensing.

During the investigation of 2D photonic crystal structures for dynamic loading sensing, it has become apparent that linearly deposited multilayer (1D photonic crystal) structures offer the best solution; therefore, optical microcavity (OMC) and distributed Bragg reflector (DBR) multilayer structures have been examined in greater detail. From a deeper understanding of the interplay between the optical and acoustic properties, highly sensitive devices ($Ag/Al_2O_3/SiO_2/Al_2O_3/Ag$ asymmetrical OMC (AOMC) and SiO_{x1}/SiO_{x2} DBR structures) have been successfully developed and extensively characterized. At a relatively low applied shock pressure of ~4 GPa, both structures have exhibited spectral peak shifts of ~14-24 nm with response time <3 ns, limited only by the acoustic properties of the optically active material. These devices demonstrate the unique attributes of high sensitivity to shock pressure, ultra- fast response and with the additional potential for 2D imaging which can further widen the understanding of materials behavior under extreme conditions.

1. Introduction

1.1 Motivation

The development and exploitation of materials science, such as chemical synthesis, physical processes such as diffusion and transport, and the understanding of the thermodynamics that drives these processes are the foundation of new materials and material structures. The tremendous advancement in state-of-the-art fabrication, synthesis and characterization techniques combined with more comprehensive understanding of materials, have led to development of innovative products providing unprecedented convenience in life. With increasing intellectual thoughts, ideas, and drives for new concepts, there are increasing needs for components with more specific requirements. Subsequently, many optical structures are being utilized as they can provide more information due to intrinsic nature of fast response (as it utilizes light). For example, there are increasing needs in sensors that can provide accurate information in a very short time such as in self-driving vehicles. Optical sensors can fulfill these requirements but can also be used to understand the unknown materials properties in extreme conditions. Another example would be in a medical field. Optical medical imaging tools capable of providing high resolution images in less invasive ways can provide doctors an immense amount of precise information that can help treating patients. Therefore, in this thesis, we will investigate various optical structures to provide advanced capabilities for sensor applications and medical imaging (detector) applications.

1.2 Operating Principles

1.2.1 Scintillators

A scintillator is a material that absorbs energy when struck by an incoming high energy particle (such as light) and re-emits the absorbed energy in the form of light at a lower energy after a delay ranging anywhere from nanoseconds to hours [1]. Basic principal operation of the scintillator when coupled to a photomultiplier tube (PMT) is shown in Figure 1.1.

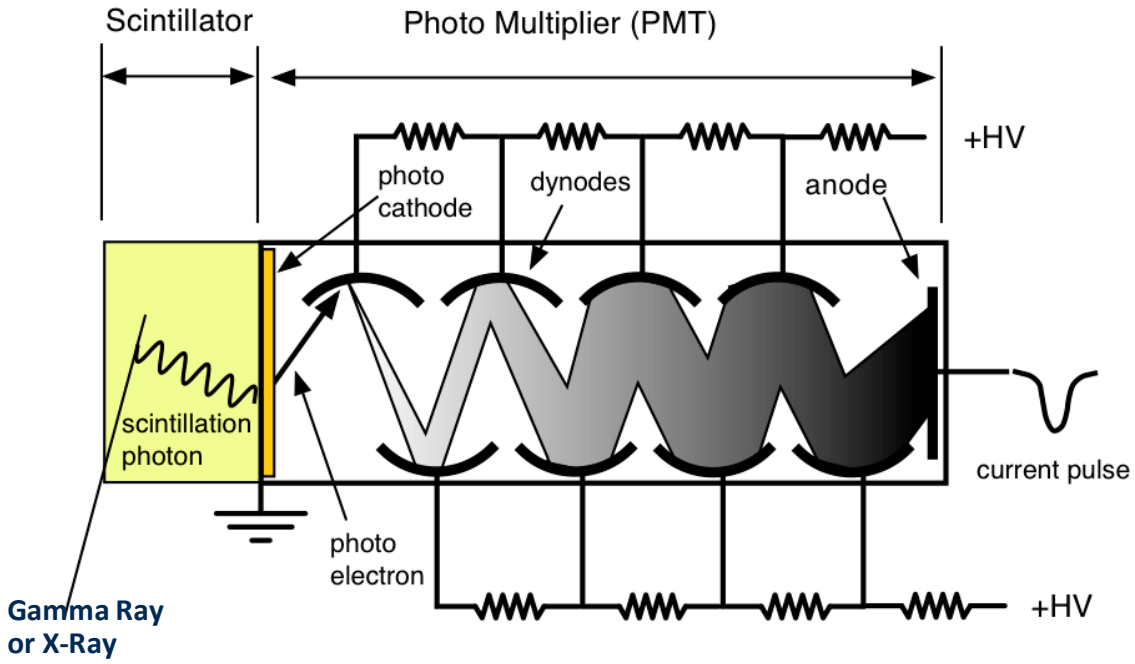

Figure 1.1 Basic working principle of scintillator

Usually, scintillators are used as a high energy light detector (such as x-ray) as it can absorb high energy light and re-emits in the visible light region that can be coupled to a PMT. The PMT converts this light into an electric signal which can be analyzed and provide meaningful information. This setup is used to amplify the signal up to ~1000 times both by the scintillator and the PMT. Currently, there are several types of

scintillators used in the market. Main applications of scintillators are in medical imaging, radiation therapy tools and radiation detectors.

1.2.2 Photonic Crystals

Photonic crystals (PhCs) are composed of periodic materials with high and low refractive index regions that affect the propagation of light. PhCs can have this periodic variation in one, two or all three orthogonal directions. An example of 1D, 2D, and 3D PhC structures are shown in Figure 1.2 [2].

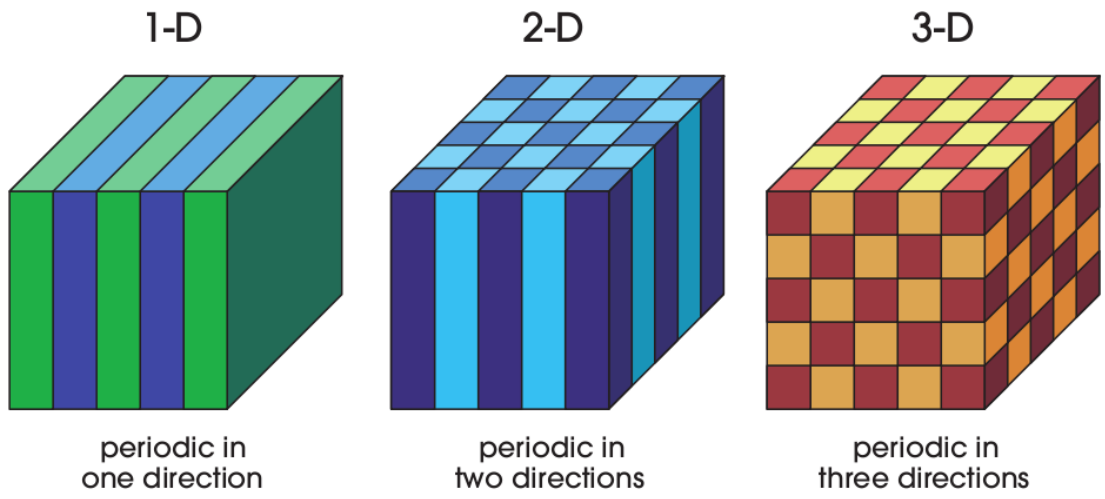

Figure 1.2 Simple Schematic of 1D, 2D, and 3D photonic crystal structures

Photons can propagate through this periodicity depending on their wavelengths. Propagation allowed wavelengths are called modes, and they form photonic bands. Inhibited groups of wavelengths form photonic bandgaps. PhCs affect light similar to how the periodic potential in a semiconductor crystal affects the electron motion; by allowing and forbidding electronic energy bands. After the publications of the idea of controlling light through the PhC in 1987 by Yablonovitch [3] and John [4], utilization of PhCs in various fields had been investigated. Since the basic physical phenomenon is

based on diffraction, the periodicity of the PhC structure has to be of the same length-scale as half the wavelength of the photon. Thus, they could not be applied to applications other than in the microwave range due to the difficulty in fabricating these structures at the scale for modulating optical wavelength. However, with recent developments in advanced fabrication techniques and tools due to the semiconductor industry, fabricating PhC structures in the optical range has become possible, and their uses in various applications are being explored extensively. These applications include, but are not limited to sensors for measuring pressure[5-10], strain, gas [11-13], chemical and more sensors [14-16], light enhancements [17], and fiber optics.

.

1.2.3 Optical Microcavities

Optical microcavities (OMCs) are composed of an optical medium layer (a cavity layer) sandwiched between two highly reflecting mirror layers and examples of OMC structures are shown in Figure 1.3.

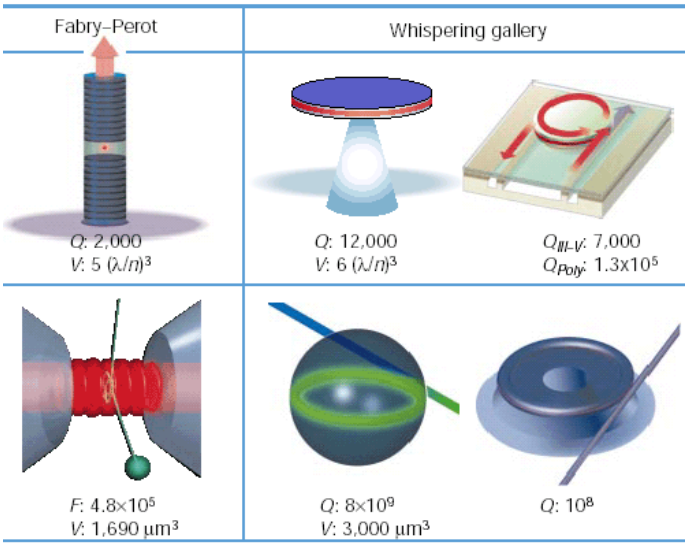

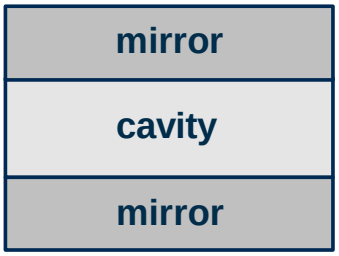

$$\lambda_0 = \frac{2}{m}(d_{cavity} n_{cavity})$$

Figure 1.3 Schematics of various OMC structures

For a given refractive index material, the thickness of the cavity layer in the OMC structure determines the resonant frequency, the cavity mode, the particular wavelength which can be transmitted. As the thickness increases, the number of cavity mode increases. Thus, the thickness of the cavity layer is usually only a few micron meters to the submicron range ensuring that cavity-modes are sparsely distributed. The advantage of the OMC structure arises from the well-defined cavity modes. Very narrow bands of wavelengths can be highly transmitted and the rest of the frequencies are highly reflected. OMCs have applications from a wide range of fields such as vertical cavity surface emitting lasers, cavity-enhanced single photon quantum dot emission and many other applications are being investigated [18, 19].

1.3 Background and Challenges and Research Objectives

1.3.1 Transparent nanocomposite scintillators

Currently, there are several kinds of scintillators that are used in medical imaging tools and high energy photon detectors. Scintillators made with micron-sized phosphors are efficient and bright, but spatial resolution is limited due to their strong light scattering. This causes significant light loss due to repeated scattering and self-absorption during propagation, especially through relatively thicker screens [20-23]. These scintillators are mostly used in detectors and they are not suitable for medical imaging or radiation therapy tools where the contrast and resolution are important. On the other hand, single crystalline scintillators such as SrI_2:Eu, $LaBr_3$:Ce and $Y_3Al_5O_{12}$:Ce can provide very high luminosity and spatial or energy resolution, but growth of these single crystals is difficult and time-consuming which makes them prohibitively expensive [24]. The most efficient scintillators are rare earth (RE) doped halide single crystals, which are hygroscopic and require housing in an air-tight enclosure. Furthermore, it is difficult to create large samples without developing a doping gradient, which causes non-uniform light yield and degrades resolution [25]. Hence, single crystalline scintillators have excellent performance suitable for medical imaging and radiation therapy tools but they are expensive. Thus, scintillators that can have adequate contrast and spatial resolutions for portal imaging tools with low materials and manufacturing costs would be competitive in current markets.

As a result, several kinds of scintillators have been reported. Single crystalline scintillators such as CsI or $CdWO_4$ can be constructed into thick pixelated arrays for high detective quantum efficiency (DQE) portal imaging at MV energies, but they have not

been commercialized due to their high costs. Recently, transparent ceramic scintillators, garnet systems, were reported as efficient scintillators [25, 26]. Typically, a cubic structure material which exhibits isotropic optical properties is required. These materials were made into nanoparticles, vacuum-sintered, and hot isostatically pressed into a transparent scintillator exhibiting scintillation properties comparable to single crystals. However, this fabrication technique is complex and expensive, and large-sized scintillators are difficult to obtain which limits their applications.

The alternative approach is using a novel transparent nanocomposite scintillator where nanocrystals responsible for scintillation are encapsulated in a robust glass matrix. They can be made at a fraction of the cost (~\$1/cm^3) with large scalability, and high thermal, chemical and mechanical stability. However, the current challenge of the transparent nanocomposite scintillators is the low light yield which prohibits them to be used in practical applications. While the performance of the nanocomposite scintillators may never be as high as the single crystalline scintillators, there is enormouse room for improvement with a systematic optimized approach.

1.3.2 Optical structures for dynamic loading sensors

The behavior of materials is significantly different under dynamic loading (shock) pressures than from their continuum behavior (under static loading conditions). This is especially true for a materials system consisting of heterogeneous particulate materials. Their response under dynamic loading is very complex and often driven by mesoscale features. There are several complicated events that occur due to material property mismatch, particle shape and size mismatches, impurities, inter-particle interactions and more [27-29]. For instance, in explosives, the system contains various microstructures of

HMX (Highly Melting eXplosive compound, also known as octogen) grains and a binder. Often times, there are formation of hot spots of high temperature and pressure which serve as reaction initiation sites [30]. It would be useful to know where and how these hot spots form to have more control over the reactions. Most of these studies are limited to simulation approaches. Since comprehensive understandings of the behaviors of such systems is deficient, the modelling work is also limited and unreliable. This is due to a lack of sensors/diagnostic tools with the desired spatial and temporal resolution that can give us some experimental results and information on the systems.

Current diagnostic tools that have a temporal resolution sufficient to capture the dynamic behavior of a material with nanosecond resolution are mostly limited in spatial resolution. For example, while piezoelectric/piezoresistive stress gauges have a nanosecond temporal resolution, they have a spatial resolution of only several millimeters providing an averaged response of the system [31]. Laser velocimetry systems such as the velocity interferometer system for any reflector (VISAR), provide a point spatial resolution defined by the diameter of the laser beam (~0.5 mm), which is not a complete representation of a system [32]. There are other techniques available such as line-VISAR and the optically recording velocity interferometer system (ORVIS) that can provide sub-mm spatial resolution but only along a one-dimensional line profile [33].

Thus, a current challenge is to develop shock sensors and/or diagnostic tools that are capable of providing information (such as stress or strain) with sufficient temporal resolutions (~ ns) and high spatial resolutions (better than sub-mm). Development of such sensors are critical to advance the understanding and knowledge of materials behaviors

under dynamic loading. Consequently, we can fully utilize the potential of materials to applications in extreme environments.

1.4 Research Objectives

There are two main objectives of this thesis: to improve the light output of the transparent nanocomposite scintillators and to design and fabricate photonic crystals and optical microcavity structures for dynamic loading sensing. The detailed objectives of the two main parts of the thesis are listed below.

For the transparent nanocomposite scintillators, the objectives are to investigate how the fundamental relationships between the glass matrices, choice of activators and sensitizers, nanoparticle concentration, doping concentrations, annealing conditions and temperatures, affect the formation of scintillating nanocrystals in the glass matrix and subsequently affect the light output under gamma-ray and x-ray excitation. To improve the light out-coupling of the emission light of the scintillator to PMTs (which can subsequently improve the light output), we will utilize a 2D PhC structure on the scintillators. Thus, we will investigate how the fundamental relationships between the materials properties, lattice arrangements, structural designs affect the photonic bandgap of the 2D photonic crystal structures and determine the appropriate fabrication methods to improve the light output of the scintillators. Such new knowledge may contribute to improvement of transparent nanocomposite scintillators that can aggressively be used in portal medical imaging tools.

For the dynamic loading sensors, the objectives are to specifically investigate and design 1D photonic crystal, distributed Bragg reflector multilayer structures and the asymmetrical optical microcavity multilayer structures to be used as dynamic loading sensors capable of providng adequate temporal and spatial resolutions. We will investigate the effect of the materials optical properties, and physical dimensions on the

spectral properties of the structures such as the peak intensity and full width half maximum of the characteristic peak. We will also consider the materials acoustic properties, and the fabrication compatibilities to obtain the optimal designs of these structures. Such successfully developed sensors can not only provide unprecedented sensing capabilities such as 2D spatial resolutions but as diagnostic tools can also help us understand the complex behavior of materials under shock pressure.

1.5 Map of Dissertation

This thesis reports (i) a robust synthetic approach for fabricating transparent nanocomposite scintillators for portal medical imaging tools and gamma ray detectors as well as the designs and fabrication approaches of (ii) distributed Bragg reflector and (iii) asymmetrical optical microcavities for the application of shock pressure sensing. Chapter 2 discusses the synthesis approach of $BaGdF_5$:Tb and GdF_3:Tb based transparent nanocomposite scintillators in various glass systems to fully identify the fundamental relationships between the light output and other conditions. In Chapter 3, the design approach and the fabrication process of SiO_xN_y 2D photonic crystals for enhancing the light out-coupling of the emission light of the scintillators are investigated. Chapter 4 studies specifically designed SiO_x distributed Bragg reflector multilayers for dynamic load sensing. Chapter 5 discusses the novel Al_2O_3 and SiO_2 asymmetrical optical microcavitiy structures for dynamic load sensing. Chapter 4 and 5 both describe the detail design and fabrication processes of these nanostructures. Lastly, Chapter 7 summarizes the main findings in each chapter and provides the recommendations for future research.

2. Transparent Nanocomposite Scintillators

Gyuhyon Lee, Christian Struebing, Brent Wagner, Christopher Summers, Yong Ding, Alex Bryant, Naresh Thadhani, Daniel Shedlock, Josh Star-Lack, and Zhitao Kang, "***Synthesis and Characterization of a $BaGdF_5$:Tb Glass Ceramic as a Nanocomposite Scintillator for X-Ray Imaging***", Nanotechnology, 2016, 27, 205203, Copyright © 2016 IOP Publishing.

Gyuhyon Lee, Nicholas Savage, Brent Wagner, Yuelan Zhang, Benjamin Jacobs, Hisham Menkara, Christopher Summers, and Zhitao Kang, "***Synthesis and luminescence properties of transparent nanocrystalline GdF_3:Tb glass-ceramic scintillator***", Journal of luminescence, 2014, 147, 363, Copyright © 2013 Elsevier B.V. Published by Elsevier B.V.

2.1 Introduction

A scintillator is a material that, when excited by ionizing radiation in the form of charged particles or gamma and X-ray, responds with the emission of UV or visible light. Currently, single crystalline scintillators such as SrI_2:Eu, $LaBr_3$:Ce and $Y_3Al_5O_{12}$:Ce can provide very high luminosity and spatial or energy resolution, but growth of these single crystals is difficult and time-consuming which makes them prohibitively expensive [24]. Most efficient scintillators are rare earth (RE) doped halide single crystals, which are hygroscopic and require housing in an air-tight enclosure. Furthermore, it is difficult to create large samples without developing a doping gradient, which causes non-uniform light yield and degrades resolution [25]. Single crystalline scintillators such as CsI or $CdWO_4$ can be constructed into thick pixelated arrays for high detective quantum efficiency (DQE) portal imaging at MeV energies, but they have not been commercialized due to their high costs. Recently, transparent ceramic scintillators, garnet

systems, were reported as efficient scintillators [25, 26]. Typically, a cubic structure material which exhibits isotropic optical properties is required. These materials were made into nanoparticles, vacuum-sintered, and hot isostatically pressed into a transparent scintillator exhibiting scintillation properties comparable to single crystals. However, this fabrication technique is complex and expensive, and large-sized scintillators are difficult to obtain which limits their applications.

Nanocomposite scintillators made from nanocrystals encapsulated in transparent matrices such as a glass matrix can be made at a fraction of the cost (~\$1/cm^3) with large scalability. While the performance of the nanocomposite scintillators will not be as high as for crystalline scintillators, contrast and spatial resolution are expected to be adequate for portal imaging at MeV energies, with the advantage that the material and manufacturing costs are expected to be reduced by over 10 times. In addition, when halide nanoparticles are embedded in a glass matrix as in a glass ceramic, they have improved thermal, chemical and mechanical stability [20, 22, 23, 34-36]. Because the halide nanocrystals are significantly smaller in size than the wavelength of the scintillation light, there is negligible light scattering and the glass shows the high transparency of a single crystal. Compared to a completely amorphous glass scintillator, the embedded nanocrystals may be able to provide higher light yields and scintillator densities. Due to these benefits, nanoparticles embedded in a glass matrix have garnered considerable scientific interest over the past decade for other applications such as white light emitting diodes, laser material, etc. [37, 38]. However, to replace currently used scintillators for high performance X-ray imaging applications, the light yield of nanocomposite scintillators must be improved.

Light yields of transparent nanocomposite scintillators can depend on many factors such as the volume fraction of nanocrystals to glass matrix, choice of nanocrystals and glass compositions. For instance, the desired glass matrix should have low phonon energy to minimize non-radiative recombination, few intrinsic traps that can reduce light output, and a high density for sufficient stopping power for high-energy applications. Many studies have been reported on various glass matrix systems such as the silicate, oxyfluoride, fluoride, and phosphate systems [39]. High volume fraction of nanophosphor particles in a glass matrix while maintaining transparency is critically important to achieve the highest light yield. This can be achieved by: 1) homogenous distribution of nanocrystal growth below the critical size (generally 1/5th of wavelength of interest) to minimize scattering according to Rayleigh-Gans-Debye and Hendy's Theory, or 2) minimizing the difference in refractive indices between glass and nanocrystals (index matching) [40]. The former approach, which controls the growth of nanocrystals, is often done by adding nucleation agents (such as TiO_2 and ZrO_2) [41]. The latter approach is complex and difficult to achieve [42, 43]. Lastly, in order to improve light yield, the choice of nanocrystals is important. Previously, different nanocrystals have been examined with many related to this study including GdF_3 [44], $BaGdF_5$ [45], $BaYF_5$ [46-48], and $BaLuF_5$ [49]. Y^{3+} and Lu^{3+} are not as efficient sensitizers for X-rays as Gd^{3+}. Also, GdF_3 and $BaYF_5$ nanoparticles formed in glasses are tetragonal structure, so their refractive indices are anisotropic. This limits their particle size and the resulting volume ratios possible as their refractive index cannot be matched to the matrix. However, $BaGdF_5$ nanocrystals exhibit cubic structure, which means the refractive index is isotropic and can be matched to the matrix. The refractive index of

$BaGdF_5$ is not yet reported in literature but it is expected be between the refractive index of BaF_2 (n=1.48) and GdF_3 (n=1.59) and the glass composition can be tuned to modify the refractive index in this range [50, 51]. Furthermore, $BaGdF_5$ doped with Tb has exhibited a high quantum efficiency due to the quantum cutting effect through cross-relaxation and subsequent direct energy transfer [52]. Huang et al. has reported that Tb doped glass ceramic containing $BaGdF_5$ nanocrystals can be prepared with enhanced luminescence properties [53]. However, they did not thoroughly evaluate the system to improve nanocrystal formation and enhance scintillation performance to develop it as an efficient nanocomposite scintillator.

This chapter seeks to identify the factors that affect the light yield of transparent glass ceramic nanocomposite scintillators and to investigate how to improve the light yield by controlling these factors. For instance, two different nanocrystals materials, GdF_3:Tb and $BaGdF_5$:Tb, were grown by different annealing conditions and their effects in scintillation performance are compared. Likewise, several approaches were evaluated to improve the light yield of the transparent nanocomposite scintillator. Also future research directions for optimizing the transparent nanocomposite scintillators in portal imaging tools are provided.

2.2 Experimental

Transparent Tb doped GdF_3 and $BaGdF_5$ glass ceramic nanocomposite scintillators were prepared via a melt-quench method followed by annealing. Robust aluminosilicate glass was selected as the matrix material to encapsulate nanocrystals. Other glass matrices such as lead based and germanium based were also considered but

not chosen due to their high phonon energy and high cost respectively. The composition of samples was systematically investigated with ratios of raw materials adjusted as following for GdF_3 and $BaGdF_5$ scintillators: $40SiO_2$-$26Al_2O_3$-15NaF-$16GdF_3$-$3TbF_3$ and $45SiO_2$-5Al2O_3-$24BaF_2$-(10-z)NaF-zCsF-$2yTbF_3$-(12-x-y)Gd_2O_3-$2xGdF_3$ ($0\leq x\leq 5$, $0\leq y\leq 4$, $0\leq z\leq 10$) respectively. Several other glass systems were also investigated: $34SiO_2$-16PbO-$16Al_2O_3$-20NaF-$10GdF_3$-$4TbCl_3$ for lead oxide based glass matrix, $25B_2O_3$-$50GeO_2$-$19Gd_2O_3$-$6TbF_3$ for germanium oxide based glass matrix, and $20SiO_2$-$33B_2O_3$-$15BaF_2$-$26Gd_2O_3$-$6TbF_3$ for borosilicate based glass matrix. High purity powders of raw materials consisting compounds responsible for glass matrix and nanocrystal were carefully weighed to a total mass of approximately 20 g and thoroughly mixed. The mixture was loaded into a covered alumina crucible and placed in a box furnace for melting. The box furnace was heated to 1400 ℃ and held at that temperature for 3 hours in air or an argon atmosphere. An error of ±1 ℃ was expected for all temperature controls. The mixture was quenched by pouring into a 500 ℃ pre-heated graphite mold and then slowly cooled down to room temperature. The density of each sample was measured using the revised Archimedes' principle. Various annealing studies were done from simple annealing to two-step annealing between 550-700 ℃ for 1-24 hours in order to promote the nanocrystal nucleation and growth inside the glass matrix. Over 100 samples were prepared and their optical, structural and scintillation properties were characterized.

Photoluminescence (PL) and photoluminescence excitation (PLE) spectra measurements of bulk or powdered samples were carried out using a Spex1000M spectrometer with a 150W Xe lamp/monochromator combination as the excitation source. Luminescence decay measurements were obtained using a 355 nm tripled Spectra-Phyics

YAG:Nd 10 ns pulsed laser as the excitation source and a Tektronix DSA 602A oscilloscope to collect the transient decay signal. Absorption spectra measurements were performed using a Cary 5000 UV-VIS-NIR Spectrophotometer. X-ray images were acquired under 6 MeV X-ray irradiation using a Varian Clinac with a modified AS1000 portal imager. Gamma ray excited brightness was measured by wrapping the sample with reflecting Teflon tape on its sides and on the face that would be exposed to the radiation source. Optical coupling was accomplished by applying optical grease to the exposed face and placing onto a Hamamatsu R669 photomultiplier tube (PMT). The PMT was connected to a current meter to directly read the relative light output signal from the excited sample. The radioactive isotope point sources used for the gamma ray tests were 0.1 μCi Cobalt-60 and 0.1 μCi Manganese-54. To obtain more accurate optical results (to minimize the surface effect), scintillators were polished to a similar volume and mass.

X-ray diffraction (XRD) spectra were obtained on finely powdered samples using an X'pert Pro Alpha-1 to check the crystallinity of nanoparticles and their particle size. Differential scanning calorimetry (DSC) analysis was performed using a Netzsch DSC 404 F1 to obtain the crystallization kinetics of the system. Scans were performed 20 ℃/min up to 800 ℃ under 45 ml/min ultra-high purity argon flow. Pieces between 10-20 mg were measured in an Al_2O_3 lined Pt-Rh crucible with a Pt-Rh lid in a SiC furnace. Baseline corrections were performed with empty crucibles. Using the FEI Tecnai F30 Transmission Electron Microscope (TEM), high magnification bright-field images and selected-area electron diffraction (SAED) patterns from powdered samples were gathered to assess the crystallinity of nanoparticles embedded in the glass matrix. Further,

the composition of nanoparticles were revealed by X-ray energy dispersive spectrography (EDS) in scanning transmission electron microscopy (STEM) mode.

2.3 Results and discussion

Transparent nanocomposite scintillators were successfully prepared. Typical samples under 365 nm UV light and 6 MeV X-rays can be viewed in Figure 2.1 and its inset image, respectively. The dimensions of most samples were about 22.0 ± 1.5 mm in diameter and 9.5 ± 1.0 mm in thickness. Compositions of glass matrix and crystal components were systematically optimized to enhance scintillator performance. Two sets of samples which exhibited efficient scintillation properties, GdF_3:Tb nanocrystal based, and $BaGdF_5$:Tb nanocrystal based are discussed in detail in this thesis.

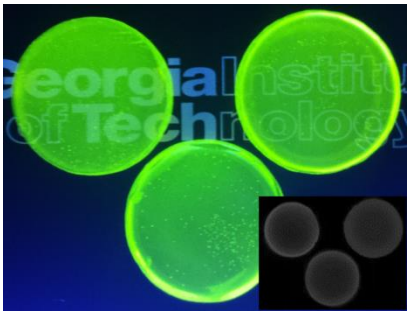

Figure 2.1 Images of successfully fabricated transparent nanocomposite scintillators under UV lamp with inset image under 6 MeV X-ray.

2.3.1 Optical Characterization

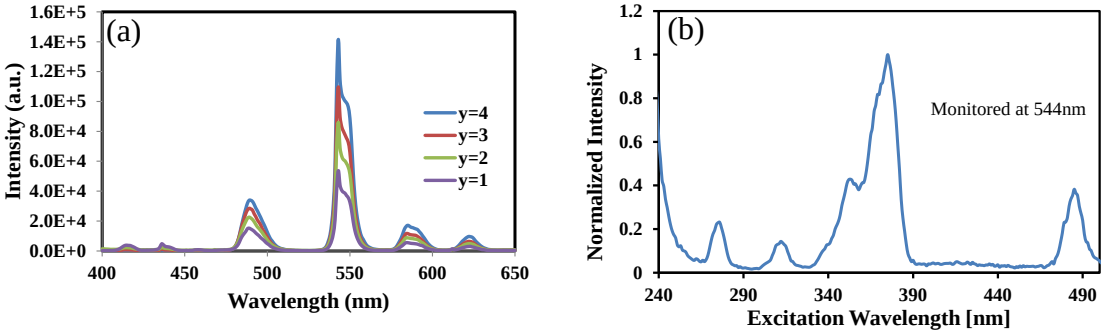

Figure 2.2 (a) PL spectra of $BaGdF_5$ nanocrystal based scintillator samples with different Tb doping concentration; y denotes to molar amount of Tb in raw composition and (b) PLE spectra of the 2% Tb doped $BaGdF_5$ based sample

Figure 2.2 (a) shows the photoluminescence (PL) spectra of $BaGdF_5$ nanocomposite scintillators synthesized with different Tb doping concentration. It should be noted that the GdF_3 PL and PLE spectra are very similar and follow the same trends to the $BaGdF_5$'s PL and PLE spectra as the rare earth ions are identical for both scintillators. For main emission peaks located at 491, 543, 586 and 623 nm in visible range are attributed to the $^5D_4$ to ^7F_J (J = 6, 5, 4, 3) energy transitions in Tb^{3+} ions [44, 52, 54]. The emission occurring at 543 nm is the most intense and accounts for the vibrant green color observed under ultraviolet light (Figure 1). Increases in PL peak intensities were observed with increasing Tb doping concentrations. X-ray radiation results on $BaGdF_5$ samples (Table 2.1) follow a similar trend as PL intensity, where scintillation performances are enhanced with increased Tb doping concentrations from y=1 to y=4. As Tb doping concentration increases, the higher light output under X-ray is observed both per unit mass and per unit volume. About 60% higher light output per unit volume was observed from the y=4 doped sample compared to the y=1 doped one. An example of the photoluminescence excitation spectrum of the $BaGdF_5$ sample monitored at 543 nm is presented in Figure 2.2 (b). The 273 nm and 312 nm excitation peaks are due to the

excitation in Gd^{3+} from $^8S_{7/2}$ to ^6I_J and ^6P_J energy levels respectively. The excitation bands observed around 351 and 373 nm are attributed to the 4f transitions in Tb^{3+}, which contribute to the main visible Tb^{3+} emissions peaks. The excitation peak at 485 nm is also due to the Tb absorption from ^7F_J to $^5D_4$ energy levels. The 273 nm and 312 nm excitation peaks are clearly shown by monitoring the intense 543 nm Tb^{3+} emission line which suggests efficient energy transfer between the Gd^{3+} and Tb^{3+} ions similar to the previously reported result on Gd^{3+} and Ce^{3+} containing scintillators materials [55, 56].

Table 2.1 X-ray radiation results on BGFT scintillators

Sample	Mass [g]	Volume [cm^3]	Density [g/cm^3]	Relative light output/volume
$BaGdF_5$:Tb (y=1)	8.635 ± 0.0005	1.986 ± 0.0005	4.347 ±0.001	1.000 ±0.004
$BaGdF_5$:Tb (y=2)	5.769 ± 0.0005	1.392 ± 0.0005	4.144 ±0.002	1.152 ±0.006
$BaGdF_5$:Tb (y=3)	10.779 ± 0.0005	2.562 ± 0.0005	4.208 ±0.004	1.438 ±0.007
$BaGdF_5$:Tb (y=4)	9.985 ± 0.0005	2.351 ± 0.0005	4.247 ±0.001	1.613 ±0.004

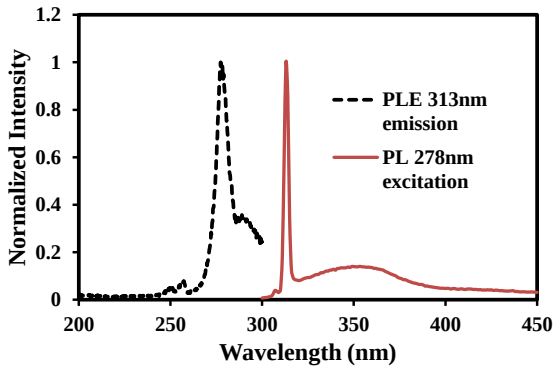

Figure 2.3 PL and PLE spectra of undoped GdF_3 glass-ceramic sample

Figure 2.3 shows the PL and PLE spectra of GdF_3 transparent nanocomposite scintillator without any Tb doping. Under 278nm excitation, the PL spectrum exhibits a main peak at 313 nm and a broad emission band from 350-450nm. As discussed previously, the main 313nm peak is due to a well-documented energy transition between the ^6P_J to $^8S_{7/2}$ levels within Gd^{3+}. As expected, peaks resulting from the energy transtions of the Tb^{3+} ions are not observed and thus the sample does not show any green color emission under a UV light. Also, the PLE spectrum confirms the 278 nm Gd^{3+} excitation peak when monitoring the emission at 313nm.

2.3.2 Glass Matrix Comparisons

As mentioned in the experimental section, several other glass systems were investigated. Table 2.2 shows the list of the investigated glass systems with the respective molar compositions of samples with the highest light output under gamma-ray excitation.

Table 2.2 Gamma-ray excitation results on other scintillator systems with GdF_3 or $BaGdF_5$ nanocrystals in different glass matrices

Glass matrix	Molar composition	Density [g/cm^3]	Relative light output/volume	
			Cs-137	Co-60
Lead Oxide	$34SiO_2$-$16PbO$-$16Al_2O_3$-$20NaF$-$10GdF_3$-$4TbCl_3$	3.91	0.33	0.36
Germanium Oxide	$25B_2O_3$-$50GeO_2$-$19Gd_2O_3$-$6TbF_3$	4.78	1.22	1.36
Borosilicate	$20SiO_2$-$33B_2O_3$-$15BaF_2$-$26Gd_2O_3$-$6TbF_3$	4.68	1.55	1.77
Aluminosilicate	$45SiO_2$-$5Al_2O_3$-$24BaF_2$-$10NaF$-$12Gd_2O_3$-$4TbF_3$	4.21	1.9	1.84

As it can be easily deduced from the result on Table 2.2, the lead oxide based glass system was the least efficient and the alluminosillicate based glass system was the most efficient in terms of the light output under the gamma-ray excitation. This is mostly

attributed to the high density of the system. But it can also be contributed to the lead oxide based system which inhibits the efficient energy transfers. The germanium oxide based glass system showed promising results but it was not further pursed due to the high raw materials cost. Therefore, we decided to extensively focus on the alluminosilicate based glass system.

2.3.3 GdF_3 and $BaGdF_5$ nanocrystal comparisons

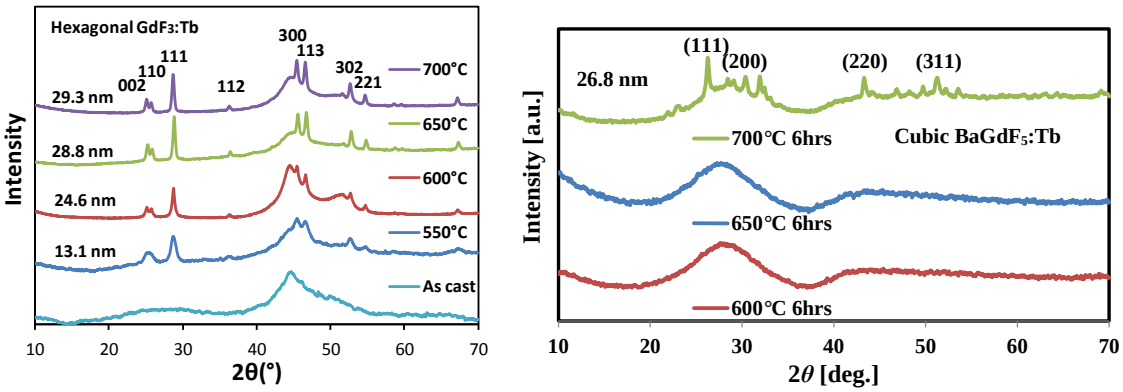

Figure 2.4 XRD spectra of both GdF3 (left) and BaGdF5 (right) nanocrystal based scintillators collected at respectively different annealing temperatures.

Both GdF_3 and $BaGdF_5$ nanocrystals were successfully embedded in the aluminosilicate glass which was confirmed by the XRD spectra as shown in Figure 2.4. It should be noted that the GdF_3 nanocrystals start to form at a much lower annealing temperature (~at around 550 ℃ vs 700 ℃ for the $BaGdF_5$ nanocrystals). For $BaGdF_5$, no sign of peak representing crystalized particle formation (nanocrystal nucleation & growth) is observed even at 650 ℃.

Subsequently, both sets of scintillators were optimized in terms of raw material composition and the annealing condition that gave the highest light yield without losing the transparency of the sample. Their performances in gamma ray radiation were examined (shown in Table 2.3).

Table 2.3 Gamma ray radiation results on GdF_3 and $BaGdF_5$ nanocrystal based scintillators.

Sample	Volume [cm^3]	Density [g/cm^3]	Relative light output/volume		Relative light output/mass	
			Cs-137	Co-60	Cs-137	Co-60
GdF_3	3.298 ±0.0005	3.213 ±0.0005	1.000 ±0.001	1.000 ±0.003	1.000 ±0.001	1.000 ±0.003
$BaGdF_5$	3.113 ±0.0005	4.208 ±0.0007	2.125 ±0.002	1.844 ±0.003	1.623 ±0.002	1.408 ±0.004

The $BaGdF_5$ nanocrystal based scintillator has a higher density, 4.208 g/cm^3, than the GdF_3 nanocrystal based scintillator, 3.213 g/cm^3. With a higher density, the $BaGdF_5$ based scintillators have higher gamma-ray absorption cross-sections to achieve increased gamma-ray stopping power and increased rate of events of gamma-rays transferring energy to electrons which increase the overall light output. Thus, the higher light output per unit volume observed in $BaGdF_5$ based scintillators under gamma ray excitation can be partially attributed to a higher density. However, the observed light output per unit mass was also higher which suggests that more phosphor crystals are present in the $BaGdF_5$ based scintillators. This is possible as $BaGdF_5$ crystal is cubic structure, which means it has an isotropic refractive index. Therefore, with refractive matching, larger nanocrystals can be formed without causing scattering. Whereas for GdF_3 nanocrystal based scintillators, index matching is not possible and the size of the grown nanocrystal is limited. Higher light output per unit mass observed for $BaGdF_5$ based scintillators can also be contributed to the $BaGdF_5$ itself, where nanocrystals are more efficient phosphors

during ionization excitation due to an effect similar to quantum cutting as observed by Tzeng et al. [52]. They observed that when $BaGdF_5$ is doped with Tb, through many cross-relaxation and subsequent direct energy transfer, a quantum efficiency of > 100% can be achieved when Tb^{3+} is excited by high energy UV photons. Therefore, for the rest of this chapter, we have focused on working with Tb doped $BaGdF_5$ nanocrystal based scintillators to maximize the improvement of the light output and the scintillation properties.

2.3.3. $BaGdF_5$ nanocrystal based scintillator with GdF_3 nucleation agent

As discussed in the earlier section, the light yield of the scintillator depends on the volume of the nanocrystals embedded in the glass matrix. Thus, to improve the nucleation rate and concentration of $BaGdF_5$ nanocrystal formation, we have introduced GdF_3 into the raw material composition and the two sets of the scintillators, $BaGdF_5$:Tb glass ceramic with GdF_3 (denoted as BGFTGF) and without GdF_3 (BGFT) are compared in detail. It should also be noted that the BGFTGF scintillator exhibited very similar PL and PLE spectra as the GdF_3 based scintillators and the $BaGdF_5$ based scintillators (BGFT) shown in the previous section.

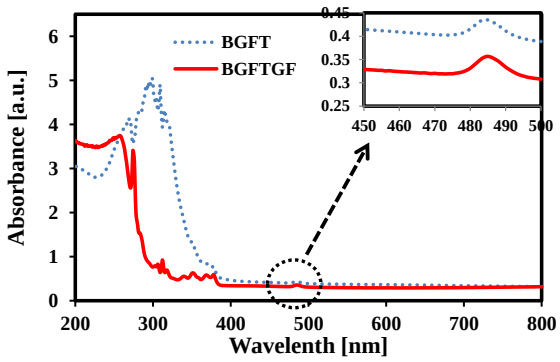

Figure 2.5 Absorption spectra of y=4 Tb doped BGFT and BGFTGF samples.

Comparing the absorption spectra of y=4 Tb doped BGFT and BGFTGF samples (Figure 2.5), the BGFTGF sample shows a blue-shift in the absorption edge (from 380 nm to 300 nm) indicating the increase in transparency at shorter wavelengths. This can be attributed to fewer defects presented in the glass matrix and/or improved nanocrystal precipitation in the glass with better index match when GdF_3 was added. Higher fluoride content from added GdF_3 can also influence electronic transitions in the glass which primarily affects absorption in the shorter wavelength region. For both samples, observed Tb absorption intensities at 485 nm are similar as shown in the enlarged inset of Figure 2.5. Between samples with the same glass composition and different Tb doping concentration, it was determined that the absorption intensities at 485 nm mainly depend on Tb doping concentrations with a positive correlation and the cut-off edges in absorption remained at about the same location. This confirms that the difference in UV absorption region does not result from the Tb doping but from the glass matrix and nanocrystals.

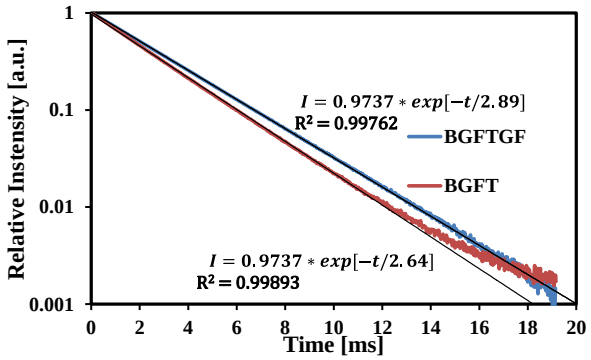

Figure 2.6: Decay results of y=4 Tb doped BGFT and BGFTGF samples.

The decay curves of y=4 Tb doped BGFT and BGFTGF samples measured at 543 nm (Figure 2.6) can be fitted well to single exponential functions such as $I = I_o \exp\left[-\frac{t}{\tau}\right]$. Estimated decay times, τ, are 2.64 ms and 2.89 ms for BGFT sample and BGFTGF sample with R^2 value of 0.99893 and 0.99762 respectively (R^2 is the coefficient of determination, indicating how well the data fit the function). It is observed that the decay time was negligibly affected by the Tb doping concentration, but 250 μs longer decay time was observed from the BGFTGF sample. The shorter decay time exhibited in BGFT sample can indicate higher defect concentration in the sample, which may have presented in both the glass and embedded nanocrystals. Defects can effectively act as non-radiative recombination sites which induce light loss. Since there is more non-radiative recombination in the system, a faster quench of luminescence is observed. A glass ceramic system with more nanocrystals will exhibit less defect concentration and longer decay time. From these results, it was determined that the BGFTGF sample exhibits longer decay time due to the system with fewer defects and more efficient nanocrystals as confirmed by XRD measurements.

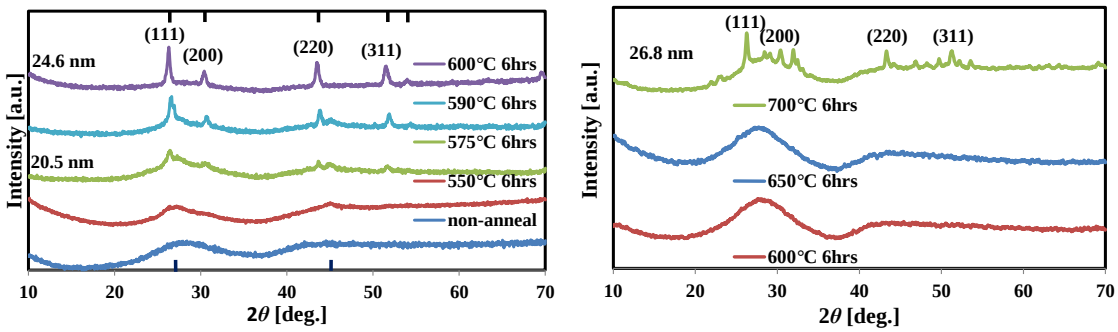

Figure 2.7 XRD spectra of BGFTGF:y=3 (left) and BGFT:y=1 (right) samples at different annealing conditions; top marker represents $BaGdF_5$ peak positions and bottom marker represents small peaks that are suspected to be responsible by (110) and (300) of GdF_3

Table 2.4 XRD analysis on BGFTGF:y=3 and BGFT:y=1 samples.

hkl	111	200	220	311	222
$2\theta_{BGFTGF}$ [°]	26.293	30.404	43.503	51.526	53.974
a_{BGFTGF} [Å]	5.866	5.875	5.879	5.878	5.880
$2\theta_{BGFT}$ [°]	26.192	30.274	43.208	51.129	53.499
a_{BGFT} [Å]	5.888	5.899	5.917	5.920	5.928
$2\theta_{JCPDS:\ No\ 24\text{-}0098}$ [°]	25.651	29.655	42.401	50.373	52.551
a_{BaGdF5} [Å]	6.010	6.020	6.025	6.003	6.028

The XRD spectra of BGFTGF (y=3) samples and BGFT (y=1) samples (Figure 2.7) are presented at respectively different annealing temperatures. Above their respective highest temperatures, scintillators started turning semi-transparent. For both sets of samples, XRD results confirm the formation of the cubic $BaGdF_5$ crystals when peak positions are compared to the reported data (JCPDS: No 24-0098) [45, 53, 54]. The size of nanoparticles were estimated using the Scherrer formula; $D_{hkl} = \frac{K\lambda}{\beta cos\theta}$, where λ = 0.154056 nm is the wavelength of Cu*K*a radiation, θ is the Bragg angle of X-ray diffraction peak, β is the full width at half-maximum of the diffraction peak and the constant K = 0.90. The approximate crystal size of the BGFTGF sample which annealed

at 600 ℃ was calculated to be 24.6 nm whereas the BGFT sample which annealed at 700 ℃ was estimated to be 36.8 nm. Also, the lattice parameter, a, of $BaGdF_5$ was calculated using the Bragg equation, $2\frac{a}{\sqrt{h^2+k^2+l^2}}sin\theta = n\lambda$. The calculated lattice parameters (shown in Table 2.4) for both sets of samples are very similar and only slightly different from the JCPDS reference data. This discrepancy can be due to Tb doping, where about 1.4% smaller in radius Tb atom substitutes a Gd atom and modifies the unit cell. Another noticeable distinction between BGFT and BGFTGF samples is the difference in the required annealing temperatures to precipitate $BaGdF_5$ nanocrystals. BGFT samples required a higher annealing temperature of 700 ℃. As a result, there are unwanted impurity phases present in the XRD spectra which can explain the previously observed results: less transparency in lower wavelength region from absorption spectra (Figure 2.5) and shorter decay time (Figure 2.6). Furthermore, the amorphous backgrounds present in the XRD spectra of BGFT samples are relatively high compared to the peak intensities. The volume fraction of $BaGdF_5$ was calculated to be 33.4% for the 700 ℃ annealed sample based on the ratio of integrated peak intensity to the amorphous background. BGFTGF samples required a lower annealing temperature and XRD peaks begin to appear at 575 ℃. It should be noted that additional small peaks at 26 ° and 45 ° which are present in the 575 ℃ and 590 ℃ samples as shown in Figure 2.7 (a) are also shown in Figure 2.4(a). These are the characteristic peaks for the hexagonal GdF_3 nanocrystals ((110) and (300) for 26 ° and 45 ° respectively) [55]. At 600 ℃, these peaks are not present. It is presumed GdF_3 nanocrystals nucleated at a lower temperature such

as 575 °C and acted as nucleation seeds for the growth of $BaGdF_5$ nanocrystals at higher temperatures. The volume fraction of $BaGdF_5$ nanoparticles was calculated to be 37.4% for the 590 °C BGFTGF sample, signifying a higher volume fraction of nanocrystals was obtained while maintaining the transparency by utilizing the GdF_3 nucleating agent.

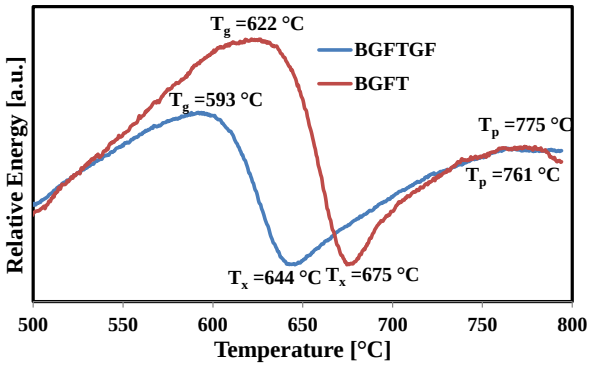

Figure 2.8 DSC thermograms of y=3 Tb doped BGFT and BGFTGF samples at 20 °C/min heating rate.

DSC analysis was performed on y=3 Tb doped BGFT and BGFTGF samples to identify and differentiate the crystallization kinetics of each system (Figure 2.8). The glass transition temperature, T_g, the onset temperature of crystallization, T_x, and the peak temperature of crystallization, T_p, for the BGFTGF sample are determined to be 593 °C, 644 °C, and 761 °C respectively, similar to previously reported results by Karmakar et al. [45]. BGFT sample has T_g, T_x, and T_p at 622 °C, 675 °C and 775 °C respectively. However, Zhang et al. reported these values to be much lower for $BaGdF_5$ nanocrystals [38]. This deviation can be attributed to the difference in the system and the lower heating rate used which generally lowers these temperatures. Regardless, this DSC result

confirms that the addition of GdF_3 lowers the crystallization temperature and further strengthens the idea of GdF_3 performing as a nucleating agent.

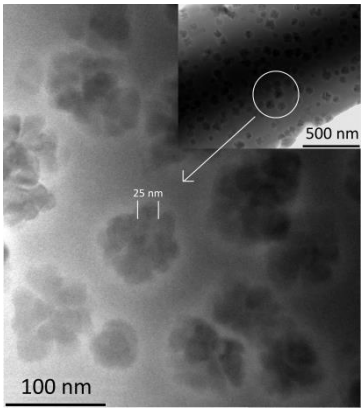

Figure 2.9 TEM images of the BGFTGF:y=3 sample, top inset image shows SAED pattern and bottom inset image shows low magnification TEM image revealing uniform distribution of nanoparticles.

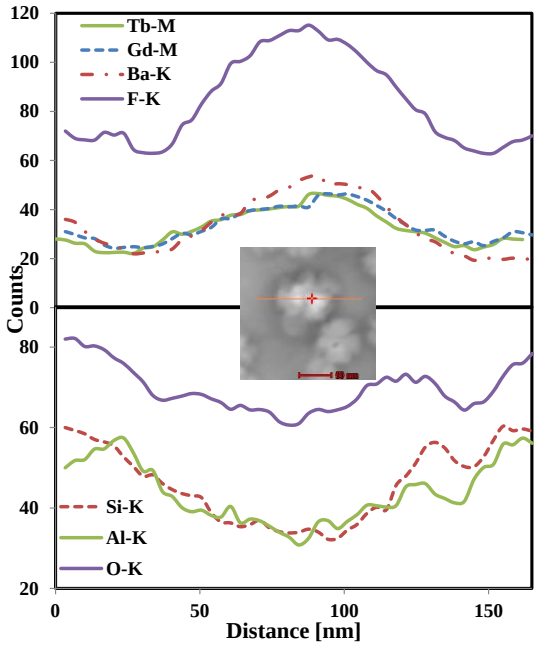

Figure 2.10 EDS scanning profile in STEM mode for various elements in the typical BGFTGF scintillator sample

In addition, high magnification images were captured utilizing TEM to confirm the formation of nanocrystals. The BGFTGF (y=3) sample was prepared into powders

using a mortar and pestle and suspended in isopropanol that was deposited and dried on a TEM grid. The bright-field image in Figure 2.9 clearly represents the embedded $BaGdF_5$ crystals in a glass matrix with a cluster particle size < 100 nm, but each cluster was composed of several smaller grains of 20-30 nm, which is in agreement with the XRD result. The inset lower magnification image (top right) reveals the uniform distribution of these nanocrystals. In spite of the relatively large size of the cluster, the scintillator remained transparent signifying a close refractive index matching between the nanocrystals and the glass matrix. Encouragingly, Berthier et al demonstrated that glass ceramic with high volume fraction could remain transparent despite having large crystal size of ~8 μm by index matching [43]. With a larger crystal size, it is possible to achieve a higher light output due to less surface defects. For more accurate analysis, EDS spectra (Figure 2.10) were collected on the sample. The inset image demonstrates the annular dark-field STEM image with the redline representing a scanning profile. As the scanning profile hovers over the nanoparticle, the EDS results display increased counts of elements in the $BaGdF_5$:Tb nanoparticles, such as Ba, Gd, Tb, and F and decreased counts in the glass matrix, Si, Al and O. This result further confirms that the formed nanocrystals are indeed $BaGdF_5$:Tb nanocrystals.

Table 2.5 Gamma ray radiation results on GdF_3 and $BaGdF_5$ based scintillators

Sample	Volume [cm^3]	Density [g/cm^3]	Relative light output/volume		Relative light output/mass	
			Cs-137	Co-60	Cs-137	Co-60
GdF_3	3.298 ±0.0005	3.213 ±0.0005	1.000 ±0.001	1.000 ±0.003	1.000 ±0.001	1.000 ±0.003
BGFT (x=0, y=3)	3.113 ±0.0005	4.208 ±0.0007	2.125 ±0.002	1.844 ±0.003	1.623 ±0.002	1.408 ±0.004
BGFTGF (x=2, y=3)	2.431 ±0.0005	4.217 ±0.0009	2.444 ±0.005	2.318 ±0.007	1.862 ±0.002	1.766 ±0.005

Table 2.5 shows the comparison of all the discussed transparent nanocomposite scintillators in gamma ray radiation: GdF_3 nanocrystal, $BaGdF_5$ nanocrystal (BGFT), and $BaGdF_5$ nanocrystal with GdF_3 nucleation agent (BGFTGF). As discussed in the earlier section, $BaGdF_5$ nanocrystal based scintillators exhibited superior (at least 2 times higher) relative light output in gamma ray compared to GdF_3 nanocrystal based scintillators due to higher density, higher nanocrystal volume to glass matrix and quantum cutting effect. When comparing between BGFT and BGFTGF ($BaGdF_5$ based sample with and without GdF_3 nucleation agent), BGFTGF sample exhibited a higher light output in both per unit mass and per unit volume. This is attributed to the higher crystalline volume ratio for better energy transfer between matrix and Tb^{3+} dopants and less defects present in the system as shown from previous section. As the XRD and DSC results confirmed, GdF_3 helped nucleation of $BaGdF_5$ crystals at a lower temperature. As a result, $BaGdF_5$

nanocrystals are more uniformly distributed and formed efficiently increasing the crystalline volume ratio. In addition, decay and absorption results confirmed that the BGFTGF system has fewer defects in the system which improves the light yield. Therefore, despite the minimal density difference, the BGFTGF sample exhibited a higher light output under gamma ray excitation.

2.4 Conclusion

Transparent nanocomposites scintillators were synthesized by a melt-quench method followed by annealing to precipitate GdF_3:Tb and $BaGdF_5$:Tb nanocrystals in an aluminosilicate glass matrix. Efficient energy transfers between Gd^{3+} and Tb^{3+} ions were observed in both GdF_3 and $BaGdF_5$ based scintillators. The luminescence intensity was enhanced with increasing Tb doping concentration as confirmed by PL and X-ray imaging results. Gamma ray results confirmed that $BaGdF_5$ based scintillators are more efficient than GdF_3 based scintillators due to their higher density, increased nanocrystal volume compared to glass matrix, and quantum cutting effect. GdF_3 was added to the $BaGdF_5$ nanocrystal based scintillator raw material before the melt-quenching procedure to increase the nucleation rate. A blue-shift in absorption edges and a slower decay time observed in the sample with added GdF_3 suggests that there are fewer defects in the glass matrix and nanocrystals. The XRD results confirmed the formation of $BaGdF_5$ nanocrystals after annealing. With the addition of GdF_3, the glass ceramic scintillators required a lower annealing temperature (700 ℃ -> 600 ℃) to precipitate $BaGdF_5$ nanocrystals. Also, a higher nanocrystal to matrix volume fraction could be achieved due to a more uniform homogeneous distribution of nanoparticles. DSC results confirmed that the addition of GdF_3 lowered glass transition temperature, onset crystallization

temperature and peak crystallization temperature. The formation of nanocrystals was confirmed by TEM and clusters near 100 nm in size were observed which consisted of 20-30 nm sized grains. In spite of the relatively large cluster size, the sample remained transparent probably due to close index matching between the glass matrix and nanocrystals. The nanoparticles' compositions were confirmed by EDS. Gamma-ray results indicated that the performance of the $BaGdF_5$ nanoparticle based scintillators was further improved with GdF_3 added as a nucleating agent. This is mostly attributed to the increased volume ratio of nanoparticles (33.4% -> 37.4%) from accelerated homogeneous nucleation. These results indicate that with GdF_3 added, higher nanoparticle volume fractions can be achieved. With improved light yield from higher volume fractions, these materials and the method can be very suitable for a wide range of X-ray imaging applications.

3. 2D Photonic Crystal for light extraction enhancement

3.1 Introduction

An additional area of utilizing photonic crystal (PhC) is improving the performance of optical devices. When a layer of PhC with appropriate photonic band structure is placed on top of a light emitting device, it can direct the emitted light to be more vertical. Thus, an optimized design can improve light extraction of a device using the guided mode of the PhC. For example, a significant fraction of light generated in a medium of high refractive index material is trapped due to total internal reflections. For light emitting diodes (LEDs), the out-coupling (extraction) efficiency is very low. There have been many rigorous studies on employing a surface PhC on LEDs. Oder et al. demonstrated 63% and 95% improvement in performance for group III-nitride blue and UV LEDs respectively, with 2D surface PhC fabricated using electron-beam lithography [17]. Such encouraging results have sparked investigations of using a surface PhC on LED. Many fabrications techniques that can be scaled up were explored such as nano-imprint lithography [57], nanospheres lithography [58], and holographic lithography [59]. Furthermore, other applications and the use of PhC structure to enhance their performances were investigated. For instance, Xu et al. have examined the use of PhC structures on organic light emitting diodes [60]. Not only did the PhC structure improve the light extraction efficiency, but the anisotropy effect of light extraction was also clearly observed. There have also been some simulation studies and experimental results demonstrating the enhancement of scintillator performance with the use of PhC structures.

Knapitsch et al. reported extensive simulation studies on the effects of surface PhC structures on scintillators and experimentally confirmed the improvements [61-63]. Also, Zhu et al. used a hexagonal monolayer array of polystyrene nanospheres as a surface 2D PhC layer and achieved an increase in extraction efficiency of 25% [64]. These results suggest the promising potential of PhC structures for light extraction enhancement in various optical applications.

In this chapter of the thesis, we report an investigation of the use of 2D surface PhCs on the transparent nanocomposite scintillators that were investigated and optimized in the previous chapter. Despite the improvements reported in the previous chapter, the light output under X-ray or gamma-ray excitation was still low compared to single crystalline scintillators. The use of the 2D surface PhC is expected to have more direct light emission with less total internal reflection which should improve the light out-coupling to the PMT and thus the scintillation performance (light output under X-ray or gamma-ray) as shown in Figure 3.1.

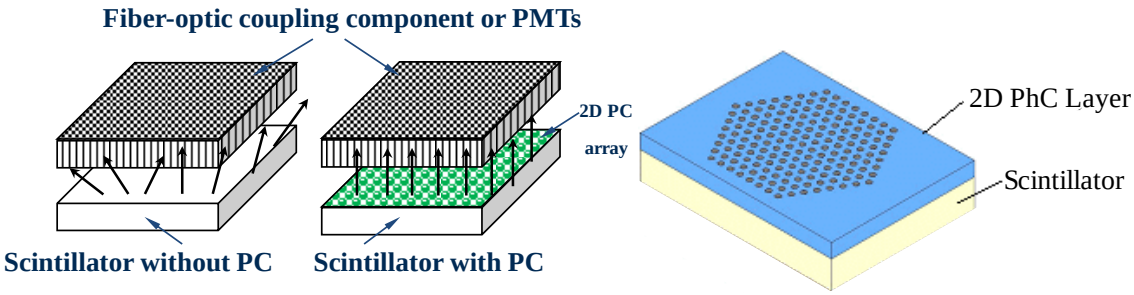

Figure 3.1 Schematics of the transparent nanocomposite scintillator without and with a 2D PhC surface layer: (a) the emission is expected to be more vertical with the 2D PhC which helps the out-coupling into the PMTs (b) close up view of the scintillator structure with the 2D PhC layer.

Various 2D surface PhC designs and the effect of materials were first studied using a simulation approach. PhCs are periodic structure having a lattice constant ‘a’ and a hole size ‘d’. There are several structural factors (designs) that can affect the propagation of the light for 2D surface PhC. For example, the periodic structures (cylindrical holes or pillars) can be arranged in two different lattices; triangular (or hexagonal) and square. Other factors that affect the photonic bandgap are the refractive index of the 2D PhC material, air filling ratio (or the radius of the cylindrical holes/pillars to lattice constant, a, ratio). Thus, the optimal design should be selected to have the widest photonic bandgap at 543 nm (emission wavelength of the transparent nanocomposite scintillators from Chapter 2). Also the fabrication method should come into consideration. Since the periodicity of the 2D PhC structures must be similar in length scale to the wavelength of the light to be guided, advanced nanoscale fabrication techniques such as e-beam lithography and reactive ion etching were investigated. The fabrication was first optimized on a commercially available glass substrate and the 2D surface PhC structure was characterized. Lastly, the 2D surface PC was fabricated on the transparent scintillator.

3.2 Simulation Approach

The photonic bandgap of the 2D PhC structures were simulated using MIT Photonic Bands (MPB) package. Effects of various parameters such as refractive index, diameter of a feature, spacing and the lattice type of the arrays were investigated in order to maximize the photonic bandgap at a specific wavelength (λ = 543 nm, the emission wavelength of the transparent nanocomposite scintillator). The optimal 2D PhC design

was then selected in consideration of the easiness of fabrication, and material compatibility, while maximizing the photonic bandgap at 543 nm.

3.2.1 Array Arrangement

From the previous simulation work, it was found that the hexagonal lattice is better than the square lattice in terms of the photonic bandgap; the hexagonal lattice has a full wider bandgap than the square lattice [2]. Also, from the fabrication point of view, hexagonal lattice is easier to fabricate than the square lattice. For the same air to filling ratio, the spacing between two adjacent holes, a-2r, (where a is lattice constant and r is the radius of the hole) is longer for the hexagonal lattice than the square lattice. This is important especially during the etching fabrication process. When we transfer the pattern into the underlying layer, we use a mask layer. Typically, the mask layer and the underlying layer have different etching rates under the same recipe as they are made of different materials. For instance, a typical polymer mask layer etches ~ 4-5 times faster than the hard mask (metal) layer. So to etch a pattern into 100 nm of hard mask layer, it is required to deposit a 400~500 nm thick polymer layer. When the spacing between the two adjacent holes (a-2r) is too small ~ 50 nm, this polymer layer can be unstable as its aspect ratio is too high (~10). Therefore, for the same air to filling ratio, it would be easier to fabricate in the hexagonal lattice than the square lattice as it would have longer spacing between the two adjacent holes (thus lower aspect ratio). For these reasons, we decide to only investigate the 2D PhC with the hexagonal lattice of cylindrical holes.

3.2.2 Air Filling Fraction (Radius to Spacing ratio)

The effect of the radius to lattice constant, r/a (or air filling fraction), on photonic bandgap width was studied for an infinite thick 2D PhC slab with an hexagonal array of cylindrical holes for dielectric constants of 2.402, 4 and 6 for PhC material using MPB.

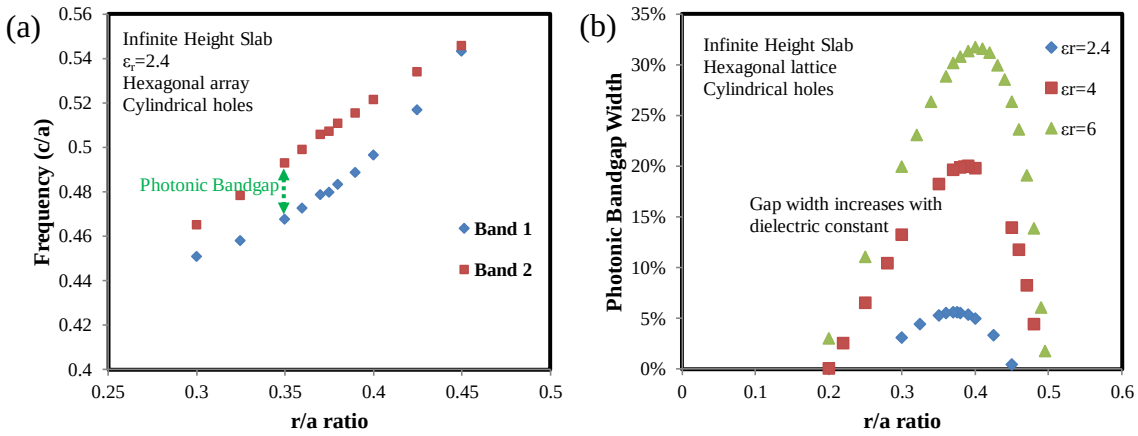

Figure 3.2 a) Simulated frequency of the photonic band level 1 and 2 for infinite height 2D PhC slab with dielectric constant of 2.402, hexagonal array of cylindrical air holes b) simulated photonic bandgap width between photonic bands 1 and 2 with different dielectric constant for infinite height 2DPhC slab with hexagonal array of cylindrical air holes

Fig. 3.2 (a) shows the frequency (which is in units of c/a and thus, the corresponding wavelength is a/f_c) of photonic bands 1 and 2 for different r/a ratios for a PhC structure with a dielectric constant of 2.402. It is clearly shown that the frequency of the photonic band 2 increases linearly with r/a ratio whereas the frequency of the first photonic band follows an exponential or 2^{nd} order polynomial function. Overall, it is apparent that there is an optimum r/a ratio for the maximum photonic bandgap between photonic bands 1 and 2. Thus, the photonic bandgap width was computed for different r/a values for dielectric constants of 2.402, 4 and 6 as shown in Fig. 3.2 (b). For all three dielectric values, the bandgap width initially increases to a maximum value but decreases

after a certain ratio which is different for all three cases considered. However, it should be noted that the optimal value lies between 0.35 to 0.45 and increases with the dielectric constant. Therefore, it was concluded that we should determine the optimal dielectric constant value (refractive index) for the PhC material in order to also select the optimal r/a ratio.

3.2.3 Dielectric Constant (Refractive Index)

The effect of the dielectric constant ε_r (or refractive index for non-magnetic material, $n = \varepsilon_r^{1/2}$) on photonic bandgap width was studied on an infinite height 2D PhC slab with an hexagonal lattice of cylindrical holes with the radius of the holes, r, to spacing, a, ratio of 0.4.

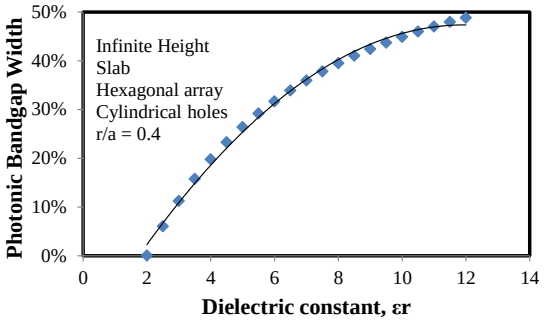

Figure 3.3 Photonic bandgap area in %, for a hexagonal lattice of cylindrical holes with a r/a ratio of 0.4

The photonic bandgap width between photonic bands 1 and 2 for an infinite thick 2D PhC slab with a hexagonal lattice of cylindrical holes as a function of dielectric constant is plotted as Fig. 3.3. Fig. 3.3 clearly shows that the photonic bandgap width between photonic bands 1 and 2 increases with increasing photonic crystal dielectric constant. It may seem that using a high refractive index material for the PhC would be an appropriate choice as it maximizes the photonic bandgap. However, as we are using this

2D PhC on top of the transparent nanocomposite scintillators to improve the light out-coupling to PMT, the optical interfaces between the PhC layer and the scintillators as well as the PhC layer to air must be considered. To eliminate the internal reflection between the scintillator and the PhC layer, the refractive index of the PhC must be greater than or equal to the refractive index of the scintillators. Also, as shown from the Eq. (3.1) below, the refractive index of the PhC material should not be too high.

$$\theta_c = \arcsin(\frac{n_{air}}{n_{PhC}}) \tag{3.1}$$

which was derived from Snell's Law ($n_1 \sin\theta_i = n_2 \sin\theta_t$) assuming $\theta_t = 90°$.

In Eq. (3.1), the critical angle, θ_c, decreases as n_{PhC} increases. Any incident light on the interface with incident angle greater than the critical angle would be experience total internal reflection. Therefore, a high refractive index would require all the guided light exiting the PhC layer to be close to vertical (very low angle of incident) or else all of the guided light will be reflected internally. Therefore, to fully understand the effect of the refractive index of the PhC material (the benefit of maximizing the photonic bandgap while considering the total internal reflection and the vertical emission), we should consider looking at a different simulation tool with the capability of simulating the reflectance/transmission spectrum. For our studies, we have decided to use $n_{PhC} = 1.55$ for the rest of the simulation approach as the refractive index of the transparent nanocomposite scintillator is expected to be between the refractive index of BaF_2 (n=1.48) and GdF_3 (n=1.59). This approach can ensure that there is no new optical interface introduced by the PhC layer which can complicate the analysis and it makes the comparison between the scintillator with and without the PhC layer relatively easy.

3.2.4 Optimized Design

The 2D PhC structure in terms of the lattice (hexagonal or square), dielectric constant (refractive index) and the ratio between radius of the holes to unit spacing (r/a) were optimized to enhance the light output of the transparent nanocomposite scintillators. To properly waveguide the emitted light from the scintillators, the photonic bandgap was maximized for 543 nm (emission wavelength of the scintillators under radiation) with the material having the same refractive index as the scintillator to eliminate the optical interface ($n_{PhC} = 1.55$). This structure would have a hexagonal lattice of cylindrical air holes with radius to unit spacing ratio of 0.365.

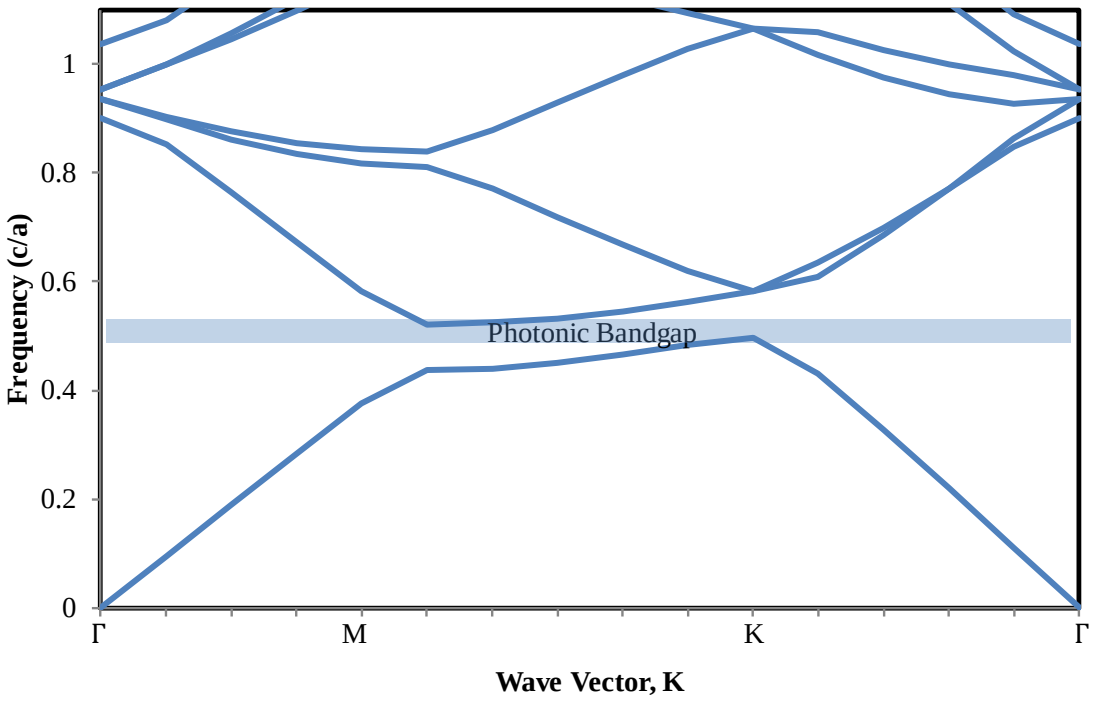

Figure 3.4 Photonic band structure of a 2D PhC infinitely thick slab with a hexagonal array of holes with a relative dielectric constant of 2.4 (n = 1.55) and r/a ratio 0.365

Figure 3.4 shows the simulated photonic bandgap of the optimized 2D PhC slab design. Between photonic bands 1 and 2, there is a photonic bandgap at a frequency (in

units of c/a) 0.509. The value of 0.509 when converted to a wavelength of 543 nm requires the unit spacing to be 276 nm ($a = f_c * \lambda$). This means for an 0.365 r/a spacing, the radius of the cylindrical air hole should be 101 nm to properly guide the emitted light from the scintillators. With a r/a spacing value of 0.365 and the unit spacing of 276 nm, the frequency of photonic bands 1 and 2 can be converted to wavelength; 557 nm and 529 nm, respectively. If the structure is fabricated as designed, this means the 2D PhC structure will have a photonic bandgap as wide as 28 nm, from 529 nm to 557 nm which will cause any light with wavelength between that range to escape the structure in the z-direction.

3.3 Fabrication Approach

To achieve the simulated design, the 2D PhC structure was first fabricated on a commercially available glass substrate. This was necessary in order to develop and optimize the fabrication process. For the fabrication, a top down approach utilizing electron-beam lithography (EBL) and inductively coupled plasma reactive ion etching (ICP-RIE) was used over a bottom up self-assembly approach in order to minimize the structural defects which can be easily present in the latter approach.

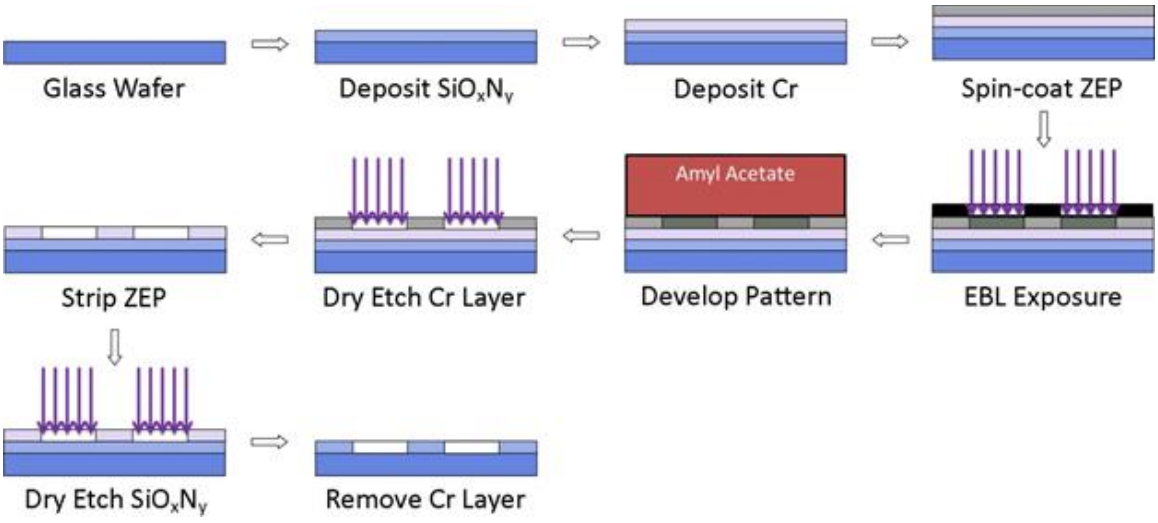

Figure 3.5 Schematic flow diagram of the 2D PhC slab fabrication process

Figure 3.5 shows the schematic flow diagram of the fabrication processes used to deposit a base material and create a pattern to develop a 2D PhC slab which was designed through simulations. For PhC base material, SiO_xN_y was selected as its refractive index depends on the atomic composition and values of n = 2.04-1.47 (at λ = 500 nm) can be achieved [65, 66]. For this study, a 500 nm thick SiO_xN_y layer was deposited using IAD as it is possible to easily and accurately vary the gas (oxygen and nitrogen) flow rate to change the atomic composition. It can deposit very smooth surfaces. A 150 nm thick Cr layer was deposited using e-beam evaporation to be used as a hard mask layer. Cr was used because it is compatible (no surface adhesion issue between interfaces) to SiO_xN_y and the particular EBL resist we used (ZEP) and also because it has a high etch selectivity to SiO_xN_y layer. ZEP was spin-coated at 2500 RPM for 60 seconds and baked for 2 minutes at 180 ℃ to form a 400 nm thick resist layer. 2 mm by 2mm patterns of hexagonal array of cylindrical holes were patterned using EBL. Various dosages were tried to create a pattern to meet the design specification (276 nm spacing with 101 nm radius). The pattern was developed on ZEP resist using amyl acetate for 2 minutes and

washed using iso-propanol and was transferred to the Cr layer using ICP RIE with Cl_2 as the etching gas. The pattern on the Cr hard mask layer was subsequently transferred to the SiO_xN_y PhC layer using ICP RIE with CF_4 and C_4F_8 gasses. After the successful pattern transfer to SiO_xN_y, the remaining Cr and ZEP layers were removed using wet-etching and acetone, respectively. Throughout each fabrication step, the transferred pattern was validated using SEM (scanning electron microscope), and a profilometer. The PhC layer was also physically characterized using AFM and optically characterized to confirm its light perturbation property.

3.4 Results and Discussions

The hexagonal array of cylindrical holes was patterned using a square beam pattern instead of a circle pattern as it greatly reduces the e-beam exposure time. Thus, the e-beam exposure dosage had to be optimized in order to obtain circular holes after the exposure and pattern transfer steps.

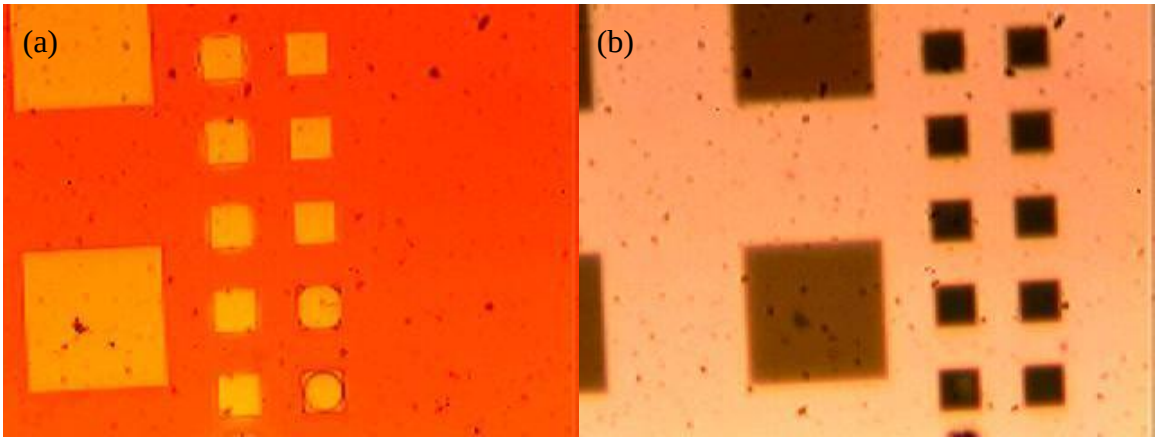

Figure 3.6 Optical Microscope Image of dosage array after (a) e-beam exposure and (b) pattern transfer to the Cr hard mask layer

Fig. 3.6 shows optical micrographs of the dosage test arrays that were performed. As can been seen more clearly from Fig. 3.6 (a), depending on the e-beam dosage, different deposited patterns can be obtained. The dosage was varied by 20 from 60 to 300 $\mu C/cm^2$.

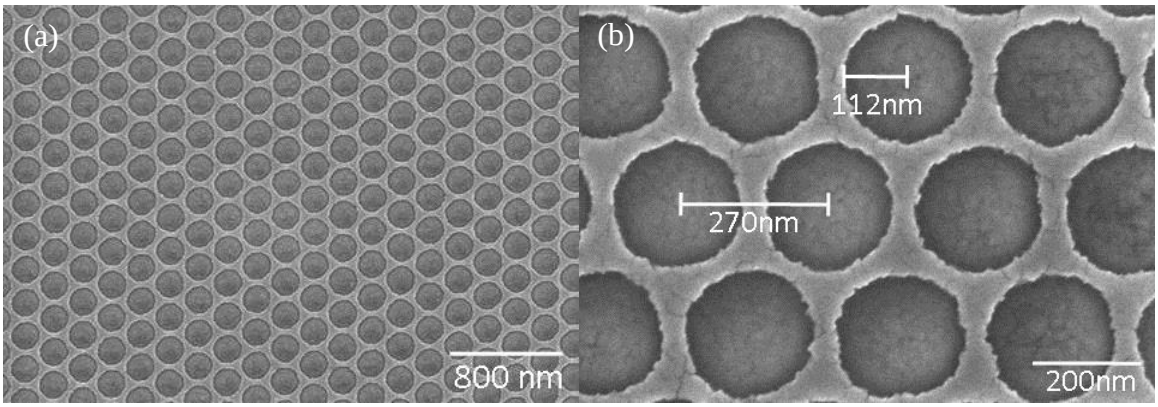

Figure 3.7 SEM micrographs after the pattern was transferred from the ZEP resist to the Cr hard mask layer

Fig. 3.7 shows the SEM micrographs taken after the array of circle patterns was exposed and developed in the ZEP resist and then transferred to the Cr hard mask layer by ICP RIE. Fig. 3.7 (a) clearly shows that the pattern was successfully transferred without any noticeable defects (no circular hole missing in the array) and Fig. 3.7 (b) shows that the transferred patterns have accurate unit spacing (a) compare to the design specification (270 nm vs 276 nm) and the radius of the hole is comparable to the design specification (112 nm vs 101 nm). The transferred pattern has a larger radii of circles most likely due to the ICP RIE process. The ICP RIE etching recipe was designed to be as vertical (for most anisotropic etching) as possible, but it appears that a little isotropy caused the size discrepancy.

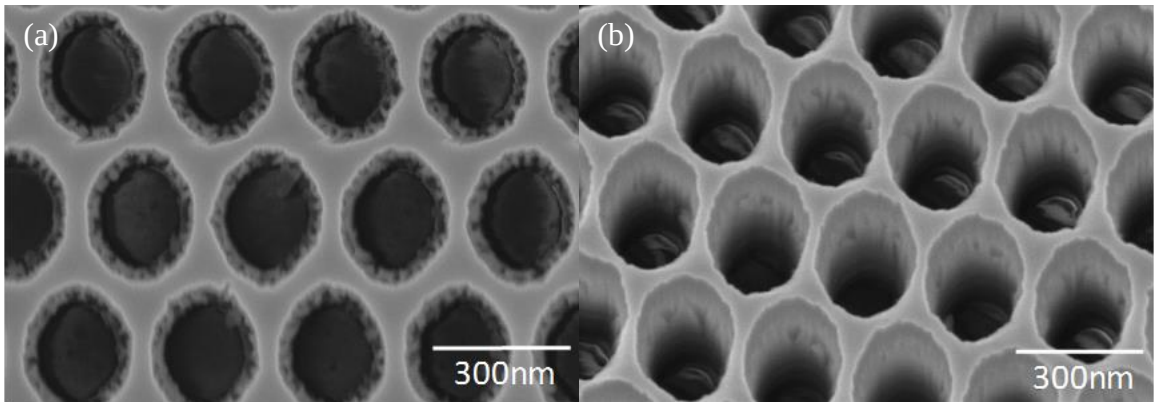

Figure 3.8 SEM micrographs after the pattern was transferred from the Cr hard mask layer to SiO_xN_y PhC layer

Fig. 3.8 shows the SEM micrographs taken after the PhC pattern was etched into the underlying SiN_xO_y layer by ICP RIE. This clearly shows that the pattern was successfully transferred. The angled view shown in Fig. 3.8 (b) reveals that the layer is etched all the way through as it shows deep holes in SiO_xN_y layer (which is 500 nm thick vs 150 nm of Cr). Fig. 3.8 (a) further confirms the success of this fabrication process and is defect free in creating 2D PhC patterns in a SiO_xN_y layer.

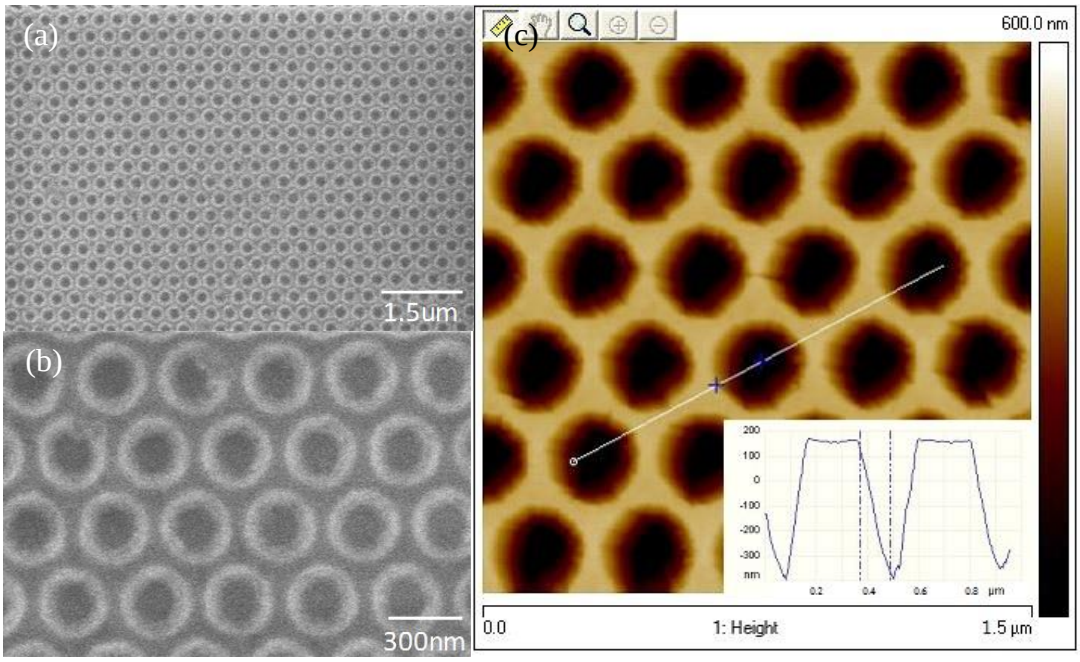

Figure 3.9 (a, b) SEM micrographs after remaining Cr and ZEP layers have been removed (c) AFM micrograph of the array with an inset figure showing the depth profile

Fig. 3.9 shows SEM and AFM micrographs of the fabricated 2D PhC patterns on the SiO_xN_y layer after the ZEP resist and the Cr hard mask layers were removed. SEM micrographs could not be taken at high resolution mostly due to the non-conductive SiOxNy material layer. However, it clearly shows that the array of circles is patterned well in the SiOxNy layer without any noticeable defects. Fig. 3.9 (c) shows the AFM micrograph and the scan profile across the array. It demonstrates that the depth of the circular hole is around 500 nm as expected. The depth profile shows the relatively sharp side wall profile obtained on the circular holes. However, the slope is most likely due to the shape and the size of the AFM tip relative to the feature size (the tip was too large compared to the feature size and could not accurately depict the sidewall profile). The SEM and AFM micrographs show that the proposed fabrication process was developed

adequately to fabricate a designed 2D PhC structure (hexagonal array of cylindrical holes with diameter 202 nm and spacing of 275 nm).

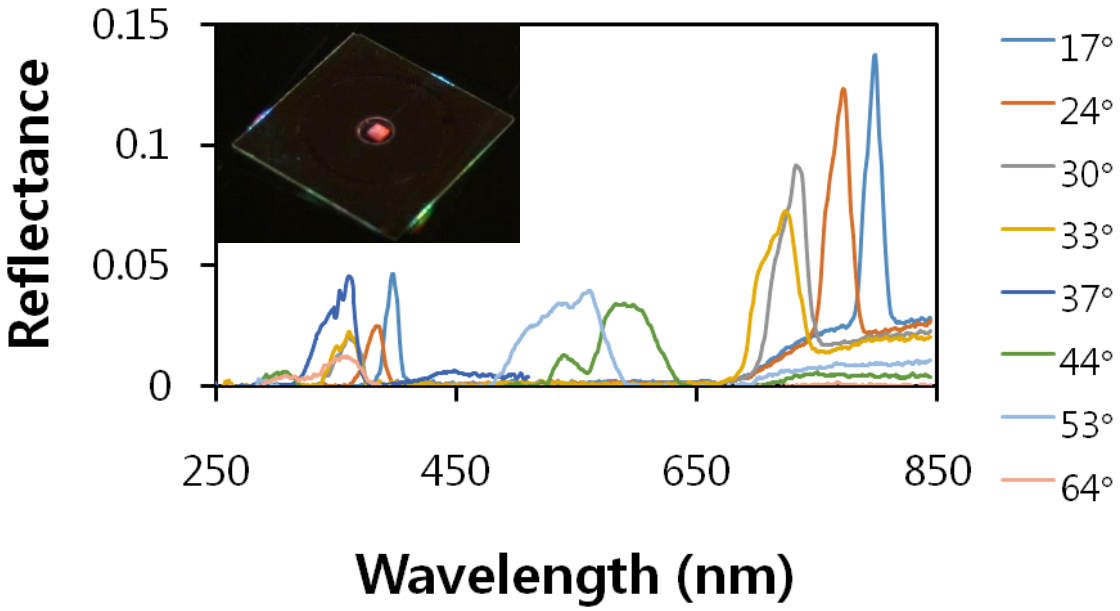

Figure 3.10 Reflectance spectra taken varying sample angles. Inset image shows the PC sample under white light illumination

Fig. 3.10 shows the reflectance spectra of the fabricated 2D PhC structure on a glass substrate taken at various sample angles. As clearly shown in the figure, the increase in measurement angle causes a blue shift in the reflectance spectra and a decrease in its intensity as expected since the optical path between holes increases causing a shift in photonic bandgap. Also, as the angle decreases, a secondary peak starts to appear in the UV-blue range which could be due to the photonic bandgap between the second and third photonic bands. The inset image shows the fabricated PhC sample under white light illumination. However, this result does not accurately represent if the fabricated 2D PhC structure is operating in the way that it was designed to work; whether 543 nm light is guided through the 2D PhC structure (as 543 nm is the emission

wavelength of Tb doped transparent nanocomposite scintillators). Therefore, there needs to be an experiment with a 543 nm laser light with varying incident angles to see if there is a difference between the sample with and without 2D PhC structure. If it guides correctly, then it should guide 543 nm wavelengths with high incident angle through the structure (whereas for the one without 2D PhC, it would either not propagate due to total internal reflection or pass through the structure at a shallow angle that the light is not near the PMT/or certain distance apart aperture)

Subsequently, using the developed and optimized fabrication processes, 2D PhC structure were successfully fabricated on a transparent nanocomposite scintillator. However, the limitation was realized during the fabrication. One of the equipment tools, the JBX-9300FS EBL tool has the dimension limit (specifically height limit of ~5 mm) on the sample size. This was not identified in the earlier fabrication process development stage as the commercially available glass wafers were only 0.5 mm thick. However, the typical transparent nanocomposite scintillators were at least 10 mm thick. This is required to ensure that the scintillators have enough cross-sectional area for sufficient x-ray or gamma-ray stopping power. As a result, the light output measured for samples thinner than 5 mm were unreliable and the enhancement made by 2D PhC structure was minimal. Thus, it was required to investigate an alternative fabrication approach such as nanoimprint lithography which can accommodate a thicker substrate.

The 2D PhC structure was first investigated to enhance the light output of transparent nanocomposite scintillators. However, during this process, it was quickly realized that the 2D PhC structure could also be used in an alternative application such as high speed strain/stress (dynamic loading) sensors. As observed, the 2D PhC structure

has the ability to perturb the propagation and refraction of select wavelengths of light which depends strongly on the lattice spacing and the feature size. Under applied stress/strain, these dimensions would change and the wavelength of light affected by the 2D PhC would also change. By monitoring the change in the color (wavelength) of the light as well as the position of the light, we could correlate this to the structural change and the applied pressure. Thus, it was realized that when developed accurately, that 2D PhCs can be used as dynamic loading sensors.

3.5 2D Photonic Crystal for dynamic loading sensors

Various patterns of 2D PhC structures were fabricated using the identical fabrication processes developed from the earlier studies on commercially available glass substrates: the square lattice of pillars, and holes. We fabricated these structures with varying lattice constants from 1.0x to 1.4x. This was done in order to simulate the effect of pressure loading (compression) on the 2D PhC structures.

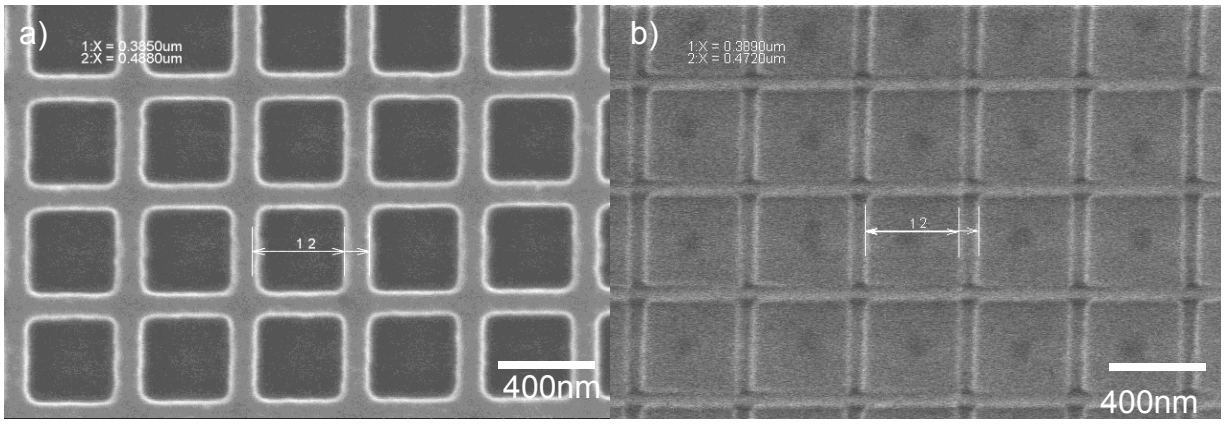

Figure 3.11 SEM micrographs of 2D PhC structures: (a) a square array of square holes and (b) a square array of square pillars

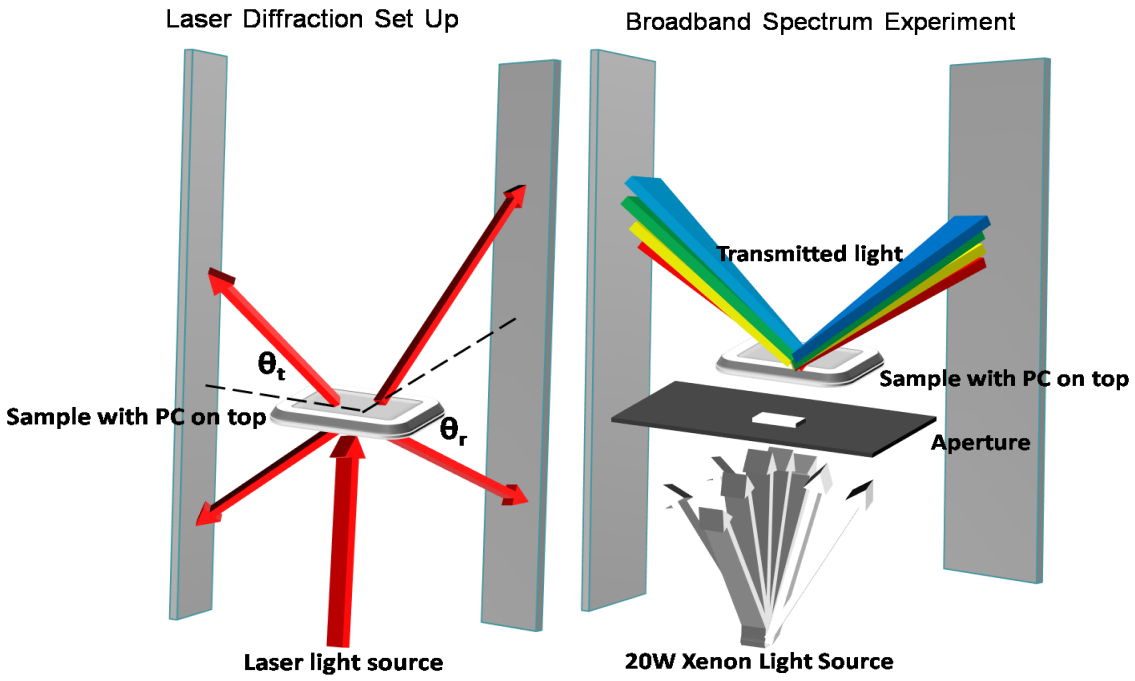

Figure 3.12 Diffracted light angle measurement using coherent laser sources and the rainbow spectra collection setup using an incoherent white light source for 2D PhC structures

The successfully fabricated structures are shown in Figure 3.11. It should be noted that the SEM micrograph is not well resolved for the case of pillars (Figure 3.11 (b)) due to the sample being non-conductive (as the layer surrounding the pillars is glass). To assess the refractive and diffracted properties of the 2D PhC structures, they were illuminated by several laser sources and white light. The characterization setup is shown in Figure 3.12. The angles of diffraction for reflected and transmitted light by the 2D PhC structures were measured using both coherent laser light sources (green (532 nm) and blue (460 nm) laser sources) and an incoherent white light source.

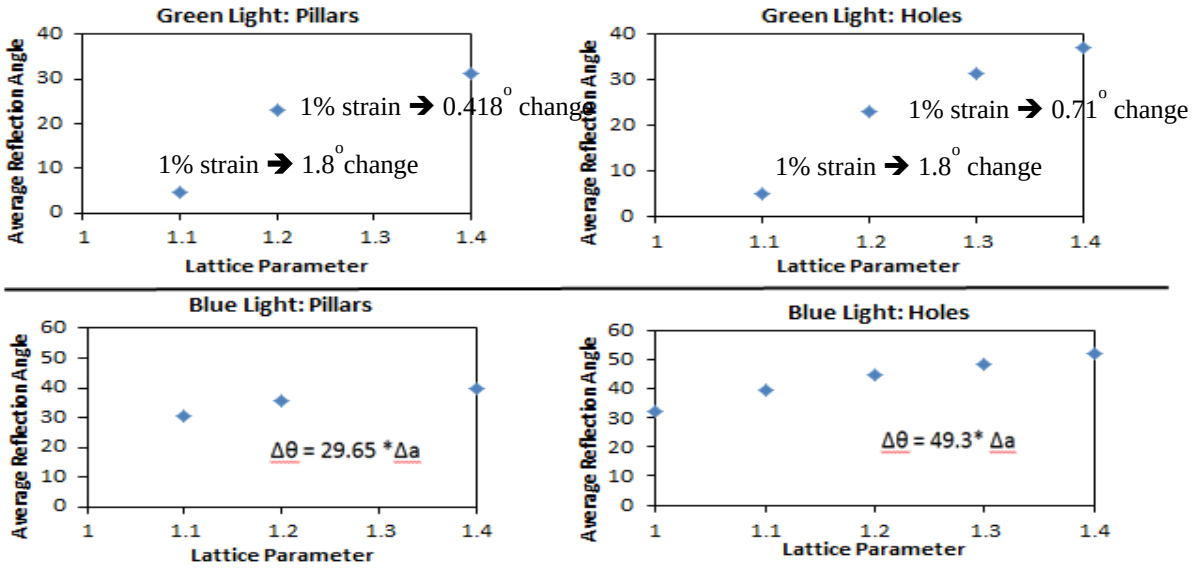

Figure 3.13 Diffraction angle of green (532 nm) and blue (460 nm) coherent radiation source by 2D square lattice PhC structures

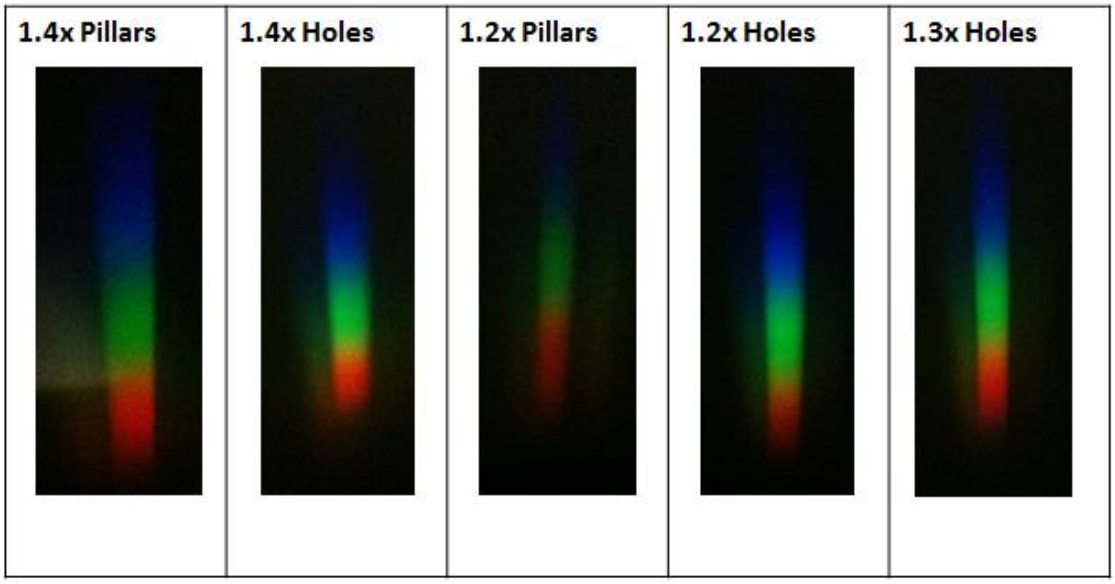

Figure 3.14 Diffraction of incoherent white light source by 2D square lattice PhC structure displaying rainbow spectra for PhCs with different lattice constants and geometries

Figure 3.13 shows the dependence of the diffraction angle of coherent radiation by the 2D PhC structures with varying lattice parameters from 1.0x to 1.4x. For both hole and pillar structures, the increase in lattice parameters increased the angle of reflected

light for both green and blue light. For the green laser source, the change in the refraction angle induced by the change in the lattice parameter ($\delta\lambda/\delta a$) is greater for the first 10% than the rest ($\delta\lambda/\delta a$ = ~1.8 for the first 10% lattice parameter change, whereas for the next 10~20% lattice parameter change, it is ~0.418 for the pillars and ~0.71 for the holes). Under the blue laser source, $\delta\lambda/\delta a$ is consistent throughout the whole lattice parameter changes but is generally lower than the green light (~0.33 for pillars and ~0.5 for holes). This result shows that monitoring the refraction angle change of the green laser source would be more appropriate. Another set of experiments were conducted with a xenon white light source, and similar results are shown in Figure 3.14. The diffraction of white light by the 2D PhC causes it to split into a rainbow spectrum as different wavelength diffracts at different angles. The position and the order of each color in the rainbow changes as the lattice constant changes. From these two results, it can be deduced that the angle or position of diffracted light of certain wavelength through the 2D PhC is dependent on the lattice constant which is expected to change under the dynamic loading. However, this would require us to develop a collection setup with an angular measurement capability. Furthermore, the direction of applied pressure would be perpendicular to the 2D PhC structure which means the change in the lattice constant is based on the poisson's ratio. From this study, it showed that the angle of the refracted light does not change much under 1% strain (~1.8% for first 10% strain under the green laser soucre). This would lead to very a very low resolution technique as the poisson's ratio is ~0.2 for SiOxNy [67] which means in order to cause the 1% strain in the lattice constant, it would require 5% strain in the z-direction even in static condition. This structure would therefore have a 0.36 degree change in angle of the refracted light, under

1% compression which can be very low angle change to detect. Furthermore, under a dynamic loading (pressure being applied in a very short amount of time), the change in dimension of the plane perpendicular to the loading direction is expected to be minimal and instead the density of the material increases. So the poisson's ratio is expected to be even lowr. Therefore, due to the aforementioned reasons, despite the promision results, we were uncertain whether using 2D PhC structures would be successful to detect pressure (stress)/strain under dynamic loading. Instead, simpler structures were sought and led to a new approach based on 1D PhC which would give a spectral shift under dynamic loading.

3.6 Conclusions

In this chapter, the design and fabrication methods of 2D photonic crystal structure for enhancing the light output of transparent nanocomposite scintillators were optimized. The effect of various lattices, geometries, lattice constant to radius ratios, and refractive indices on the magnitude of the photonic bandgap of the 2D PhC structures were investigated and the optimized design with the maximized photonic bandgap at 543 nm (the emission wavelength of the transparent nancomposite scintillators) was obtained. The fabrication processes for the optimized 2D PhC structure design were developed and fine-tuned on a commericially available glass wafer with a top down approach utilizing electron-beam lithography and inductively coupled plasma reactive ion etching. Subsequently, the optimized fabrication processes were used to successfully fabricate the 2D PhC structure on the transparent nanocomposite scintillator. However, it was later realized that the developed fabrication processes were limited by the current e-beam lithography tool to specimen thickness of ~5 mm. However, the typical transparent

nanocomposite scintillators were required to be at least 10 mm thick to ensure enough cross-sectional area for sufficient x-ray or gamma-ray stopping power. Therefore, it was concluded that an alternative fabrication approach such as nanoimprint lithography which can accommodate a thicker substrate must be explored. During this process, it was also realized that the 2D PhC structure could also be used in an alternative application such as high speed strain/stress (dynamic loading) sensors. Therefore, several 2D PhC structures with different lattice arrangements and geometries were fabricated with varying lattice constants to simulate the effect of the compression. They were illuminated by several laser sources and white light to assess the refractive and diffracted properties. The increase in the angle of reflected light were observed as the lattice parameter increased which indicates a promising potential of the 2D PhC structures as dynamic loading sensors. However, this would require a complicated collection setup with an angular measurement capability as well as the added complication of estimating the lattice constant change based on the PhC materials poisson's ratio. Therefore, despite the promising results, it was concluded that investigations on simpler structures which have spectral properties with dimensional dependance (such as the 1D PhC structures) were required.

4. 1D Photonic Crystal for dynamic loading sensor

Gyuhyon Lee, David A. Scripka, Zhitao Kang, Naresh Thadhani, and Christopher Summers, "***Design and Fabrication of Distributed Bragg Reflector Structures for Dynamic Loading Sensor***", being prepared for submission

4.1 Introduction

Mesoscale heterogeneities in materials or structures often play an important role in the macroscopic behavior of a system under shock loading. Complex loading states driven by mesoscale particle interactions coupled with the limitation of the current diagnostic methods make understanding and predicting the behavior of such a system extremely difficult. Current diagnostic tools have a temporal resolution sufficient to capture the dynamic behavior of a material with nanosecond resolution but with limited spatial resolution. For example, while piezoelectric/piezoresistive stress gauges have fast response, they have a spatial resolution of only several millimeters providing an averaged response of the system [31]. Laser velocimetry systems such as the velocity interferometer system for any reflector (VISAR), provide a point spatial resolution defined by the diameter of the laser beam (~0.5 mm), which is not a complete representation of a system [32]. There are other techniques available such as line-VISAR and the optically recording velocity interferometer system (ORVIS) that can provide sub-mm spatial resolution but only along a one-dimensional line profile [33].

Recently, optical device structures, as opposed to systems, have been investigated to provide enhanced capabilities for dynamic load sensing. For instance,

fiber Bragg Grating sensors were investigated by Ravid et. al, and Sandberg et. al. [68, 69]. They demonstrated their capability for dynamic pressure sensing with the added advantages of low cost, and potential for temperature sensing and spatial resolution. However, disadvantages include low temporal resolution attributed to the device thickness of ~125 μm and limited survivability (fiber fracture which results in lost signal or poor signal quality that complicates analysis).

In a new approach to develop optical dynamical load sensors, we recently proposed modifications to two mature optical devices: the asymmetrical optical micro-cavity (AOMC) and the Distributed Bragg Reflector/Multilayer (DBR/ML) structure [70]. Both devices are typically characterized by an intense, characteristic peak (narrow transmission peak for AOMC, and reflection peak for DBR/ML), formed by additive interference at a specific wavelength whose position depends on the dimensions and refractive indices of the layers comprising the structure. The impact of a compressive shockwave is to shift spectral features to shorter wavelengths where the magnitude of the shift is dependent on the change in optical path length (i.e. a decrease in layer thicknesses and which in some cases can be partially offset by an increase in refractive index), at high pressure. In our previous publication, we demonstrated the potential of AOMC structures as a dynamic loading sensor [71]. This was accomplished by monitoring the shift of a transmission peak under dynamic loading. However, in practice, the device characteristics are monitored in reflectance by measuring the shift in the reflectance minimum (dip) which is the inverse of the transmission peak by using a flash lamp to illuminate the surface of the sample and collection optics to focus the reflected light into a spectrograph coupled to a streak camera. The limitation of the AOMC was realized

from this study; for complex loading scenarios such as applying different pressures across a 2D surface, monitoring the shift and splitting of reflectance dip into many dips, can be extremely complex and difficult compared to that of a shift in a transmission peak. On the other hand, a DBR/ML structure can be an effective alternative as it features a reflectance peak instead of a dip for these complex loading circumstances. However, there can be some disadvantages compared to AOMC. In our previous publication, we showed that the accuracy and sensitivity of the device to shock pressure and changes in shock pressure was, respectively, directly proportional to the position of the characteristic spectral feature and its full-width at half-maxima (FWHM). For optical sensing, the intrinsic speed of response is determined by the length of the active sensor region and refractive index. This is estimated to be higher for the DBR structure due to its longer length; in the order of 600 ps as opposed to 200 ps for the AOMC. Furthermore, because of its multilayer structure, the DBR is expected to show a more complicated behavior than the simple spectral shift observed for the AOMC. Initially, the compression of the first few bilayers (BLs) will signal the emergence of a new peak at shorter wavelengths whose intensity progressively increases as the shock wave propagates through the structure, while in registration, the intensity of the fundamental (original) peak decreases eventually to zero. Thus, after the shock front has passed through the device, only the shifted peak will remain and later will move back to its original position as the device structure relaxes. This is another potential advantage of the DBR/ML structure sensor over the AOMC where it can provide a spatial resolution in the direction of the shock pressure. We note, however, that if the relaxation time is of the same order, or faster than the transient time, a more complex response can be expected. A further and very important

advantage of the DBR/ML device is its potential for measuring the 2D surface (areal) pressure profile across the device. Thus, in this chapter of the thesis, the potential of DBR multilayer structures for dynamic loading sensing was investigated to assess the concept and potential of these devices and as a compliment to the experimental work previously reported on the AOMC sensor. We report, more fully, in this paper the concept of the DBR/ML device; the criteria used for material selection, simulations of device performance to optimize the design, fabrication methods and finally the results obtained from preliminary studies.

4.2 Design criteria and material selection

For dynamic loading sensing, it is extremely important to obtain a highly reliable structure that accurately produces a fast observable response to the impulse of the applied shock pressure wave. Therefore, achieving optimal device characteristics requires careful consideration of the class of materials, their optical and mechanical properties and the ability to grow the structure in a reliable/reproducible way.

Typically, DBRs are designed to behave as dielectric mirrors and comprise many alternating material layers with a high refractive index difference to obtain a wide, strong reflective band (wide FWHM). Consequently, their total thickness is in the millimeter range. However, in contrast, to achieve high spectral discrimination/resolution (positional sensitivity), a DBR multilayer structure must have a narrow FWHM with a high reflectance peak for high signal-to-noise ratio. This makes it preferable to use a material system, in which the refractive index can be compositionally tunable as there is a strong dependence of the peak reflectance and FWHM on the refractive indices and the

difference in refractive indices of the bilayers as discussed later. Also, the total thickness of the structure must be a few micrometers to have a relatively fast temporal resolution (~ a few nanoseconds). Lastly, the DBR multilayer should be composed of layers with similar density and bulk modulus to minimize shock impedance mismatch (acoustic impedance, $Z = c * \rho$, where ρ is the density, c is the speed of sound $\cong \sqrt{\frac{K_s}{\rho}}$, and K_s is the elastic modulus). An impedance mismatch increases the equilibration time and causes high stresses to form at interfaces, making it difficult to estimate the pressure transferred to subsequent layers thereby increasing the complexity of the response and analysis. Thus, well designed DBR multilayer can in principle offer an advantage over the previously investigated AOMC structure which consists of two metal mirror layers and a dielectric cavity layer, which inherently creates a large impedance mismatch as density and modulus greatly differs between metals and oxides (Ag has ~2.2 times higher impedance than *a*-SiO_2: density of Ag = 10.49 g/cm^3, elastic modulus of Ag = 74 GPa, and density of *a*-SiO_2 = 2.20 g/cm^3, elastic modulus of *a*-SiO_2= 72 GPa) [72-76].

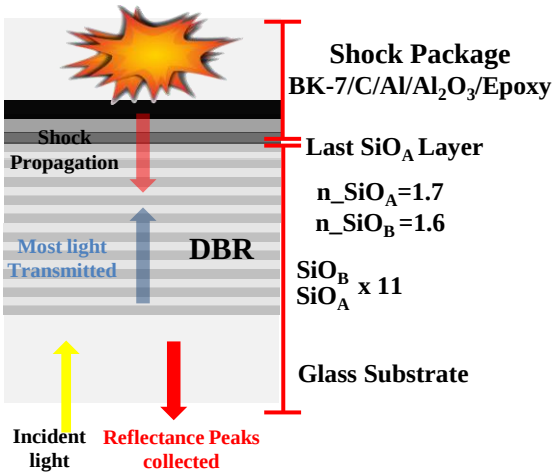

Figure 4.1 Schematic of a SiO_A/SiO_B DBR structure designed for dynamic loading experiments showing the geometrical arrangements for shock wave generation and optical characterization in reflection

A search of materials exhibiting these attributes with low absorption (high transparency) and suitable mechanical properties led to the identification of polymer and metal oxide systems. Of these, different alloys of the SiO_x ($1.0 < x < 2.0$) system were chosen as the material for each layer as their refractive index is small and can be easily tuned between 1.41 and 1.97 at 500 nm by varying the atomic composition of oxygen, *x* [77]. A schematic of the typical DBR structure using SiO_x material system is shown in Figure 4.1. Each layer consisting a bilayer is stoichiometrically altered in oxygen content, so the refractive index is different (SiO_A & SiO_B with A≠B and $n_A \neq n_B$). Mechanical properties of these alloys are very similar for slightly different compositions and subsequently this will minimize the shock impedance mismatch (We expect these values to be between that of SiO and SiO_2: 2.13-2.20 g/cm^3 and 92-72 GPa for x = 1 to 2, maximum of 11% or less impedance difference) [72-76]. Examination of the properties of the SiO_x system in detail showed that for compositions with x less than 1.27, the transmission was poor and that for alloys with x greater than 1.91, the deposition process

became difficult. Thus, the SiO_A and SiO_B ($A \neq B$) compositions forming the multilayer were restricted to $1.27 \leq A < B \leq 1.91$. Within this range the refractive index of SiO_x lies between 1.46 and 1.89 and so allows significant flexibility in device design [77].

With the possible material (and the range of refractive index set) chosen, simulations of the reflectance spectra were performed to find the optimized design using the classical Fresnel equation approach, as available in "OpenFilters" or for the periodic structure by the photonic crystal approach. The Fresnel approach was chosen as it is well proven for both periodic and non-periodic structures and gives greater physical insight [78]. The effect of various parameters such as material properties, thickness, refractive index of each layer, and the number of bilayers were investigated.

For dynamic loading analysis, the fabricated DBR structures were epoxied to a laser shock compression package (BK-7/Carbon/Al/Al_2O_3) in which the shockwave is generated by the carbon/aluminum layers absorbing the energy of an incident 3 J 1064 nm Nd:YAG laser pulse as shown in Figure 4.1. This process produces a rapidly expanding plasma cloud at the carbon/aluminum interfaces that launches a shockwave into the structure. The DBR structure is placed to allow the shock front to directly impact and propagate through the multilayer. Simultaneously, broadband light from a Xenon flash lamp was reflected off the front side through the substrate. The reflected signal was directed into a grating spectrograph and fast streak camera capable of recording a spectrum every 0.25 ns. As the shock pressure propagates through the DBR structure, the thickness and the refractive index of each layer comprising the DBR structure is changed resulting in the shift of the reflectance peak.

4.3 Simulation

4.3.1 Effect of the order of the reflectance peak and number of bilayers

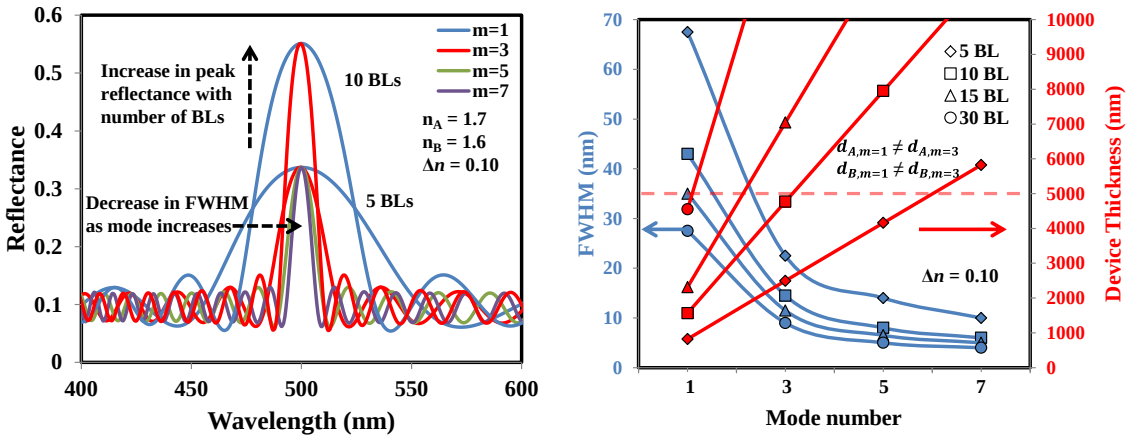

Figure 4.2 (a) Reflectance spectra of DBRs simulated for different optical modes tuned to position the reflectance peak at 500 nm for 5 and 10 bilayers, respectively; (b) Dependence of FWHM (blue) and device thickness (red) required to achieve a reflectance peak at 500 nm for different numbers of bilayers and mode number. For each mode, the thickness of each layer in the bilayer was obtained using Eq. (4.1) assuming the same optical path length for each layer. The total thickness of the device for each mode, m, for a different number of BLs was calculated using Eq. (4.3).

Figure 4.2 shows simulations of the effects of the number of bilayers (BLs), mode number (m), and the total device thickness on the peak reflectance and FWHM. The key spectral characteristics can also be analyzed using the following expressions:

$$m\lambda_m = 2(n_A d_A + n_B d_B),\ m \text{ is an odd integer} \tag{4.1}$$

$$R \approx \left[\frac{{n_B}^{2N} - {n_A}^{2N}}{{n_B}^{2N} + {n_A}^{2N}}\right]^2 \tag{4.2}$$

$$L \approx \mathrm{N}(\mathrm{d}_A + \mathrm{d}_B) + \mathrm{d}_A \tag{4.3}$$

Where m is the mode number, λ_m is the wavelength of the reflectance peak, and n_A, n_B and d_A, d_B refer to the refractive index and thickness of layers A and B in the bilayer, respectively. R and N refer to the peak reflectance and number of BLs, respectively [79]. L is the total length of the device. In Eq. (4.1), the condition $n_A d_A = n_B d_B$ is set to achieve the same optical path length for each layer in the bilayer. The reflectance peak is narrower and higher in intensity with an extra layer of A deposited as was observed by others before [80, 81].

From Eq. (4.1), the wavelength of a peak depends on the thickness and refractive index of each layer in the bilayer. As mentioned previously, the refractive index of layer A and B were restricted between 1.46 to 1.89 based on the high transmission property (low absorption) of visible light and the ease of the fabrication process. To first investigate the effects of number of BLs and the mode number, the refractive index of layer A and B were chosen as 1.7 and 1.6. For our spectrograph/streak camera, the spectral sensitivity is maximized in the range 400 to 600 nm and the DBR structures were designed to operate with a peak reflectance at 500 nm. Thus, to position a reflectance peak at 500 nm for different mode numbers, the required thickness of each layer in the bilayer (d_A and d_B) should change (the thickness increases with mode number). As seen from Figure 4.2(a), the FWHM of a peak decreases with increasing mode number. The effect of the number of BLs is demonstrated from Figure 4.2(a) and Eq. (4.2); the peak reflectance, R, increases and the FWHM decreases with increasing number of BLs. Therefore, although it appears desirable to maximize the number of BLs and the mode number as it minimizes the FWHM (which improves the sensor sensitivity) and maximizes the peak reflectance (which improves the signal to noise ratio). However, this

drastically increases the total device thickness as shown in Figure 4.2(b), causing the transient time of the shockwave through the device to increase, which subsequently exacerbates the temporal resolution of the sensor. Therefore, one needs to select the appropriate device thickness for high optimal sensitivity while maintaining a sufficiently low temporal resolution. The deposition tool used to deposit SiO_x (discussed later), Ion Assisted Deposition (IAD) has a limitation; the total thickness of the SiO_x layers that can be deposited in a single run is limited to approximately 5000 nm. This is shown by the red dotted line in Figure 4.2(b). This restriction leaves us to utilize the 1st order peak with 30 BLs, 3rd order peak with 10 BLs, or the 5th order peak with 5 BLs. As seen from Figure 4.2 (a), the 5th order peak with 5 BLs would not have sufficient peak reflectance (~33%). The 3rd order peak with just 10 BLs has a high enough peak reflectance (~55%) as well as a narrower FWHM (14.5 nm) than the FWHM of the 1st order peak (27.5 nm) of the 30 BLs structure while having a comparable device thickness (4770 nm vs. 4552 nm). While 30 BLs would have a higher peak reflectance (~90%), there would be added fabrication complexity and interfaces present in the structure. Therefore, it was determined that the DBR with 10 BLs utilizing the 3rd order mode peak at 500 nm would be most suitable.

4.3.1 Effect of the refractive indices difference

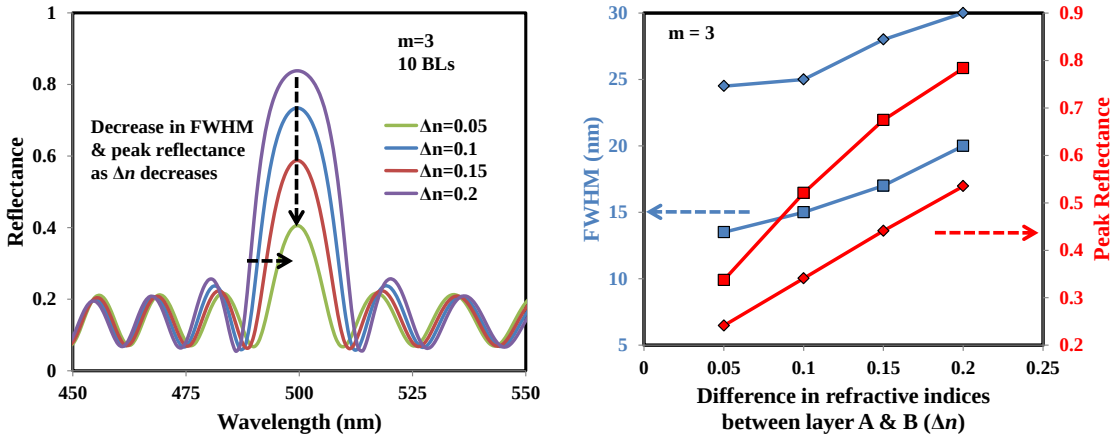

Figure 4.3 (a) Reflectance spectra simulated for a 10 bilayer DBR tuned to position the 3rd order mode reflectance peak at 500 nm for different bilayer refractive indices; (b) Dependence of FWHM (blue) and peak reflectance (red) on the refractive index difference of the bilayers

Figure 4.3 shows the effect of the difference in the refractive indices (Δn) between the layers comprising the bilayers on the reflectance spectra for the 10 BL structure utilizing the 3rd order reflectance peak positioned at 500 nm. The effect of the refractive index difference between the layers on the FWHM of the first order mode is given by the expression:

$$FWHM, \Delta\lambda = \frac{4}{\pi}\lambda \, arcsin\left(\frac{n_B - n_A}{n_B + n_A}\right), \text{ for } m=1 \tag{4.4}$$

It should be noted that the FWHM for different mode numbers follow a similar trend [82].

As observed in Figure 4.3(a), a decrease in Δn improves the sensitivity of the device by decreasing the FWHM. However, it also decreases the peak reflectance, which subsequently lowers the signal to noise ratio thus making the tracking of the peak shift under dynamic loading more difficult. For 10 BLs with a 3rd order reflectance peak at

500 nm, the FWHM is minimized ($\Delta\lambda$ =~14 nm) when Δn = 0.05 but the peak reflectance value is too low (~35%) compared to Δn = 0.10 (~15 nm, ~50%) as shown in Figure 4.3(b). Even though Δn = 0.15 has a higher peak reflectance with moderately low FWHM (~68%, 22 nm), Δn = 0.10 was chosen to minimize the impedance mismatch (as higher Δn increases Δx in SiO_x which increases the density and modulus difference thus creating a larger impedance mismatch). Also, fabrication variations (in terms of thickness and the refractive indices of the deposited layers compared to simulation values) would affect the FWHM (which widens the peak) more than the peak reflectance value. Therefore, from these simulation studies on the effects of various parameters, it was determined that the SiO_A/SiO_B DBR structure with 10 BLs, 3rd order peak at 500 nm (d_A = 220 nm and d_B = 234 nm), and Δn = 0.10 (n_A = 1.7 and n_B = 1.6) has the optimized attributes for use as a dynamic loading sensor.

This design would have an optical response to shock compression of approximately < 3 ns (which is basically limited by the acoustic response of the device); assuming that the transient time of a single shock wave passage is ~0.9 ns (5 um / 5500 m/s) with 3 ring up time for the equilibrium response time. Using a strain to rupture failure value of 0.15 (an over-estimation as it is a static uniaxial compression of a-SiO_2 micropillar array at around 7 GPa and does not consider effects of densification), it is over-estimated that the peak wavelength would show a maximum blueshift of 75 nm for this design [83]. The sensitivity of the device can be estimated using the Rayleigh criteria which is used to differentiate two peaks and in terms of the minimum strain (FWHM) that can be measured from the maximum wavelength shift is ~20% (15 nm/75 nm). The required accuracy in measuring the position of a peak would be around 3% (FWHM/peak

position). However, these would be overestimates and the accuracy and the sensitivity of the device are most likely better as we are monitoring a peak shift and not differentiating between two peaks.

4.4 Device Fabrication and Dynamic Loading Experiments

Following the design phase, DBR structures were fabricated on commercially available 2" diameter fused silica substrates. Immediately prior to growth, the substrates were thoroughly cleaned using solvents and acid (methanol & hydrochloric acid). The alternating layers of SiO_A and SiO_B ($A \neq B$) forming the bilayers were deposited sequentially using Ion-Assisted Deposition (IAD). IAD is capable of controlling various parameters such as precise plasma conditions for added atomic mobility and oxygen flow for atomic composition of the deposited layer. By using IAD we could precisely control and tune the refractive index of each deposited layer. The effect of the oxygen flow on the refractive index of the deposited SiO_x layer was determined. The stoichiometric oxygen content in SiO_x was varied by using a different O_2 flow rate from 0 to 30 sccm at room temperatures for growth rates of 0.2 nm/s. The range of x for the deposited SiO_x layer was approximated to be in between 1.30 to 1.91 using EDX and the refractive index of the deposited layer was between 1.51 and 1.75. The deposited layer exhibited high transmission (low absorption) to visible light [77]. It should be noted that the total thickness of the SiO_x layers deposited in a single run was limited to a maximum thickness of approximately 5 μm. To obtain a thicker DBR structure, the IAD chamber was vented to replenish the raw material. The thicknesses of the deposited layers were characterized

using a profilometer. The reflectance spectra and refractive indices were measured using a Filmetrics thin film interferometer system.

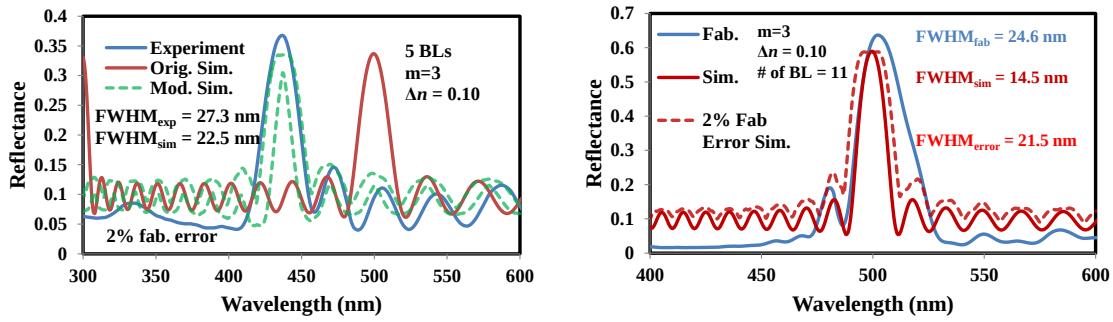

Figure 4.4 Reflectance spectra of the fabricated DBR structure, the original design, and 2% thickness variations from the fabrication errors incorporated in the simulation with (a) 5 BLs and (b) 11BLs.

The thickness and the refractive index of the deposited layers were calibrated and the optimal IAD deposition conditions were obtained by growing SiO_x using different IAD conditions on multiple test coupons. The DBR structure was fabricated using 10 and 20 sccm oxygen flow rates to deposit layer A and B, respectively in the effort to match the optimized design determined from the simulations. The thickness of the deposited layer A and B were closely matched to the target thickness (d_A = 220 nm and d_B = 234 nm but the subsequent layers were more susceptible to variations from the target thickness (as expected because the quartz crystal microbalance which measures the deposition rate is less precise as it ages). The oxygen composition of the deposited layers A and B was estimated to be 1.51 and 1.8 respectively and the corresponding refractive index was approximated to be 1.65 and 1.55. Figure 4.4(a) shows the reflectance spectrum of the fabricated DBR structure with 5 BLs. As it can be observed from the Figure 4.4, the fabricated DBR structure has the peak reflectance at around 440 nm

instead of the originally designed 500 nm. This is because the IAD deposition calibration was not optimized at this stage and thicknesses of the deposited layers in the superlattice were not as thick as their respective target thicknesses. The reflectance spectrum of the DBR structure simulated with the correct thickness shows that the FWHM is within the 2% fabrication error range (thickness variation). The thickness and the refractive index of a deposited layer were calibrated better and the optimal IAD deposition conditions were obtained to successfully deposit 11 BLs DBR structure shown in Figure 4.4(b). It should be noted that 11 BLs were successfully deposited in a single IAD run and the simulated spectra were adjusted accordingly to fit the experimental data. The obtained reflectance spectra show that the FWHM of the peak is wider than simulated, even after incorporation of a ±2% thickness variation. However, the relative peak reflectance value remained high (~61.7%) and comparable to the original simulation (58.9%). This confirms that the design decision of utilizing Δn = 0.10 was correct as the Δn = 0.15 design would have resulted in a higher FWHM, lowering the sensitivity of the device as a sensor.

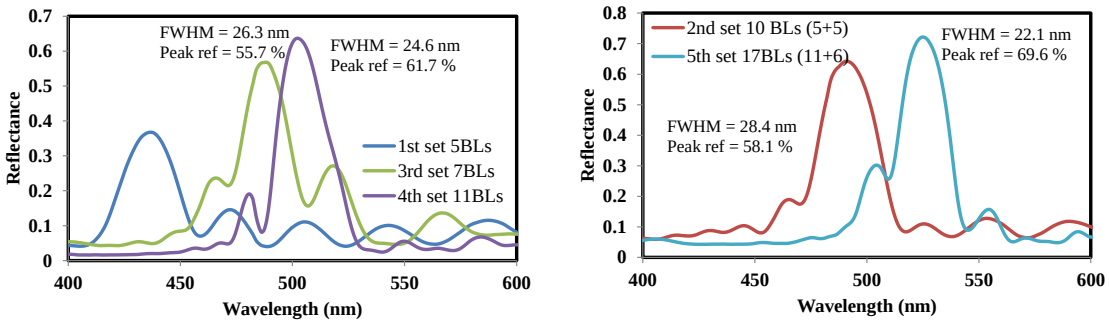

Figure 4.5 Reflectance spectra of the fabricated DBR structures with (a) a single step IAD run and (b) multiple steps IAD run.

Table 4.1 List of fabricated structures and their optical properties

Sample #	Number of bilayers	FWHM (nm)	Peak Reflectance	Peak Position (nm)
1	5	27.34	32.72%	436.6
2	10 (5+5)	28.37	58.11%	491.07
3	7	23.44	52.35%	488.6
4	11	24.62	61.69%	502.16
5	17 (11+6)	22.1	69.59%	525.52
6	11	30.095	51.27%	516.93
7	21 (11+10)	30.095	53.16%	516.93

Figure 4.5 shows the reflectance spectra of the other fabricated DBR multilayer structures and the Table 4.1 shows the optical properties of the fabricated structures. For the single step IAD run samples (Figure 4.5(a)), as the number of the deposited BLs increases, peak reflectance increases. However, the FWHM does not become linearly as expected. This is most likely because the thickness control of the deposited layers gets more difficult as the number of the deposited layers increases and this affects the FWHM more than the peak reflectance value. This trend also seems to apply for the multiple steps IAD run samples (Fig 4.5(b)). It seems very difficult to identify the effects of using multiple IAD runs as opposed to a single IAD run. When comparing 2nd set of sample with 10 BLs deposited through two IAD runs, versus the 4th set of 11 BLs deposited in one run, a single IAD run sample seems to be better in terms of optical properties. This seems to be different when comparing the 5th set to the 4th set but it is no consistent when comparing it to 7th set of the sample. Therefore, more controlled investigations for the deposition condition should be done in the future.

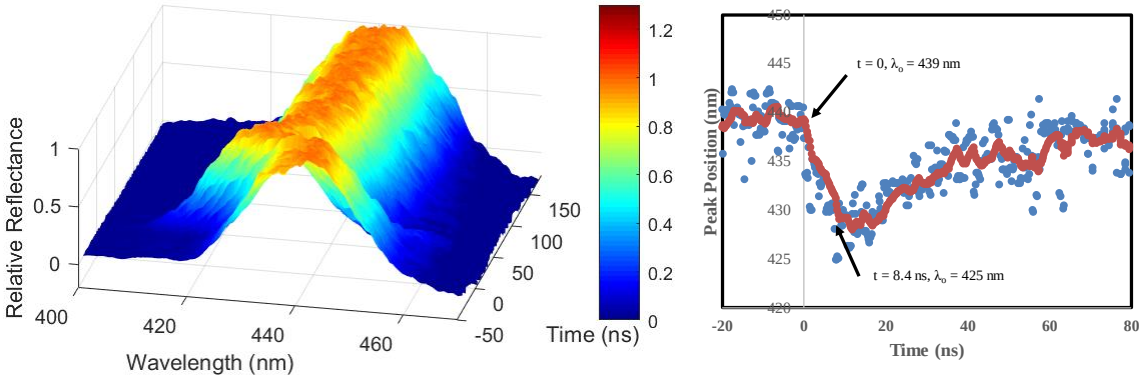

Figure 4.6 Reflectance spectrum of a fabricated DBR structure taken by the streak camera for different times successfully capturing the shift in reflectance peak caused by applied shock pressure of ~4.0 GPa

Figure 4.6 shows the preliminary dynamic loading experiment result conducted on 5 BL sample; reflectance spectra of a SiO_A/SiO_B DBR structure (utilizing 3rd mode peak at 500 nm with $d_A \approx$ 198 nm, $d_B \approx$211 nm, $n_A \approx$ 1.65 and $n_B \approx$ 1.55) under approximately 4.0 ± 1 GPa at different time stamps. It should be noted that the 5 BL SiOx DBR structure have thinner layer thickness than the design specification which accounts for shifted (blue) peak location than the design. This result clearly shows the promising feasibility of the specially designed DBR structure as a dynamic loading sensor. At t = 0 (a moment before the shock pressure impact), the reflectance spectrum shows a peak reflectance at around 439 nm. As t increases, the characteristic peak starts to blue-shift until t = 8.4 ns where it almost reaches its full shifted peak position of 425 nm. Between t= 0 ns to 8.4 ns, we were expecting to see introduction of a secondary peak peak while the original peak still having some intensity; as some of the layers subjected to the shock pressure would show the shifted peak while the rest uncompressed would have the peak at the original location. However, this phenomenon was not observed. This is most likely due the structure only having 5 BLs instead of the original design of 10

BLs. 5 BLs would be enough number of BLs to show a characteristic reflectance peak but when only half of the structure is compressed, it would be 2~3 BLs that would be responsible for shifted/original peaks. We believe it may still be possible to observe this phenomenon with higher number of BL structure which would demonstrate the full capability of this device; the spatial resolution on the direction of the shock pressure. At until around t = 17.4 ns, the location of the peak still remains at ~428 nm. After t > 17.4 ns, the peak starts to red-shift and it reaches around 438 nm at 100 ns. For about 120 ns, the peak hovers around at 438 nm and it finally relaxes back to its original peak position at around t = ~220 ns. Unlike the SiO_2 AOMC structure where the full peak shift was observed after 3.3 ns which matches the approximate rise-time for the shock pressure in the setup, the peak shift was observed more slowly for the DBR structure. Also, the peak shift observed by the DBR structure was less than the AOMC structure under the similar shock load of 4 GPa (~14 nm vs. 22 nm). Furthermore, it was at the compressed state for a longer time (~9 ns vs almost instantaneous for the AOMC structure) and also it took more time for the structure to relax back to its original uncompressed state (100 ns vs. 24.2 ns) dimension the full shift was recorded long after the shock pressure profile reaches its maximum pressure (~3.3 ns) and is much slower device. This is mostly attributed to the thicker total device thickness (~2.6 um vs. 600 nm) as well as more complicated device structure. Thus, the DBR structure would take a longer time to reach the equilibrium state which is what we observed even through relaxation. This preliminary result clearly indicates that an optimally designed DBR structure can successfully detect the shock impact with a relatively high temporal resolution of 8.4 ns. It also suggests that in order to see whether it can provide a spatial resolution in the

direction of applied pressure, thicker device with more BLs must be characterized. However, a DBR sensor with more accurate spatial resolution on that direction would only be possible with a sacrifice in temporal resolution.

4.5 Conclusion

From the in-depth simulation efforts, it was determined that the finding the optimized DBR design is critical in order to maximize the shock sensor performance within the local constraint. Although utilizing high order of reflectance peak, many number of bilayers, and a relatively low refractive indices difference in superlattice layers would result in a very high and narrow reflectance peak width, this would tremendously increase the total thickness of the device which would subsequently decrease the temporal resolution of the device as well as the fabrication difficulty. Working within the total thickness restriction currently set by the fabrication tool, it was determined that the optimized design would have 10 bilayers of SiO_A and SiO_B layers with respective thickness of 220 nm and 234 nm and refractive index of 1.7 and 1.6 at 500 nm. This DBR structure was fabricated and was further improved by depositing 11 bilayers. The fabricated DBR structure was placed under a dynamic loading of ~4 GPa and the reflectance peak shift of ~14 nm was detected in 8.4 ns. The peak widening (or separation) observed during the dynamic loading experiment also suggests that the DBR structure can have spatial resolution in the direction of the applied shock pressure. These results successfully demonstrated the promising potential of the DBR structure as a shock sensor. Also, this DBR structure can further provide us an insight on how the SiO_x materials with different composition behave under an extreme condition such as shock pressure.

5. Asymmetrical Optical Microcavity for dynamic loading sensor

Gyuhyon Lee, David A. Scripka, Zhitao Kang, Naresh Thadhani, and Christopher Summers, "***Asymmetrical optical microcavity structures for dynamic pressure sensing: design, fabrication, validation***", *Opt. Express* 24, 23494-23504 (2016)

5.1 Introduction

The dynamic loading behavior of composites and particulate materials is highly complex as their macroscopic behavior is driven by mesoscale interactions. Despite their prevalence and importance, a comprehensive understanding of such materials is deficient due to a lack of diagnostic tools with desired spatial and temporal resolution. Thus, sensor designs that are capable of providing material state information with high spatial and temporal resolutions are critical to advance the understanding of dynamic behavior in complex, heterogeneous material systems.

Currently, there are few diagnostic tools that simultaneously have sufficient temporal and spatial resolution to capture the highly transient dynamic events controlling mesoscale interactions. For instance, while piezoelectric/piezoresistive stress gauges can provide accurate stress-time profiles with nanosecond temporal resolution [31] their spatial resolution is on the order of millimeters, thus providing only an averaged response of the system. Similarly, laser velocity interferometers, such as the velocity interferometer system for any reflector (VISAR) [32], Fabry-Perot [84, 85] and heterodyne systems [86], all provide accurate velocity profiles with nanosecond resolution, but only for a single spatial point presenting a certain volume. A more capable

system; the optically recording velocity interferometer system (ORVIS), has demonstrated sub-nanosecond temporal resolution and sub-mm spatial resolution but only along a one dimensional line profile [33].

In contrast to the limitations of these existing methods, optical microcavities (OMCs), can potentially provide two-dimensional surface data, with comparable temporal resolution. OMCs are composed of an optical medium (cavity layer) placed between two reflecting mirror layers whose principal optical characteristic, the resonant frequency, depends predominantly on the thickness and the refractive index of the cavity layer. The resonant frequency, or cavity mode, corresponds to the particular wavelength of light that can be transmitted. Furthermore, cavity modes of OMCs are typically very sharp with narrow full-width-half-maximum (FWHM) and high transmission. Under dynamic compression, the thickness of the cavity layer along with its refractive index change due to the applied pressure, cause a spectral shift in the transmission peaks or complementary reflectivity minima. By monitoring the shift of a particular cavity mode using time-resolved spectroscopy, it is possible to capture two-dimensional data corresponding to the area of the OMC structure under dynamic loading. These promising characteristics were recently published in an in-depth theoretical study assessing the potential of OMC structures for use in dynamic compression sensing by Scripka *et al.* [70]. In this work, modeling of an OMC structure with a TiO_2 cavity layer surrounded by Distributed Bragg Reflectors (DBR) composed of alternating TiO_2/SiO_2 layers was performed which showed a shift of the characteristic cavity mode under uniaxial shock compression with a rapid temporal response. Therefore, further design and experimental

studies were initiated, with an emphasis on optimizing the design and fabrication processes for dynamic load sensing [87].

In this part of the thesis, asymmetrical OMC (AOMC) designs and fabrication processes for dynamic loading diagnostics were investigated. The effect of different materials and structural designs on sensor performance were simulated and optimized, and the feasibility of required fabrication processes validated. AOMCs instead of OMCs were chosen to maximize the amount of reflected light from the sample by depositing a thicker mirror layer as the final surface of the multilayer and to provide some additional mechanical stability under shock compression conditions. The optimized designs of the AOMC structures have attributes suited for use as dynamic loading sensors. A fabricated AOMC structure was then subjected to laser-driven shock compression, and the time-resolved position of the characteristic spectral peak was recorded using a streak camera coupled spectrograph**.**

5.2 Design Methodology

Figure 5.1 shows the device design developed during the course of this investigation. The AOMC structure is epoxied to the shock-compression package which has several layers: BK-7/Carbon/Al/Al_2O_3. The AOMC structure was configured to permit optical interrogation from one side (the substrate side) such that the shock front from the opposite side directly impacts the active cavity layer. The shock is generated by the carbon/aluminum layers in the package absorbing the energy of the incident laser pulse, which produces a rapidly expanding plasma cloud, or “explosion” at the interface of the carbon/aluminum layers and shock package substrate. This drives a shock wave

into the AOMC, as shown in Figure 5.1 (a). Simultaneously, broadband light from a Xenon flash lamp is reflected off the AOMC substrate, and is collected and directed into a grating spectrograph. The spectrograph separates the component wavelengths, and additional optics focus the output from the spectrograph onto the input slit of a fast streak camera, which records the temporal evolution of the spectra with a resolution down to 0.5 ns.

The reflectance and transmission spectra of various AOMC structures were simulated using the OpenFilters software which includes the dispersion properties of the optical materials used in this investigation [78]. Device parameters such as layer thicknesses, reflectivity, and material refractive index, were used as input parameters to simulate the effect of each parameter on the optical properties of the AOMC. In fabricating sensor devices, it is extremely important to achieve highly reliable structures that reflect the true value of their component materials. Thus, in addition to device design, the selection of materials and deposition systems are critical and must take into consideration the resulting optical and structural properties. For example, OMCs are typically fabricated using Distributed Bragg Reflectors (DBR), but the thickness (~2 μm) of these structures can result in their response to strain or shock obscuring the cavity effect and lead to a very complex analysis. Thus, thin Ag reflectors were chosen whose optical (reflective) properties are less affected by stress and which directly and rapidly transfer the stress to the cavity material. Although some of the energy of the shock wave is dissipated in the mirrors due to the impedance mismatch between Ag and SiO_2, in comparison to the thicker (2 μm) multilayer DBR design, the energy loss is very small. This is due both to the thinness of the Ag layer and the moderate difference in impedance

that results in very little shock energy loss at the interfaces. Therefore, for this application, these simplified designs significantly reduce device complexity and consequently enhance reliability without any loss in performance. This structure also addresses an additional design requirement; namely, that the shock be transferred instantaneously to the sensor layer so as to enhance the temporal response of the device. Using the appropriate material parameters (elastic modulus, density, etc) for a 125 nm thick Ag mirror and a 500 nm thick SiO_2 cavity layer the device response to shock compression was estimated to be <200 ps. To our knowledge, the number of optical materials for which reliable shock parameters are known is very small (SiO_2, TiO_2, Al_2O_3 and LiF). Thus, for this proof-of-principle study we selected SiO_2 and Al_2O_3 as the best cavity materials as their deposition and fabrication techniques have also been well studied.

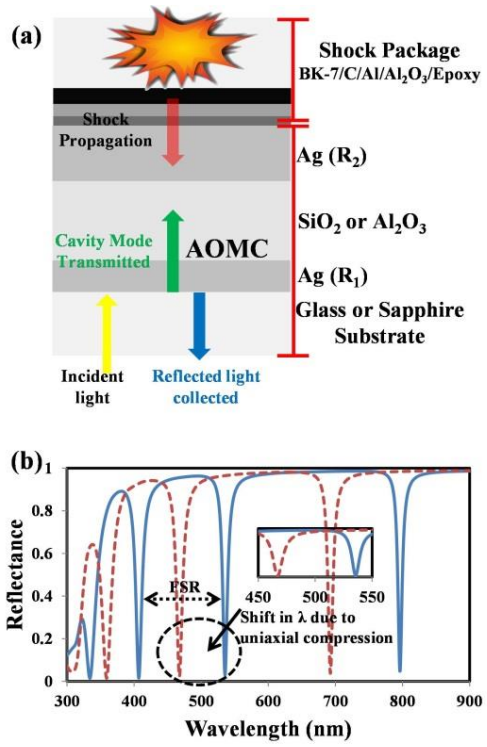

Figure 5.1 Schematic of a SiO_2 (or Al_2O_3) AOMC structure under dynamic loading experiment and the reflectance spectrum simulated for a Ag/SiO_2/Ag AOMC with a 500 nm thick SiO_2 cavity layer (continuous blue line), and after being compressed to the fracture limit (dotted red line). The inset depicts the calculated shift in the reflectance minimum due to the maximum static compression at the strain to failure point.

Figure 5.1 (a) shows a schematic of the simplified SiO_2 (n=1.46 at 535 nm) and Al_2O_3 (n=1.77 at 535 nm) AOMC stress-sensors consisting of just three layers: two Ag mirror layers and a cavity layer. The reflectance spectrum was simulated for a 500 nm thick SiO_2 cavity layer and a 35 nm thick semi-transparent (11% transmittance at 535 nm) front Ag mirror layer and ~98% back reflecting 125 nm thick Ag layer. The top Ag layer is designed to be thicker for two reasons: (a) to provide a buffer layer for shock pressure, (b) enable high reflectivity for better optical signal. Although the thickness, refractive index, and reflectivity of each layer all affect the reflectance spectrum, the positions of the reflectance minima are mostly affected by a change in the cavity layer thickness. The

dotted red curve shows the simulated effect of a dimensional change in the SiO_2 cavity layer under static compression. It has been previously reported [83] that a-SiO_2 micropillar array exhibits a strain to rupture failure value of 0.15 in uniaxial compression at around 7 GPa. By employing this number in simulation, a blueshift of the reflectance minimum by ~70 nm is obtained. It should be noted that the blueshift obtained is an over-estimation as it is under static compression, and also it does not consider other effects such as densification which can result in modification of refractive index. For an Al_2O_3 AOMC structure with the same design parameters, a smaller spectral shift is predicted due to its superior hardness and inherent lower strain at failure compared to SiO_2 [88]. Thus, a SiO_2 based design is expected to be significantly more sensitive to pressure.

The accuracy to which a particular minimum can be measured directly determines the sensitivity of the device to changes in length and/or refractive index. This will depend on how narrow the particular FWHM minimum is and requires a standardized procedure for measuring and comparing data. For the latter we employed a Rayleigh-like criterion to distinguish two adjacent peaks, such that when the first minimum of a peak lies under the maximum of an adjacent peak then the dip between them is 20% less than the maximum intensity of either. For a Gaussian or Lorentzian line shape this is approximately equivalent to the FWHM of the peak. Thus, for example for SiO2 cavity designs with FWHMs of 9 and 1.5 nm, as discussed later, the percentage accuracy in measuring the position of a peak is determined by the ratio FWHM/(peak position); ~1.64% and ~0.27% respectively, for a peak position of 550 nm centered at the maximum response of the measuring system. To calculate the sensitivity in terms of the minimum strain that can be measured for a given material, we can obtain an estimate

from the wavelength shift expected at the strain to fracture limit. For SiO_2, this is 70 nm and gives 13% (9/70 x 100) and 2.1% (1.5/70x100), respectively for the two designs. In principal by judicious curve fitting, and since we are not differentiating two peaks but a shift of a peak, it is estimated that the accuracy can be improved, potentially by a factor of five. Therefore, the designed device must have a sharp transmission peak (which from now on is referred to as a reflectance minimum as we collect reflectance spectrum) and positioned to match the maximum spectral sensitivity of the spectrograph and streak camera: in this case between 400-700 nm. Additionally, for maximum device sensitivity, the FWHM must be narrow compared to the free spectral range (FSR) between reflectance minima (shown in Figure 5.1) and the bandwidth of the measuring instrumentation. Additionally, a strong overall reflectance is required to enhance the capture and collection of light during the short duration of dynamic loading. We have therefore, rigorously investigated the impact of both material and structural parameters and fabrication issues on the optimization of AOMC structures designed for dynamical loading applications.

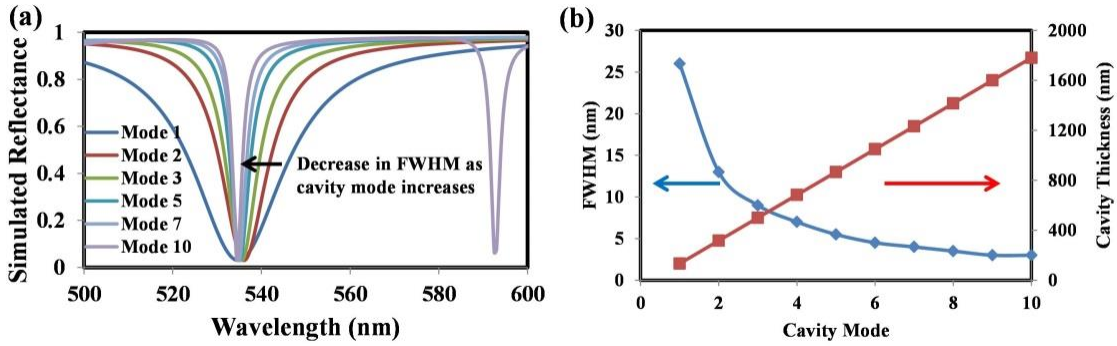

Figure 5.2 (a) Shape of reflectance spectra simulated for different modes of AOMCs tuned for reflectance minimum at 535 nm (b) dependence of FWHM and cavity thickness (as required to achieve a reflectance minimum at 535 nm) on cavity mode number

Figure 5.2 shows the dependence of the spectral reflectance, as calculated using the OpenFilters software, on the structural dimensions of the AOMC. Additionally, the AOMC can be analyzed in terms of the theory for Fabry-Perot structures where the reflectance minima (cavity modes) can be obtained from the expression:

$$2nlcos(\theta) = m\lambda \tag{5.1}$$

where m (a positive integer) refers to the mode number, n is the refractive index, l is the length (thickness) of the cavity layer, and θ is the angle of incident light.

Figure 5.2(a) shows a collection of reflectance spectra for AOMC structures designed to position the reflectance minimum at λ = 535 nm for each mode number. As the mode number increases, the cavity layer thickness must also increase in order to keep the reflectance minimum positioned at λ = 535 nm. Figure 5.2(b) shows the dependence of FWHM (δλ) and the required cavity layer thickness, l, on the cavity mode number, m. The FWHM, δλ, at λ = 535 compliance increases from ~100 to 1200 nm. This can be explained from the expression:

$$\delta\lambda = \frac{\Delta\lambda}{F} \tag{5.2}$$

$$F = \frac{\pi(R_1R_2)^{1/4}}{(1-(R_1R_2)^{1/2})} \tag{5.3}$$

$$\Delta\lambda = \frac{{\lambda_o}^2}{2n_g lcos(\theta)} \tag{5.4}$$

Where δλ refers to the FWHM, F refers to the finesse, Δλ refers to the FSR. Eq. (3) is for an asymmetrical cavity (where R1 and R2 are the reflectivity's of the front and back

mirrors, respectively) and in (4), λ_o is the central wavelength of the nearest adjacent reflectance minimum (shown at 593 nm for m=10 in Fig. 2), and n_g (~n) is the group refractive index **[89]**.

As l increases, λ_o decreases because according to Eq. (5.1), there are more reflectance minima in a given spectral range which means that adjacent minimum become closer to the minimum of interest, λ = 535 nm. Therefore, the increase in *l* results in a decrease in λ_o and $\Delta\lambda$, which ultimately decreases $\delta\lambda$, as desired. However, even though a higher cavity mode is beneficial, it should be noted that the required cavity layer thickness increases linearly. Thus, it is essential to find the optimum cavity layer thickness for each material while also considering the impact of the fabrication process on the deposited film quality. From these considerations and the data shown in Figure 5.2 for a SiO_2 AOMC structure, it was determined that the 3rd order reflection minimum was sufficiently narrow (FWHM ~ 9 nm) while also keeping the thickness of the cavity layer thin.

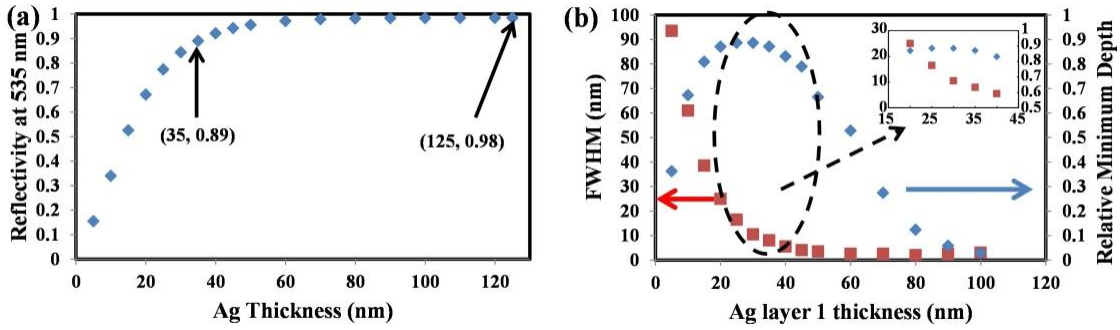

Figure 5.3 (a) Dependence of reflectivity of Ag mirror at 535 nm on Ag thickness (b) dependence of characteristic minimum (m=3) FWHM and depth on Ag mirror layer 1 thickness for a fixed SiO_2 cavity thickness of 500 nm and Ag mirror layer 2 thickness of 125 nm; inset image shows zoomed in graph of a region of interest

Figure 5.3 shows the OpenFilters computations performed to establish the mirror properties that gave the best reflectance minimum depth and narrowest FWHM [13]. Figure 5.3(a) shows that the mirror reflectivity at 535 nm increases exponentially as the thickness increases. The reflectivity is close to 1 at 60 nm. From the simulation, it was found that AOMC with Ag mirror layers had the best spectral characteristics (in terms of the depth of minima and FWHM) compared to other metal such as Al and Au mostly due to its excellent reflectivity in visible light range. Furthermore, it was determined from the simulation that the thickness of mirror layer 2 has minimal effect on the reflectance spectrum and the characteristic features above 60 nm. Therefore, we decided to make it ~ 125 nm as it also acts as the shock buffer layer. Figure 5.3(b) shows the effect of the thickness of Ag mirror layer 1 on the characteristic minimum's (m=3) FWHM (red markers) and depth (blue markers) of AOMC with a fixed SiO_2 cavity thickness (500 nm) and mirror layer 2 (125 nm). As the thickness of mirror layer 1 increases, the FWHM of the characteristic cavity mode decreases drastically. On the other hand, the depth of the characteristic minimum increases initially, but then starts to decrease past a certain thickness. The inset image in Figure 5.3(b) shows the zoomed graph of the region of interest. The relative minimum depth is maximized at 25 nm, but the FWHM is too wide (~16.5 nm). Thus, even though there is a drop in the depth of minimum at 35 nm, it is still relatively high at 87% and the FWHM is acceptably narrow at 9 nm. Therefore, the thickness of the mirror layer 1 was optimized to be at 35 nm.

Using the same procedures for the Al_2O_3 AOMC, it was determined that the AOMC consists a 990 nm Al_2O_3 cavity layer and front and back Ag mirror layers 105 nm and 53 nm thick, respectively, with a 7th order transmission peak FWHM of 1.5 nm. The

Al_2O_3 AOMC length was chosen to utilize a higher order reflecting feature since the deposition process for Al_2O_3 is more uniform and stable than SiO_2. We note that an even higher order mode could have been utilized for the Al_2O_3 AOMC structure but as shown in Figure 5.2, the decrease in FWHM after the 7th order was minimal.

5.3 AOMC Fabrication Procedure

For this investigation, the AOMC structures were fabricated on commercially available 1" square aluminoborosilicate glass substrates or 2" diameter sapphire substrates sectioned into quarters. Substrates were thoroughly cleaned using organic solvents and acid (methanol & hydrochloric acid). Ag mirror layers were deposited by electron-beam evaporation which was chosen over sputtering to provide higher surface and interface smoothness. The cavity layers were deposited using ion-assisted deposition (IAD); selected for its capability for high spatial uniformity, simultaneous deposition of different dielectric layers, and particularly its accurate control over the deposition rate and application of plasma excitation for enhancing atomic mobility so as to achieve high density film depositions and sharp interfaces at low temperatures (20 ℃). Note that achieving a high density cavity layer is very important as the density directly affects the refractive index and the dynamic loading behavior of the structure. Therefore, the use of IAD which provides precise control over the deposition rate is very important and is a less invasive deposition technique compared to techniques such as sputtering.

The thicknesses of the deposited layers were characterized using test coupons and a profilometer and the reflectance spectra and refractive indices were measured using a Filmetrics thin film interferometer system. After successful validation of the static

spectral behavior, the fabricated AOMC structures were epoxied to a laser shock compression package for the dynamic loading experiment. Details of the dynamic loading experiment have been reported [8].

5.4 Results and Discussion

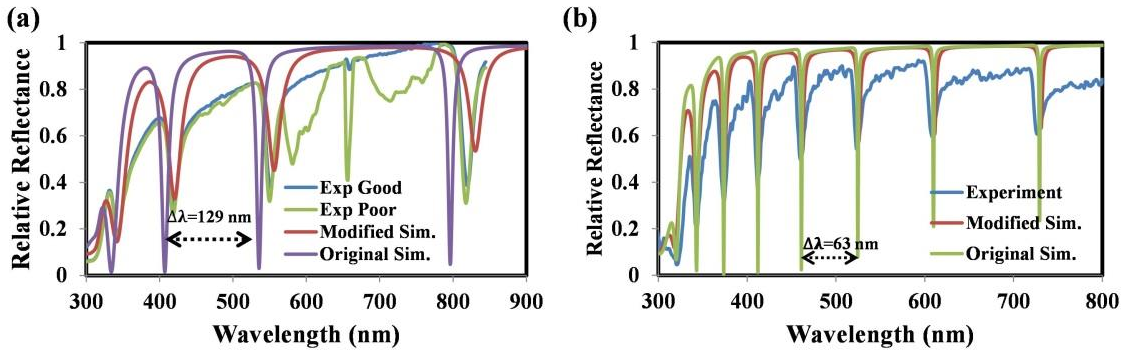

Figure 5.4 Reflectance spectra of the simulated design, fabricated structures and the fitted simulation based on experimental results of (a) SiO_2 and (b) Al_2O_3 AOMC structures

Table 5.5.1. Comparison between simulated and experimental spectral characteristics

Device	Ag-SiO_2 AOMC (m = 3)		Ag-Al_2O_3 AOMC (m = 7)	
	Experiment	Simulation	Experiment	Simulation
Cavity Mode Wavelength (nm)	551.3	535.9	478.7	524.5
FWHM (nm)	20	9	17	1.5
Relative Minimum Depth (%)	45	97	35	91

Figure 5.4 shows the reflectance spectra of the simulated designs, along with the experimental data from the fabricated structures and refitted simulations based on these results. The parameters obtained from the original simulations and those measured for the fabricated structures are compared in Table 5.1. As shown on Fig. 5.4(a), the spectrum measured for the SiO_2 AOMC structure is shifted by 15 nm to shorter wavelengths compared to the targeted design, while no such shift is observed for the Al_2O_3 AOMC. For both structures, the fabricated devices have wider FWHMs and shallower minima

than those predicted from simulations. The shifts in the reflectance spectrum and cavity modes for SiO_2 OMC structures are attributed to differences in the thickness and/or refractive index of the cavity layer as shown from the Eq. (5.1). Thus, the refractive indices and thicknesses of the deposited cavity layers were independently measured. The re-computed predictions employing these corrections reveal that the simulated peak locations are in excellent agreement with experiment. However, a disparity still exists in the depth of the reflectance minimum and FWHM between the experiment and simulations and this is attributed to the mirror layers. As discussed previously in Figure 5.3, the depth of the minimum and FWHM in an asymmetrical OMC structure can be greatly influenced by the reflectivity of mirror layer 1. A decrease in the reflectivity of mirror 1 lowers the finesse, F, according to Eq. (5.3). This also increases the FWHM following the Eq. (5.2). The FWHM can also be affected by the small difference in refractive index of the cavity layer as it affects FSR according to Eq. (5.4). The fitted simulation results for both SiO_2 and Al_2O_3 AOMC structures reflecting the corrections of both the refractive index/thickness of the cavity layer and the reflectivity of the mirror layers reveal reflectance spectra in excellent agreement with the fabricated structures. However, it should be noted that some of the SiO_2 AOMC structures were unstable and exhibited different reflectance spectra (in green), as shown in Figure 5.4(a). The SiO_2 AOMC structures were found to degrade even more over time and with light/atmosphere exposures due to the poor adhesion between SiO_2 and Ag [14]. Under dynamic loading, the signal-to-noise ratios were very low and spectral responses relied heavily on significant data processing/filtering to distinguish and monitor spectral shifts. This was due to insufficient depths in the characteristic minima exhibited for both fabricated SiO_2

and Al_2O_3 AOMC structures which can hinder their utility as dynamic loading sensors. Therefore, different designs with increased sample stability, minima depth, and narrower FWHM were developed and further investigated.

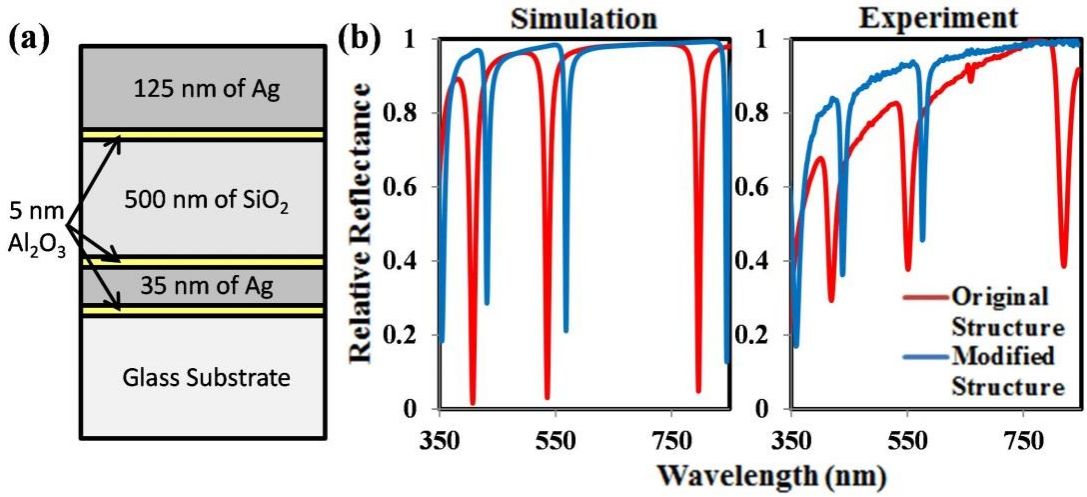

Figure 5.5 (a) Schematic of SiO_2 AOMC structure fabricated using Al_2O_3 adhesion layers and (b) comparison of simulated and measured reflectance spectra of modified and the original SiO_2 AOMC structure

Table 5.5.2. Comparison of parameter values between simulated and measured spectra for both the original and modified SiO_2 AOMC structures

Ag-SiO_2 AOMC (m=3)	Simulated Spectra		Experimental Spectra	
	Original Design	Modified Design	Original Design	Modified Design
Cavity Mode Wavelength (nm)	535.5	568	551.3	576
FWHM (nm)	9	5	20	8.5
Relative Minimum Depth (%)	97	80	45	48

Figure 5.5(a) shows a schematic of a modified SiO_2 AOMC structure designed to address the instability in the original SiO_2 AOMC structure due to poor adhesion between SiO_2 and Ag. As shown, a thin layer of Al_2O_3 was deposited at each SiO_2/Ag interface to enhance adhesion. Figure 5.5(b) compares the simulated and measured reflectance spectra of both the modified and the original SiO_2 AOMC structures and Table 5.2 lists

comparisons of their key parameters. When comparing the experimental results, the modified design shows improvements in both the relative minimum depth and FWHM (9 versus 5 nm theoretical and 20 versus 8.5 nm measured) of the characteristic minimum. This is because the poor adhesion and high interfacial energy between Ag and SiO_2 not only affects sample stability but also its spectral properties. High interfacial energy leads to uneven thickness, high interface roughness, defects, and porosity of the deposited Ag layer which decreases its reflectivity as the evaporated Ag atoms minimize their interfacial energy by preferentially growing on previously deposited areas, leading to non-uniform thickness. Therefore, the incorporation of thin Al_2O_3 layers improved the stability and the reflectivity of the mirror layers and the increase in reflectivity of the mirror layers enhanced the spectral properties by narrowing the FWHM and increasing reflectance minimum depth for the modified SiO_2 AOMC structure.

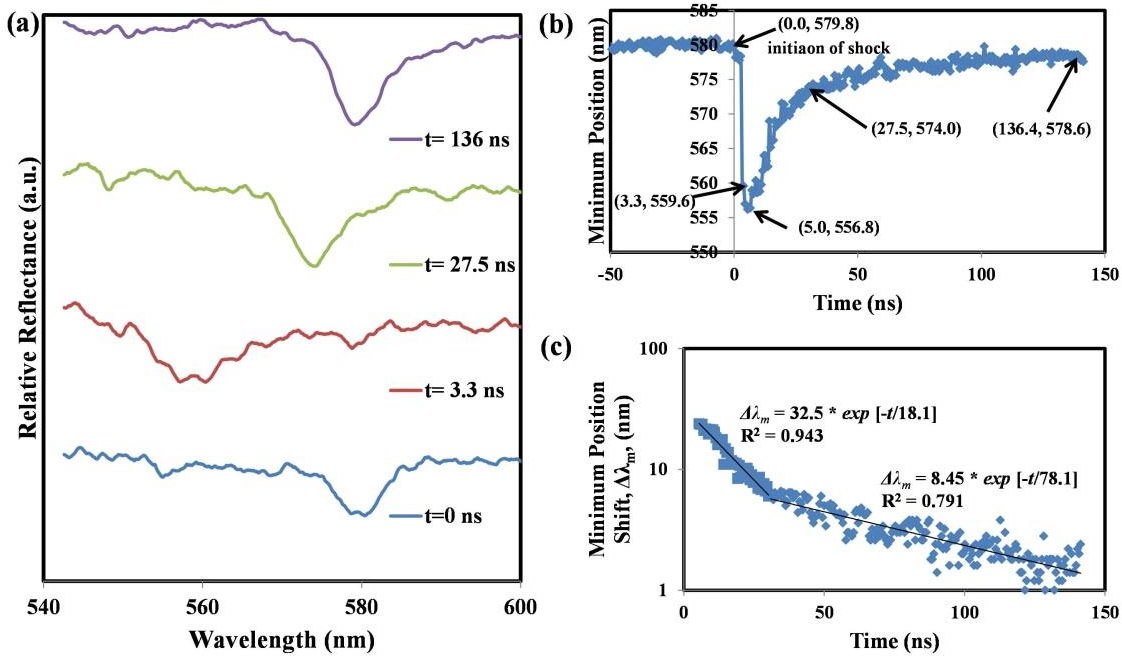

Figure 5.6 (a) Spectral and temporal response of a modified SiO_2 AOMC device to a

4 GPa shock front. The spectra were recorded using a streak camera at different times to capture the shift in the reflectance minimum (mode 3) caused by the applied shock pressure. (b) The reflectance minimum over time and (c) change in the reflectance minimum position over time after shock propagation.

Figure 5.6 shows the spectral response of the modified design under application of ~4 GPa shock pressure, which was chosen to be significantly below the estimated Hugonist Elastic Limit (HEL) for fused SiO_2 [15]. This preliminary result clearly shows the high promise and feasibility of properly designed SiO_2 AOMC structures as very sensitive, fast response, dynamic loading sensors. At t=0 (immediately before shock impact), the reflectance minimum is centered at 580 nm. The shock impact was almost instantaneously observed as a blueshift in the reflectance minimum of 22 nm within 3.3 ns of the shock wave impact, which is the approximate rise-time for the pressure pulse in the present laser-driven shock experimental setup. After 27.5 ns the reflectance minimum has decreased to 574 nm indicating that the structure quickly relaxes. For longer times, the magnitude of the blueshift decreases at a slower rate, and after 136 ns, displays a small redshift of ~0.8 nm, which is within the experimental error, and can possibly be due to a ringing effect. Figure 5.6(c) indeed clearly shows a two-step recovery exhibiting fast and slow release regimes with the relaxation times of 18.1 ns and 78.1 ns, respectively. This two-step behavior can mostly be attributed to the shape of the pressure pulse that laser-driven shock produces: a sharp rise followed by a slow, drawn out release back to low pressure. Also, some of the behavior can be due to the layers surrounding the cavity layer as they also release down from a higher pressure and will have their own behavior applying stress on the cavity layer. Lastly, there could be other contributing factors from the non-linear elastic decompression behavior of the SiO_2 to chemical bond length and bond angle restoration and crystallization [16], but it is very difficult to determine these

phenomena and their effects accurately. Regardless, the monitoring cavity mode's wavelength shifts observed and the data recorded after 3.3 ns, which is very close to the estimated response time of the structure, demonstrate that AOMC devices can be designed and fabricated with very fast response times for use as diagnostics for measurements of nanosecond resolution dynamic effects.

5.5 Conclusion

In this study asymmetrical metallic OMC structures (AOMC) were shown to significantly enhance device utility for dynamic strain measurements with high temporal resolution (and the potential for high spatial resolution): limited only by the designed linewidth of the resonant mode. The study supports result of previous simulations [7] and initial experimental data that the thickness (and refractive index) of the cavity layer plays a major factor in determining the spectral position, mode number and FWHM of the reflectivity minima. As such, the reflectivity of the mirror layers is also shown to be critical to optimizing device design and required fabrication processes that ensured high stability, as well as ease of processability. The experimental results show that further improvements can be made in this area. It is concluded that for $Ag/SiO_2/Ag$ AOMC structures, thin Al_2O_3 adhesion layers are best suited for this application and lead to the successful detection of a dynamic compression with a blueshift of 22 nm after 3.3 ns. At present, cavity materials with low refractive index and high modulus are shown to be most suitable, however, the lack of values of shock parameters of materials subjected to shock loading, and recent observations that device geometry is very important in determining these limits, illustrates the further potential to not only extend the sensitivity

of these devices but also their use as a platform for monitoring the extreme limits of shock compression.

6. Conclusions and Future Work

6.1 Conclusions

In this thesis, we have investigated how the fundamental relationships between the glass matrices, choice of materials, and thermal processing conditions affect the light output of the transparent nanocomposite scintillators. We investigated on further improving the light output of the scintillators by employing 2D surface photonic crystal structures. We also investigated the multilayer optical structures (distributed Bragg reflector and optical microcavity) and the interplay between the optical and acoustic properties to develop dynamic loading sensors capable of providing stress/pressure profile with nanosecond temporal and 2D spatial resolutions.

We have successfully synthesized the transparent nanocomposites scintillators by a melt-quench method followed by annealing to precipitate GdF_3:Tb and $BaGdF_5$:Tb nanocrystals in an aluminosilicate glass matrix. We have observed efficient energy transfers between Gd^{3+} and Tb^{3+} ions in both GdF_3 and $BaGdF_5$ based scintillators and increase in luminescence intensities with increasing Tb doping concentrations. It was found that $BaGdF_5$ based scintillators are more efficient than the GdF_3 based scintillators due to the higher density, increased nanocrystal volume compared to glass matrix, and the quantum cutting effect. We also found that when GdF_3 was added to the $BaGdF_5$ nanocrystal based scintillator raw materials before the melt-quenching procedure, it can increase the nucleation rate. With the addition of GdF_3, the scintillators required a lower annealing temperature (700 ℃ -> 600 ℃) to precipitate $BaGdF_5$ nanocrystals and a higher nanocrystal to matrix volume fraction could be achieved (33.4% -> 37.4%) with more uniform homogeneous distribution of nanoparticles. Gamma-ray results indicated

that the performance of the $BaGdF_5$ nanoparticle based scintillators was further improved (by 2.4 times) with GdF_3 added as a nucleating agent.

We have also successfully developed 2D photonic crystal structures for enhancing the light outcoupling of the scintillators to PMTs. We have optimized the design of the 2D PhC structure with the maximized bangap width of 28 nm centered at 543 nm through simulations. The fabrication process utilizing e-beam lithography and inductively coupled plasma reactive ion etching were successfully developed. However, it was later realized that the developed fabrication processes were limited by the current tools and that an alternative fabrication approach must be explored. During this process, it was also realized that the 2D PhC structure could be used in an alternative application such as high speed strain/stress (dynamic loading) sensors. Several 2D PhC structures with different lattice arrangements and geometries were fabricated with varying lattice constants to simulate the effect of the compression. The increase in the angle of reflected light were observed as the lattice parameter increased which indicates a promising potential of the 2D PhC structures as dynamic loading sensors under various light sources. However, this would require a complicated collection setup with an angular measurement capability. Thus, sensor geometries that exploit a spectral shift capability were investigated.

We have also determined the optimized DBR design maximizing the shock sensor performance within the local constraint. Following the design and working within the restrictions currently set by the fabrication tools, we have successfully fabricated 5 and 11 bilayers DBR structures with SiO_A and SiO_B with respective thickness of 220 nm and 234 nm and refractive index of 1.7 and 1.6 at 500 nm. The fabricated DBR structure was placed under a dynamic loading of ~4 GPa and the reflectance peak shift of ~14 nm was

detected in 8.4 ns. The peak widening (or separation) observed during the dynamic loading experiment also suggests that the DBR structure can have spatial resolution in the direction of the applied shock pressure. These results successfully demonstrated the promising potential of the DBR structure as a shock sensor. Also, this DBR structure can further provide us an insight on how the SiO_x materials with different composition behave under an extreme condition such as shock pressure.

Asymmetrical metallic OMC structures (AOMC) were successfully designed and fabricated to be used as a dynamic loading sensor with the advantage of high temporal resolution with various cavity materials (Al_2O_3, SiO_2 and PMMA). The AOMC with a SiO_2 cavity layer showed the most promising optical properties as a sensor and the design was modified following the initial device fabrication to improve the stability and the optical properties directly related to the sensor's performance by incorporating thin adhesion layers of Al_2O_3. The successfully developed and optimized design with thin Ag mirrors and SiO_2 cavity along with the adhesion layers were subjected to dynamic loading of approximately 4 GPa which led to blueshift of 22 nm with temporal resolution of 3.3 ns. This promising results showed the advantage of the AOMC structure compare to the DBR ML structure; fast temporal response due to thinner device thickness as well as the potential for providing the 2D spatial resolution.

In summary, we have gained valuable fundamental insights on the effects of various structural, chemical and materials factors and their correlation on the performance of the transparent nanocomposite scintillators as well as the dynamic loading sensors. This information can help us further improve these devices and may assist in commercialization of a significantly cheaper alternative scintillator and a sensor

or a diagnostic tools offering 2D spatial resolutions with fast, nano-second temporal resolution.

6.2 Future Works

While significant improvement of scintillation performance was demonstrated, the light output under x-ray and gamma-ray excitation needs to be further enhanced in order to aggressively replace the current scintillators. In addition, even though the dynamic sensing has been demonstrated, the sensor performances need to be improved and the sensor's capability in 2D spatial resolution must be demonstrated.

For the transparent nanocomposite scintillators, several routes can be taken to improve the scintillation performance. The current system can be further improved with more comprehensive studies. For example, judicious manipulation of $BaGdF_5$ and Tb concentrations as well as the thermal treatment conditions should be performed. Furthermore, the incorporation of CsF can be more carefully and fully analyzed; to improve the refractive index matching between the glass matrix and the nanocrystals. This can further improve the ceiling of the nanocrystals concentrations and the volume fraction of nanocrystal to glass matrix without causing light scattering. The second approach is utilizing a different kind of nanocrystal. There are alternative cubic nanocrystals that can be possible formed in the glass matrix such as $LiGdSiO_4$, $LnBGeO_5$ and $GdBGeO_5$. As the effect of the nanocrystal on the light output is significant, they must be properly investigated. Lastly, as the potential benefit of the 2D photonic crystal had been demonstrated, an alternative fabrication technique such as nanoimprint

lithography which can fabricate the pattern at low cost must be investigated to enhance the light out-coupling of the scintillators to PMTs.

Both the AOMC and the DBR ML structures had demonstrated their capabilities as the dynamic loading sensors with excellent temporal resolutions. However, their signal to noise along with other spectral features can be further improved. For the AOMC structure, it was demonstrated that the reflectivity of the Ag mirror layer had significant effects on both the peak transmission and the FWHM. Therefore, investigation on depositing Ag layers at an elevated temperature to ensure smoother and a higher reflective surface are expected to be beneficial. Also, we have learned that the thickness of the device does not exacerbate the temporal resolution as significantly as expected. Thus, we can also try incorporating a thicker SiO_2 cavity layer utilizing a higher mode number (5 or 6) which would significantly improve the signal to noise ratio while reducing the FWHM. For the DBR ML structures, we should further improve the current device (SiO_x) and also investigate devices utilizing other materials. Further improving the current device growth and processing conditions should be performed to reduce thickness variation errors. Also, we need to experimentally determine the optimum device thickness and the number of bilayers. These approaches will improve the signal to noise ratio while reducing the FWHM. Another material that can be investigated is silicon oxynitride (SiO_xN_y). Similar to SiO_x, SiO_xN_y materials have compositionally tunable refractive index, and the materials properties (such as density and the modulus) are expected to be similar between compositional variants. Additionally, unlike SiO_x, SiO_xN_y is highly transparent in all the visible light range. Therefore, the DBR ML structure utilizing SiO_xN_y can have improved signal to noise ratio by reducing the wasted light due

to absorption. When both structures have improved their spectral properties, they should be subjected to different dynamic pressures at different locations to investigate their spatial resolution capabilities.

REFERENCES

1. Leo, W.R., *Techniques for Nuclear and Particle Physics Experiments: A How-to Approach*. 2012: Springer Berlin Heidelberg.
2. Joannopoulos, J.D., et al., *Photonic Crystals: Molding the Flow of Light (Second Edition)*. 2011: Princeton University Press.
3. Yablonovitch, E., *Inhibited Spontaneous Emission in Solid-State Physics and Electronics.* Physical Review Letters, 1987. **58**(20): p. 2059-2062.
4. John, S., *Strong localization of photons in certain disordered dielectric superlattices.* Physical Review Letters, 1987. **58**(23): p. 2486-2489.
5. Fudouzi, H. and T. Sawada, *Photonic Rubber Sheets with Tunable Color by Elastic Deformation.* Langmuir, 2006. **22**(3): p. 1365-1368.
6. Viel, B., T. Ruhl, and G.P. Hellmann, *Reversible Deformation of Opal Elastomers.* Chemistry of Materials, 2007. **19**(23): p. 5673-5679.
7. Ozin, G.A. and A.C. Arsenault, *P-Ink and Elast-Ink from lab to market.* Materials Today, 2008. **11**(7–8): p. 44-51.
8. Arsenault, A.C., et al., *From colour fingerprinting to the control of photoluminescence in elastic photonic crystals.* Nat Mater, 2006. **5**(3): p. 179-184.
9. Chan, E.P., et al., *Block Copolymer Photonic Gel for Mechanochromic Sensing.* Advanced Materials, 2011. **23**(40): p. 4702-4706.
10. Hu, Y.-W., et al., *Optomechanical sensing with on-chip microcavities.* Frontiers of Physics, 2013. **8**(5): p. 475-490.
11. Sünner, T., et al., *Photonic crystal cavity based gas sensor.* Applied Physics Letters, 2008. **92**(26): p. 261112.
12. Herrmann, R., et al., *Ultrahigh-quality photonic crystal cavity in GaAs.* Optics Letters, 2006. **31**(9): p. 1229-1231.
13. Robinson, J.T., L. Chen, and M. Lipson, *On-chip gas detection in silicon optical microcavities.* Optics Express, 2008. **16**(6): p. 4296-4301.
14. Ballato, J. and A. James, *A Ceramic Photonic Crystal Temperature Sensor.* Journal of the American Ceramic Society, 1999. **82**(8): p. 2273-2275.
15. Wang, R., et al., *A Reflective Photonic Crystal Fiber Temperature Sensor Probe Based on Infiltration with Liquid Mixtures.* Sensors, 2013. **13**(6): p. 7916.
16. Rahman, A., *Temperature sensor based on dielectric optical microresonator.* Optical Fiber Technology, 2011. **17**(6): p. 536-540.
17. Oder, T.N., et al., *III-nitride blue and ultraviolet photonic crystal light emitting diodes.* Applied Physics Letters, 2004. **84**(4): p. 466-468.
18. Vahala, K., *Optical Microcavities*. 2004: World Scientific.
19. Vahala, K.J., *Optical microcavities.* Nature, 2003. **424**(6950): p. 839-846.
20. McKigney, E.A., et al., *Nanocomposite scintillators for radiation detection and nuclear spectroscopy.* Nuclear Instruments and Methods in Physics Research Section A: Accelerators, Spectrometers, Detectors and Associated Equipment, 2007. **579**(1): p. 15-18.
21. Chen, G., et al., *Fluorozirconate-based nanophase glass ceramics for high-resolution medical X-ray imaging.* Journal of Non-Crystalline Solids, 2006. **352**(6–7): p. 610-614.
22. Williams, G.V.M., et al., *Glass-ceramics and epoxy-composites for radiation imaging.* Radiation Measurements, 2007. **42**(4–5): p. 899-902.
23. Koch, A., et al., *X-ray imaging with submicrometer resolution employing transparent luminescent screens.* Journal of the Optical Society of America A, 1998. **15**(7): p. 1940-1951.
24. Leo, W.R., *Techniques for Nuclear and Particle Physics Experiments a How-to Approach*. 1994, Springer Berlin Heidelberg: Berlin, Heidelberg :.
25. Cherepy, N.J., et al. *High energy resolution with transparent ceramic garnet scintillators*. 2014.
26. Cherepy, N.J., et al. *Transparent ceramic scintillators for gamma spectroscopy and radiography*. 2010.

27. Barua, A., et al., *Prediction of probabilistic ignition behavior of polymer-bonded explosives from microstructural stochasticity.* Journal of Applied Physics, 2013. **113**(18): p. 184907.
28. Dwivedi, S.K., L. Pei, and R. Teeter, *Two-dimensional mesoscale simulations of shock response of dry sand.* Journal of Applied Physics, 2015. **117**(8): p. 085902.
29. Dwivedi, S.K., et al., *Two dimensional mesoscale simulations of projectile instability during penetration in dry sand.* Journal of Applied Physics, 2008. **104**(8): p. 083502.
30. Xu, A.-G., et al., *Dynamics and Thermodynamics of Porous HMX-like Material Under Shock.* Communications in Theoretical Physics, 2009. **52**(5): p. 901.
31. Graham, R.A., F.W. Neilson, and W.B. Benedick, *Piezoelectric Current from Shock-Loaded Quartz—A Submicrosecond Stress Gauge.* Journal of Applied Physics, 1965. **36**(5): p. 1775-1783.
32. Barker, L.M. and R.E. Hollenbach, *Laser interferometer for measuring high velocities of any reflecting surface.* Journal of Applied Physics, 1972. **43**(11): p. 4669-4675.
33. Bloomquist, D. and S. Sheffield, *Optically recording interferometer for velocity measurements with subnanosecond resolution.* Journal of Applied Physics, 1983. **54**(4): p. 1717-1722.
34. Milbrath, B.D., et al., *Radiation detector materials: An overview.* Journal of Materials Research, 2008. **23**(10): p. 2561-2581.
35. Létant, S.E. and T.F. Wang, *Semiconductor Quantum Dot Scintillation under γ-Ray Irradiation.* Nano Letters, 2006. **6**(12): p. 2877-2880.
36. Campbell, I.H. and B.K. Crone, *Quantum-Dot/Organic Semiconductor Composites for Radiation Detection.* Advanced Materials, 2006. **18**(1): p. 77-79.
37. Blasse, G. and B.C. Grabmaier, *Luminescent Materials*. 1994, Springer Berlin Heidelberg: Berlin, Heidelberg :.
38. Zhang, W., et al., *Luminescent properties of Eu2+-doped BaGdF5 glass ceramics a potential blue phosphor for ultra-violet light-emitting diode.* Journal of Applied Physics, 2015. **117**(2): p. 023113.
39. Doris, E., *Photoluminescence in glasses and glass ceramics.* IOP Conference Series: Materials Science and Engineering, 2009. **2**(1): p. 012001.
40. Clara Gonçalves, M., L.F. Santos, and R.M. Almeida, *Rare-earth-doped transparent glass ceramics.* Comptes Rendus Chimie, 2002. **5**(12): p. 845-854.
41. Beall, G.H. and L.R. Pinckney, *Nanophase Glass-Ceramics.* Journal of the American Ceramic Society, 1999. **82**(1): p. 5-16.
42. Beall, G.H. and D.A. Duke, *Transparent glass-ceramics.* Journal of Materials Science, 1969. **4**(4): p. 340-352.
43. Berthier, T., V.M. Fokin, and E.D. Zanotto, *New large grain, highly crystalline, transparent glass–ceramics.* Journal of Non-Crystalline Solids, 2008. **354**(15–16): p. 1721-1730.
44. Shan, Z., et al., *Luminescence in rare earth-doped transparent glass ceramics containing GdF3 nanocrystals for lighting applications.* Journal of Materials Science, 2010. **45**(10): p. 2775-2779.
45. Karmakar, P., et al., *Crystallization kinetics analysis of BaF2 and BaGdF5 nanocrystals precipitated from oxyfluoride glass systems: A comparative study.* Thermochimica Acta, 2015. **610**(0): p. 1-9.
46. Huang, S., Q. Gao, and M. Gu, *Enhanced luminescence in transparent glass ceramics containing BaYF5: Ce3+ nanocrystals.* Journal of Luminescence, 2012. **132**(3): p. 750-754.
47. Gu, M., et al., *Luminescence properties of Pr3+-doped transparent oxyfluoride glass–ceramics containing BaYF5 nanocrystals.* Journal of Luminescence, 2012. **132**(10): p. 2531-2536.
48. Biswas, K., A.D. Sontakke, and K. Annapurna, *Synthesis and Structural Probing of Eu3+ Doped BaYF5 Nano-Crystals in Transparent Oxyfluoride Glass-Ceramics.* International Journal of Applied Glass Science, 2012. **3**(2): p. 154-162.
49. Liu, X., et al., *Elaboration, Structure, and Luminescence of Eu3+-Doped BaLuF5-Based Transparent Glass-Ceramics.* Journal of the American Ceramic Society, 2013. **96**(3): p. 798-800.
50. Li, H.H., *Refractive index of alkaline earth halides and its wavelength and temperature derivatives.* Journal of Physical and Chemical Reference Data, 1980. **9**(1): p. 161-290.
51. Stenzel, O., *Optical Coatings: Material Aspects in Theory and Practice*. 2014: Springer.
52. Tzeng, H.-Y., B.-M. Cheng, and T.-M. Chen, *Visible quantum cutting in green–emitting BaGdF5:Tb3+ phosphors via downconversion.* Journal of Luminescence, 2007. **122–123**(0): p. 917-920.

53. Huang, S. and M. Gu, *Enhanced luminescent properties of Tb3+ ions in transparent glass ceramics containing BaGdF5 nanocrystals.* Journal of Non-Crystalline Solids, 2012 **358**(1): p. 77-80.
54. Cao, C., et al., *RE3+ (RE = Ce3+, Tb3+) doped BaGdF5 nanocrystals: Synthesis, optical and magnetic properties, and energy transfer.* Materials Research Bulletin, 2012. **47**(7): p. 1704-1708.
55. Lee, G., et al., *Synthesis and luminescence properties of transparent nanocrystalline GdF3:Tb glass-ceramic scintillator.* Journal of Luminescence, 2014. **147**(0): p. 363-366.
56. Porter-Chapman, Y.D., et al., *Scintillation and Luminescence Properties of Undoped and Cerium-Doped LiGdCl4 and NaGdCl4.* IEEE Transactions on Nuclear Science, 2009. **56**(3): p. 881-886.
57. Cho, H.K., et al., *Light extraction enhancement from nano-imprintedphotonic crystal GaN-based blue light-emitting diodes.* Optics Express, 2006. **14**(19): p. 8654-8660.
58. Li, K.H., et al., *III-nitride light-emitting diode with embedded photonic crystals.* Applied Physics Letters, 2013. **102**(18): p. 181117.
59. Shen, X.X., et al., *Optimization design of holographic photonic crystal for improved light extraction efficiency of GaN LED.* Superlattices and Microstructures, 2013. **64**: p. 303-310.
60. Xu, W. and Y. Li, *The Effect of Anisotropy on Light Extraction of Organic Light-Emitting Diodes with Photonic Crystal Structure.* Journal of Nanomaterials, 2013. **2013**: p. 6.
61. Kronberger, M., E. Auffray, and P.R. Lecoq, *Improving Light Extraction From Heavy Inorganic Scintillators by Photonic Crystals.* Nuclear Science, IEEE Transactions on, 2010. **57**(5): p. 2475-2482.
62. Knapitsch, A., et al. *Effects of photonic crystals on the light output of heavy inorganic scintillators*. in *Nuclear Science Symposium and Medical Imaging Conference (NSS/MIC), 2011 IEEE*. 2011.
63. Knapitsch, A., et al., *Results of Photonic Crystal Enhanced Light Extraction on Heavy Inorganic Scintillators.* Nuclear Science, IEEE Transactions on, 2012. **59**(5): p. 2334-2339.
64. Zhu, Z., et al., *Enhanced light extraction efficiency for glass scintillator coupled with two-dimensional photonic crystal structure.* Optical Materials, 2013. **35**(12): p. 2343-2346.
65. Pandey, R.K., et al., *Growth and characterization of SiON thin films by using thermal-CVD machine.* Optical Materials, 2004. **25**(1): p. 1-7.
66. Godinho, V., et al., *SiOxNy thin films with variable refraction index: Microstructural, chemical and mechanical properties.* Applied Surface Science, 2010. **256**(14): p. 4548-4553.
67. Boch, P. and J. Glandus, *Elastic properties of silicon oxynitride*. Journal of Materials Science, 1979. **14**(2): p. 379-385.
68. Ravid, A., et al., *Fibre Bragg Grating sensor for shock wave diagnostics.* Journal of Physics: Conference Series, 2014. **500**(14): p. 142029.
69. Sandberg, R.L., et al., *Embedded optical probes for simultaneous pressure and temperature measurement of materials in extreme conditions.* Journal of Physics: Conference Series, 2014. **500**(14): p. 142031.
70. Scripka, D., et al., *Spectral response of multilayer optical structures to dynamic mechanical loading.* Applied Physics Letters, 2015. **106**(20): p. 201906.
71. Lee, G., et al., *Asymmetrical optical microcavity structures for dynamic pressure sensing: design, fabrication, validation.* Optics Express, 2016. **24**(20): p. 23494-23504.
72. Ross, R.B., *Metallic Materials Specification Handbook*. 2013: Springer US.
73. Committee, A.I.H., *Properties and Selection: Nonferrous Alloys and Special- Purpose Materials*. 1990: ASM International.
74. Nayar, A., *The Metals Databook*. 1997: McGraw-Hill.
75. Lide, D.R., *CRC Handbook of Chemistry and Physics, 85th Edition*. 2004: Taylor & Francis.
76. Bauccio, M., *ASM engineered materials reference book*. 1994: ASM International.
77. Durrani, S.M.A., M.F. Al-Kuhaili, and E.E. Khawaja, *Characterization of thin films of a-SiO x (1.1< x <2.0) prepared by reactive evaporation of SiO.* Journal of Physics: Condensed Matter, 2003. **15**(47): p. 8123.
78. Larouche, S. and L. Martinu, *OpenFilters: open-source software for the design, optimization, and synthesis of optical filters.* Applied Optics, 2008. **47**(13): p. C219-C230.
79. Sheppard, C.J.R., *Approximate calculation of the reflection coefficient from a stratified medium.* Pure and Applied Optics: Journal of the European Optical Society Part A, 1995. **4**(5): p. 665.

80. Kolle, M., et al., *Stretch-tuneable dielectric mirrors and optical microcavities.* Optics Express, 2010. **18**(5): p. 4356-4364.
81. Álvarez, A.L., et al., *Polymeric multilayers for integration into photonic devices.* Thin Solid Films, 2003. **433**(1–2): p. 277-280.
82. Brovelli, L.R. and U. Keller, *Simple analytical expressions for the reflectivity and the penetration depth of a Bragg mirror between arbitrary media.* Optics Communications, 1995. **116**(4): p. 343-350.
83. Lacroix, R., et al., *Micropillar Testing of Amorphous Silica.* International Journal of Applied Glass Science, 2012. **3**(1): p. 36-43.
84. Goosman, D., *Measuring velocities by laser Doppler interferometry.* LLNL Energy and Technology Review, UCRL-52000-79-3, Lawrence Livermore National Laboratory, Livermore, CA, 1979: p. 17-24.
85. McMillan, C., et al., *Velocimetry of fast surfaces using Fabry–Perot interferometry.* Review of Scientific Instruments, 1988. **59**(1): p. 1-21.
86. Strand, O., et al., *Compact system for high-speed velocimetry using heterodyne techniques.* Review of Scientific Instruments, 2006. **77**(8): p. 083108.
87. Scripka, D., et al. *Spectral Response of Multilayer Optical Structures to Dynamic Loading*. in *APS Shock Compression of Condensed Matter Meeting Abstracts*. 2015.
88. Callister, W.D., *Fundamentals of Materials Science and Engineering: An Integrated Approach WileyPlus*. 2008: John Wiley & Sons, Incorporated.
89. Lipson, A., S.G. Lipson, and H. Lipson, *Optical Physics*. 2010: Cambridge University Press.

VITA

Gyu Hyon (Eric) Lee

Gyu Hyon was born in Gwang Myung, Korea. He immigrated to Canada when he was thirteen. He received his B.S. in Nanotechnology Engineering from University of Waterloo in 2012. He pursued a doctoral degree in Materials Science and Engineering at Georgia Institute of Technology in 2012.